ELASTIC STIFFENING IN PVA-BORAX STUDIED WITH EXPERIMENTAL MEDIUM AMPLITUDE OSCILLATORY SHEAR

BY

OLIVIA CAREY-DE LA TORRE

THESIS

Submitted in partial fulfillment of the requirements
for the degree of Master of Science in Mechanical Engineering
in the Graduate College of the
University of Illinois at Urbana-Champaign, 2017

Urbana, Illinois

Adviser:

Associate Professor Randy Ewoldt

Abstract

In this thesis, we seek to understand the mechanisms of strain-stiffening and shear-thickening often observed in transient or associative polymer hydrogels; specifically, Poly(vinyl) alcohol (PVA) crosslinked with Sodium tetraborate (Borax), or PVA-Borax. We use medium amplitude oscillatory shear (MAOS) as a tool to measure asymptotically nonlinear viscoelastic material functions across a range of compositions of PVA-Borax with storage moduli ranging from $G_0 \approx 100 - 3000$ Pa. The material functions can be related to model parameters to gain physical insight into the structure of the material system. We demonstrate that with a "good" structure-rheology model [1], a single nonlinear parameter scales the asymptotically nonlinear material functions, and we argue that finite-extensibility is the sub-dominant cause of nonlinearity ($< 5\%$) compared to stretch-induced crosslinking. Furthermore, we validate the model by using first-harmonic MAOS measures to predict third-harmonic MAOS via a single nonlinear model parameter. Finally, we define a universal nonlinear parameter to compare the strength of nonlinearities across a range of strain-stiffening materials.

Acknowledgements

I would like to thank my mother and brother for their unwavering support throughout my educational career. I would also like to thank my advisor Dr. Randy Ewoldt for the excellent guidance and for being an understanding and supportive mentor. Many thanks to Ashwin Bharadwaj for helping me get started on this project and for teaching me experimental techniques and the theory behind this work. A big thank you to Rebecca Corman and Arif Nelson for recruiting me to this awesome group, Piyush Singh and Luca Martinetti for helping me better understand experimental procedures and theory crucial to this work, and the rest of the Ewoldt group for all of their help and support. Finally, thanks also goes to Eric Epstein for the insightful materials science discussions.

Contents

Chapter 1

Introduction and Background

Nonlinearities are inherent to any system. There exists some limit in which a linear response will deviate from it's "normal" response when subject to sufficiently large external stimuli. There has been recent interest in introducing elastic nonlinearities to improve the performance of dynamical systems, such as vibration energy harvesters [2]–[6]. For an elastic mechanical system, a nonlinear response is represented as a deviation from a linear Hookean response (e.g. keeping the first term in a Taylor series expansion) and is modeled as a nonlinear restoring force,

$$\begin{aligned} F(x) &= k(x)x \\ &= k_1 x \left(1 + k_3 x^2\right), \end{aligned} \tag{1.1}$$

where the spring stiffness, $k(x) = k_1 \left(1 + k_3 x^2\right)$, is described by the linear spring constant k_1 and is dependent on the displacement, x. The amplitude of the leading order nonlinearity is represented by k_3. Here, if $k_3 < 0$ the system will exhibit a softening response, while $k_3 > 0$ represents a stiffening response. Ramlan et al. have shown that elastic stiffening improves the performance of an energy harvester by broadening the frequency response of the output power [3].

Just as nonlinearities can be advantageous for a dynamical system, it has been shown that biological materials often exhibit a nonlinear stress-strain response to preserve their physiological functionality [7]. For a material system with a three-dimensional structure, the characteristic spring stiffness, k, in Eqn. 1.1 is represented as an intrinsic elastic modulus, e.g. the shear modulus G. Thus, a nonlinear shear stress response

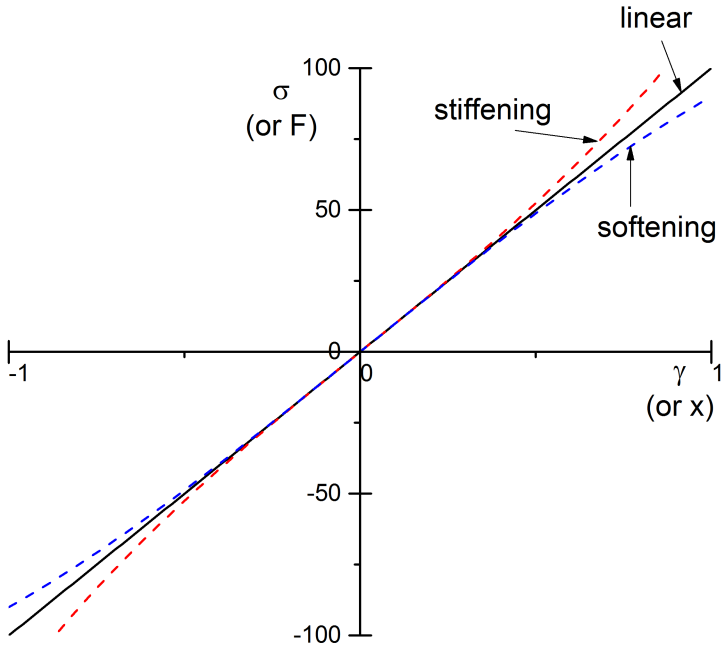

Figure 1.1: Stress response to strain for different nonlinearities. The black line is a purely linear elastic material, while the dashed lines represent a nonlinear response. The red line describes a stiffening response and the blue line represents a softening response.

for an elastic material is represented as

$$\begin{aligned} \sigma(\gamma) &= G(\gamma)\gamma \\ &= G_0\gamma\left(1 + b\gamma^2\right), \end{aligned} \tag{1.2}$$

where σ is the shear stress, G_0 is the linear elastic modulus, and γ is the shear strain. Here, b is analogous to the nonlinear parameter k_3 defined in Eqn. 1.1. Figure 1.1 shows how a stiffening or softening response represents a deviation from the linear response that increases with strain or displacement. Biological tissues exhibit complex rheological behavior, including strain-stiffening and -softening [8]–[14]. While some tissues soften and others stiffen, Storm et al. has shown that biological gels with networks composed of semiflexible filaments exhibit a stiffening response observable at some critical strain [8]. Observations such as these have motivated extensive research into nonlinear synthetic materials that can serve as models to better understand the mechanical properties of biological materials.

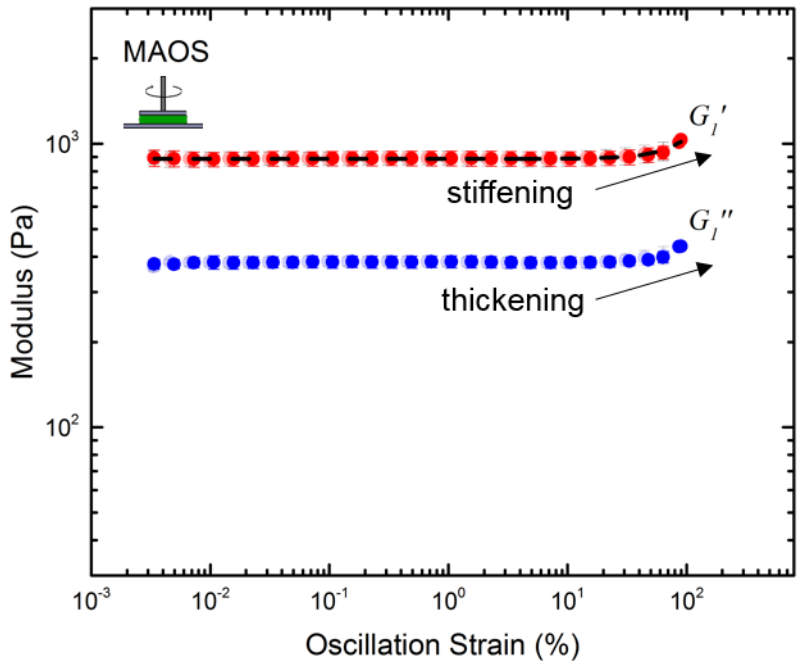

Figure 1.2: The response of a strain-stiffening and shear-thickening material under oscillatory shear. Material is a 2.75 wt% PVA with 1.25 wt% Borax polymer network (material details in Chapter 2).

Physical hydrogels have been an active area of research due to their complex rheological behavior including rich time and temperature dependence [15], [16], and nonlinear signatures including strain-stiffening and shear-thickening [17]–[21]. Just as strain-stiffening is a nonlinear *elastic* response, shear-thickening is a nonlinear *viscous* response. Oscillatory characterization allows for decoupling of such energy storage and loss properties (see Fig. 1.2). These observations have sparked research on how these material systems can be useful for various applications, including as possible candidates to serve as substrates for biological tissue engineering [18], as phantom tissue models for ultrasound elastography [20], and even as model materials for food gels and connecting rheological properties to sensory textures [22], [23]. While the nonlinear rheological properties for biological materials and physical hydrogels are well documented, the mechanism for strain-stiffening and shear-thickening is not always well understood.

This thesis aims to understand the mechanisms of strain-stiffening and shear-thickening often observed in transient or associative polymer hydrogels; specifically, Poly(vinyl) alcohol (PVA) transiently crosslinked

with Sodium tetraborate (Borax), or PVA-Borax. We use oscillatory shear rheology to measure asymptotically nonlinear material functions [24]. These material functions can be related to model parameters to gain physical insight into the structure of the material system. We argue that asymptotically nonlinear material functions are useful signatures for understanding the mechanisms driving nonlinearities arising from a change in structure.

1.1 Stiffening and Thickening Mechanisms

The structure of a physical hydrogel is described as a network of polymer chains that are physically crosslinked by crosslinks with a finite lifetime [15], [16]. The nonlinear response of a physical hydrogel is understood as a change in microstructure due to a deformation or flow imposed on the network [16]. Strain-stiffening and shear-thickening have largely been explained by two different mechanisms. One mechanism is the theory of stretch-induced structure formation due to an increase in the number of interchain crosslinks [25]–[27]. The other mechanism is attributed to the finite-extensibility of the polymer, in which the polymer chain is stretched into the non-Gaussian regime [28]–[30].

Recently, a model for a strain-stiffening transient polymer network was developed that is able to capture both mechanisms simultaneously [1]. We adopt the nomenclature from this model for the following discussion. Figure 1.3 is a theoretical schematic of the microstructural response by both mechanisms as a function of the stretch magnitude of a polymer chain between crosslink points, Q. Here, $h(Q)$ represents a nonlinear force extension law for the polymer chain, $F_s = h(Q)Q$, and $n(Q)$ represents the number density of elastic elements defined as a polymer chain carrying a nonlinear elastic restoring force between two crosslink points. Either, or both, of these microstructural responses invokes a bulk strain-stiffening response, as seen in Fig. 1.3. Since both microstructure parameters increase with stretch magnitude, Q, it is non-trivial to identify the dominating mechanism that drives the nonlinear response. We aim to identify regimes in which either mechanism can be rationalized as the more dominant one driving the nonlinear response. Our approach is to use oscillatory shear rheology across a range of compositions of PVA-Borax to study how nonlinear behavior changes as we change the concentrations of both PVA and Borax.

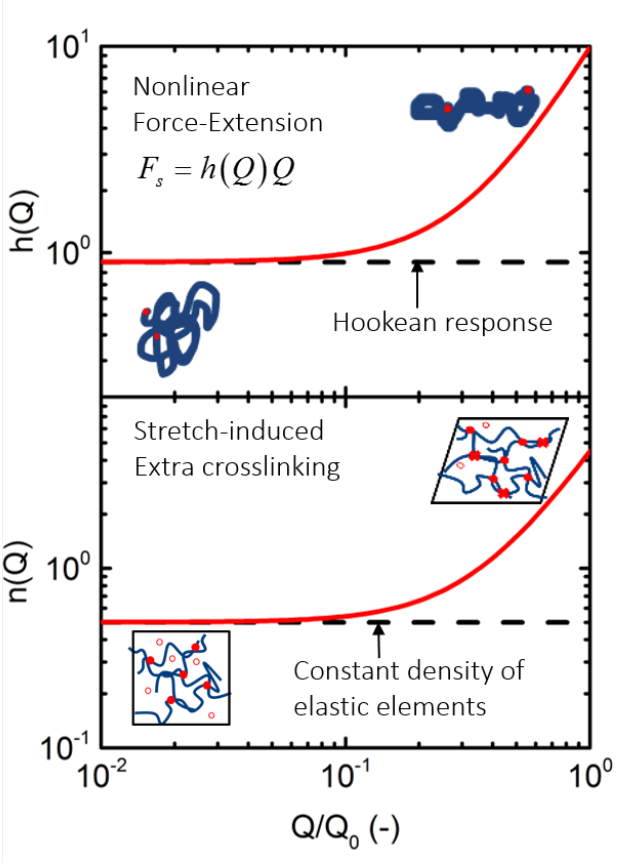

Figure 1.3: Theoretical response from a polymer chain carrying a nonlinear restoring force $h(Q)$ and from stretch-induced network formation $n(Q)$. Here Q_0 represents the maximum stretch of a polymer chain.

1.2 MAOS

Medium amplitude oscillatory shear (MAOS) is a testing protocol that probes the asymptotically nonlinear regime of a material system [24], [32]–[35]. The MAOS regime can be represented in a Pipkin space as shown in Fig. 1.4. The Pipkin space is a regime map for a viscoelastic response based on two input variables: strain amplitude γ_0, and angular frequency ω [36]. At a given frequency, the stress response becomes observably nonlinear as strain increases. The asymptotically nonlinear regime is the first order deviation from the linear regime; thus, it provides more information than the material functions extracted from small amplitude oscillatory shear (SAOS), while avoiding the high dimensionality and experimental artifacts of large amplitude oscillatory shear (LAOS) [37]–[41]. MAOS rheological signatures can be used for microstructural inference, model selection, and for fitting nonlinear model parameters for physical insight into

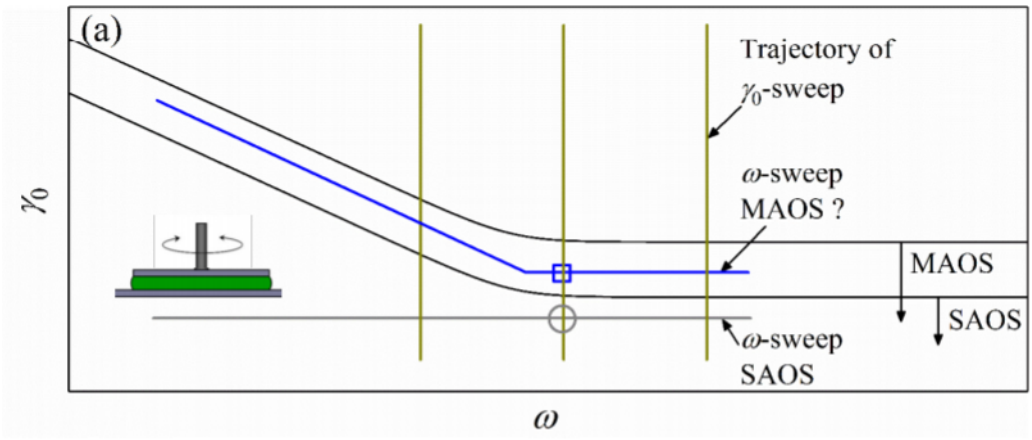

Figure 1.4: Pipkin space for a viscoelastic response. (With permission from Singh et al. [31]).

the material system [24], [33]–[35], [42].

The advantage of oscillatory shear measurements is the decomposition of the stress response into an elastic and viscous response. For a strain-controlled oscillatory shear measurement, the shear strain input is represented as

$$\gamma(t) = \gamma_0 sin(\omega t). \tag{1.3}$$

The shear stress response can be represented by a Fourier series involving higher harmonics,

$$\sigma(t) = \sum_n \sigma'_n sin(n\omega t) + \sigma''_n cos(n\omega t). \tag{1.4}$$

We choose the Chebyshev framework developed by Ewoldt and Bharadwaj [24], [38] to represent the power expansion of the measurable stress-harmonics,

$$\sigma'_1(\gamma_0, \omega) = G'(\omega)\gamma_0 + [e_1](\omega)\gamma_0^3 + O\left(\gamma_0^5\right) \tag{1.5}$$

$$\sigma''_1(\gamma_0, \omega) = G''(\omega)\gamma_0 + \omega\,[v_1](\omega)\gamma_0^3 + O\left(\gamma_0^5\right) \tag{1.6}$$

$$\sigma'_3(\gamma_0, \omega) = -\,[e_3](\omega)\gamma_0^3 + O\left(\gamma_0^5\right) \tag{1.7}$$

$$\sigma''_3(\gamma_0, \omega) = \omega\,[v_3](\omega)\gamma_0^3 + O\left(\gamma_0^5\right), \tag{1.8}$$

where prime denotes the elastic response, double prime represents the viscous response, and $G'(\omega)$ and $G''(\omega)$ are the linear viscoelastic material functions. The four nonlinear material functions are represented as $[e_1](\omega)$, $[v_1](\omega)$, $[e_3](\omega)$, and $[v_3](\omega)$, where e represents elastic and v represents viscous nonlinearities and the subscripts represent the harmonic of the input frequency. At a fixed frequency, the first- and third-harmonic moduli are defined by the measurable stresses in Eqns. 1.5-1.8 and are represented as

$$\begin{aligned} G_1'(\gamma_0, \omega_0) &= \frac{\sigma_1'}{\gamma_0} \\ &= G'_{LVE} + [e_1]|_{\omega_0} \gamma_0^2 + O\left(\gamma_0^4\right) \end{aligned} \tag{1.9}$$

$$G_1''(\gamma_0, \omega_0) = G''_{LVE} + \omega_0 \, [v_1]|_{\omega_0} \gamma_0^2 + O\left(\gamma_0^4\right) \tag{1.10}$$

$$G_3'(\gamma_0, \omega_0) = - \, [e_3]|_{\omega_0} \gamma_0^2 + O\left(\gamma_0^4\right) \tag{1.11}$$

$$G_3''(\gamma_0, \omega_0) = \omega_0 \, [v_3]|_{\omega_0} \gamma_0^2 + O\left(\gamma_0^4\right), \tag{1.12}$$

where G'_{LVE} and G''_{LVE} are the linear viscoelastic plateaus at the input frequency ω_0. At a given frequency, a strain-stiffening response is represented by a positive first-harmonic elastic nonlinearity $[e_1] > 0$; while a shear-thickening response is represented by a positive first-harmonic viscous nonlinearity $[v_1] > 0$ (see Fig. 1.2).

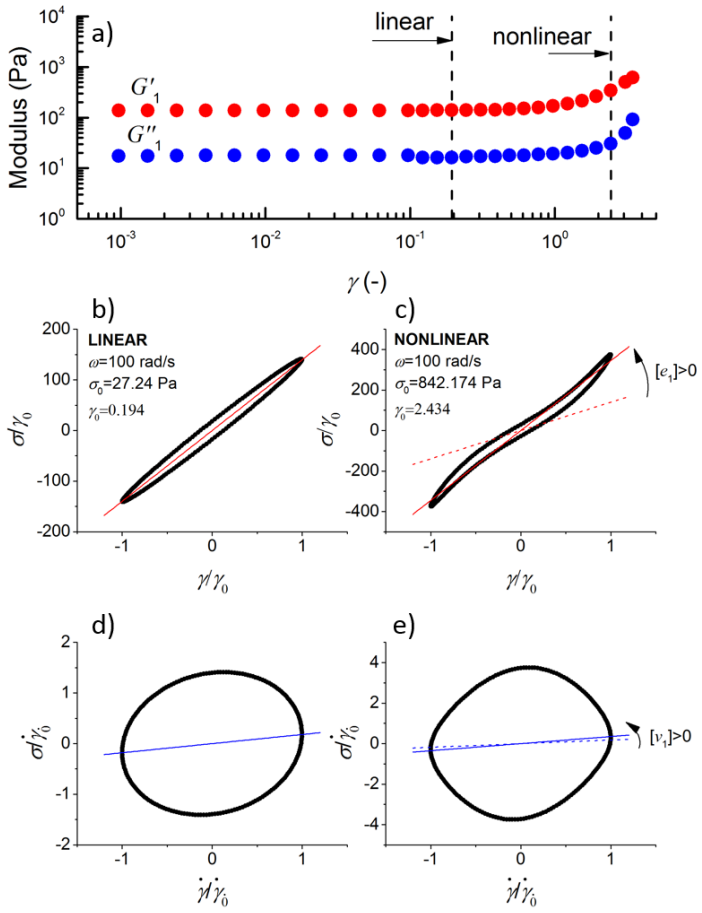

Figure 1.5: Strain amplitude sweep at $\omega = 100$ rad/s shown in (a). Elastic perspective of Lissajous curves at a strain amplitude in the linear and nonlinear regime shown in (b)-(c), respectively. The black lines represent the normalized stress response, while $\frac{\sigma}{\gamma_0} = G'_1 \frac{\gamma}{\gamma_0}$ is plotted as the solid red lines for each strain amplitude (dashed line in (c) is line seen in (b)). Similarly, the viscous perspective of the Lissajous curves are shown in (d) and (e), where $\frac{\sigma}{\dot{\gamma}_0} = \eta'_1 \frac{\dot{\gamma}}{\dot{\gamma}_0}$ is plotted as the blue lines. Analysis done with MITlaos software [43].

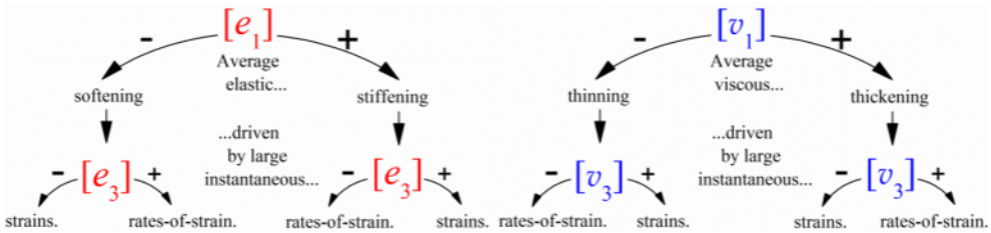

Figure 1.6: Sign interpretations of the four MAOS material functions. (With permission from Ewoldt et al. [24]).

The Chebyshev framework is used to provide sign interpretations of the four MAOS measures related to the rotation and distortion of Lissajous curves [24], as seen in Fig. 1.5. The signs of the first-harmonic asymptotic nonlinear functions dictate the rotation of a Lissajous curve from the linear response, while the signs of the third-harmonic asymptotic nonlinear functions define the concavity. Additionally, the signs of these material functions are used to determine if the nonlinear response is driven by strains or strain-rates (Figs. 6-7 in [24]). Furthermore, they can be related to model parameters to gain insight into the physical mechanisms driving the response [1]. A summary of the sign interpretations of the four MAOS measures are shown in Fig. 1.6 (from Fig. 7 in [24]). We measure the four MAOS measures across a range of compositions of PVA-Borax to determine how the nonlinear signatures change as a function of the concentrations of PVA and Borax, and to infer molecular features.

1.3 Chapter Summary

We aim to distinguish regimes in which one of the two strain-induced stiffening and thickening mechanisms is the more dominant one responsible for the nonlinear response of a physical hydrogel. In Chapter 2 we discuss the characteristics of our model material: PVA-Borax. In addition, we outline the two rheometry methods used for testing the material and extracting material functions. Our main results are discussed in Chapter 3, in which a novel approach was used for measuring asymptotic nonlinear material functions. We infer molecular and network features using a nonlinear transient polymer network model. In Chapter 4, we validate the model by using first-harmonic MAOS measures to predict third-harmonic MAOS via a single nonlinear model parameter. A universal nonlinear stiffening parameter is defined in Chapter 5, where we compare the nonlinearity of various materials using this low-dimensional material parameter. Finally, we discuss our conclusions and future outlook in Chapter 6.

Chapter 2

Material and Rheometry Methods

Rheological measurements were performed on a separated motor-transducer rotational rheometer (ARES-G2, TA Instruments) for data discussed in Chapter 3. Complementary data that will be discussed in Chapter 4 were collected using a combined motor-transducer rotational rheometer (DHR-3, TA Instruments). Strain controlled experiments were performed on a transiently crosslinked PVA-Borax system.

2.1 Model Material: PVA-Borax

A mixture of Poly(vinyl) alcohol (PVA) and Sodium tetraborate (Borax) is a well studied material system due to its physical and chemical properties [17], [44]–[48]. This transient polymer network is an ideal system for studying the mechanisms driving nonlinear viscoelasticity, as the system shows linear viscoelastic behavior and a single dominant relaxation timescale [49] in addition to nonlinear signatures when subjected to large strains [24], [35], [50]. A reversible hydrogel is formed by a di-diol complexation reaction, in which thermoreversible crosslinks form between two diol units of PVA with one borate ion, as seen in Fig. 2.1.

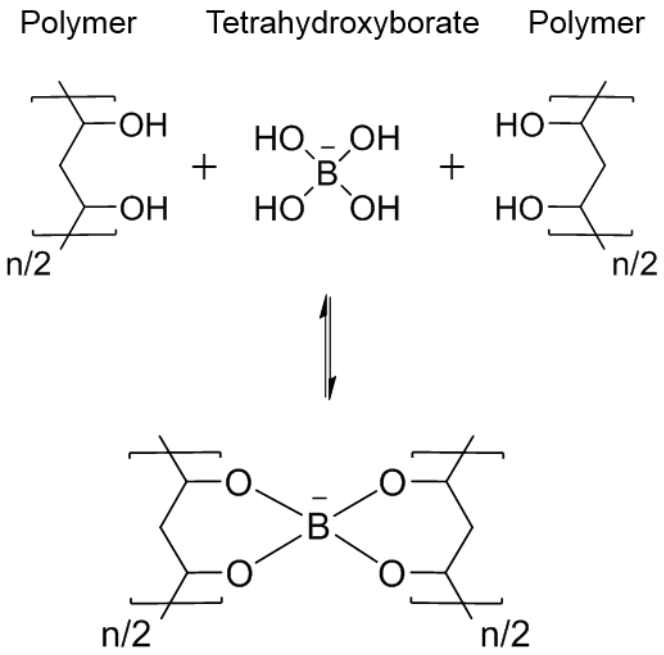

Figure 2.1: PVA-Borax crosslink reaction (di-diol). Here, n represents the number of monomers in a polymer chain.

Aqueous solutions of PVA (Aldrich Chemical Co., molecular weight $= 85,000 - 124,000$, 99+% hydrolyzed) were mixed with aqueous solutions of Sodium tetraborate, i.e. Borax (Aldrich Chemical Co.) to form multiple transient polymer networks with thermoreversible transient crosslinks. The mixture was prepared as follows. PVA was dissolved in deionized water under continuous stirring with a magnetic stir rod at a temperature of about 95°C until a homogeneous clear solution was obtained (approximately four hours) to form a 4 wt% stock solution. Borax was dissolved under similar conditions to form a 4 wt% stock solution. Throughout the stirring process the containers were sealed with layers of plastic film and aluminum foil to prevent evaporation loses. The solutions were allowed to cool to room temperature under ambient conditions and were mixed together in different ratios to form multiple compositions of a transient polymer network.

The final mixture was prepared by combining measured weights of each component in a closed test tube and stirring them until they were mixed thoroughly. We synthesized multiple compositions with varying

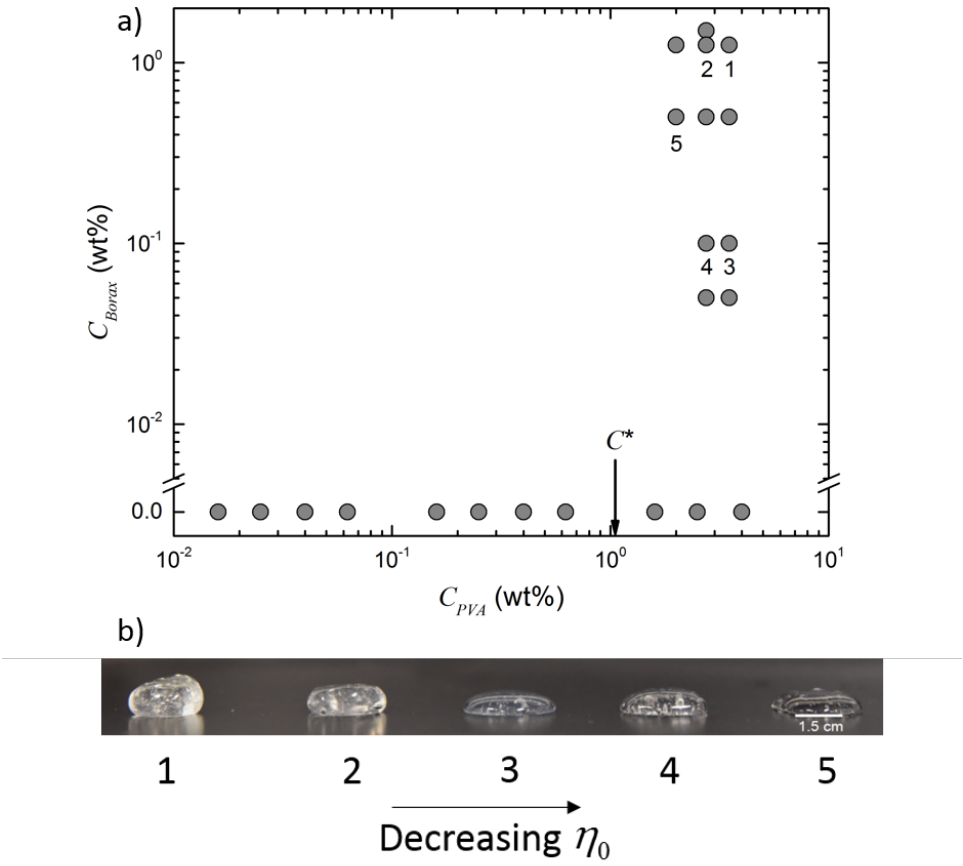

Figure 2.2: Compositions in which rheological data was collected shown in (a). Five of the compositions tested in (b) are labeled in (a) by decreasing zero-shear viscosity. The data at $C_{Borax} = 0$ were used to calculate the overlap concentration, $C^* = 1.06$ wt%.

concentrations of both PVA and Borax, as shown in Fig. 2.2. Depending on the combination of concentrations of PVA and Borax, it was noticed that the resulting mixture was always a viscous liquid, but sometimes with a high viscosity and noticeable elasticity (e.g. material could bounce off of a flat surface when dropped). Higher viscosity samples retaining air bubbles were centrifuged at 3000 rpm for 15 minutes (CL2 Centrifuge, Thermo Scientific) to remove any of those air bubbles before testing.

2.1.1 Measuring Overlap Concentration

To measure the overlap concentration C^*, concentration-dependent viscosity measurements for PVA solutions were performed on a flow-rate controlled internal flow viscometer (m-VROC, Rheosense) [51]. A

schematic of the device is shown in Fig. 2.3(a) (inset). Shear rate sweeps were performed on solutions of PVA at different concentrations (as shown in Fig. 2.2, where $C_{Borax} = 0$). Three repeat measurements were performed on each solution, and the average was taken as the mean viscosity shown in Fig. 2.3(a). The shear-sweep data is shown in Fig. A.1.

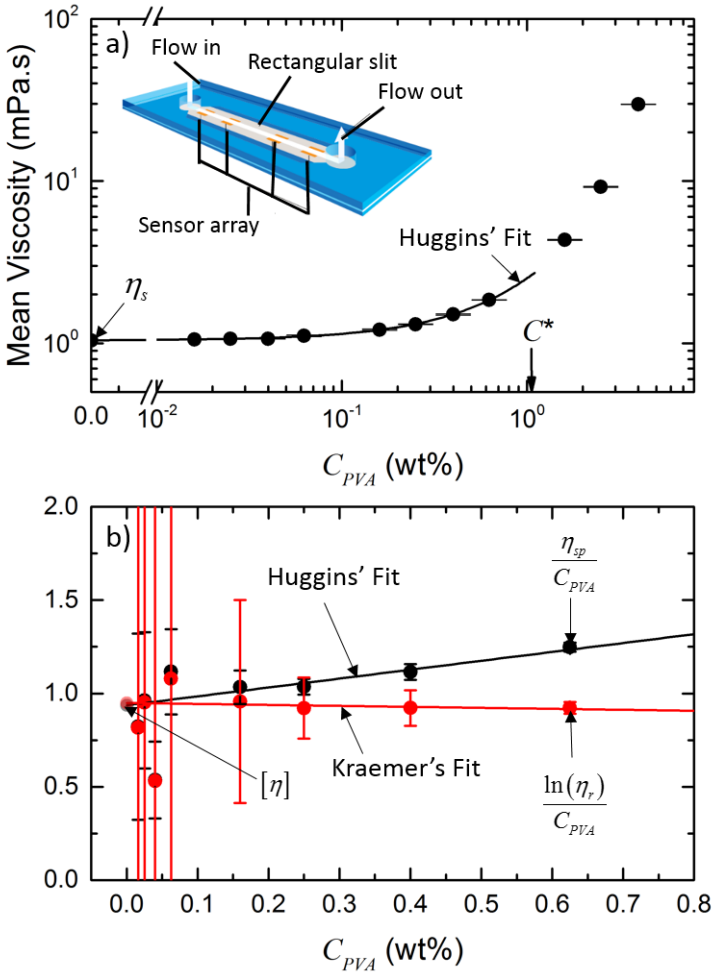

Figure 2.3: Viscosity measurements for different wt% concentrations of PVA shown in (a). Equations 2.1 and 2.2 are used to fit an intercept representing the intrinsic viscosity for the Huggins' and Kraemer's equation, respectively, as shown in (b). Here, $\eta_r = \frac{\eta}{\eta_s}$ and $\eta_{sp} = \eta_r - 1$ (see Eqns. 2.1 and 2.2). Inverting the intrinsic viscosity yields the overlap concentration, C^*, seen in (a). The inset in (a) is a schematic of how the m-VROC viscometer measures shear-rate sweep data [51].

By collecting mean viscosity data for a range of concentrations of PVA, we can estimate an intrinsic viscosity from the Huggins equation and the Kraemer's equation, respectively

$$\eta = \eta_s \left(1 + [\eta]\, C + k_H\, [\eta]^2\, C^2 + O\left(C^3\right)\right) \tag{2.1}$$

$$ln\left(\eta_r\right) = [\eta]\, C - k_K\, [\eta]^2\, C^2 + O\left(C^3\right), \tag{2.2}$$

where η is the measured viscosity, η_s is the solvent viscosity, $\eta_r = \frac{\eta}{\eta_s}$ is the relative viscosity, $[\eta]$ is the intrinsic viscosity, k_H is known as the Huggins' constant, k_K is the Kraemer's constant, and C is the concentration of the polymer solution.

The intrinsic viscosity represents asymptotic changes to viscosity due to an additive at mass concentration C (mass per volume) [52], [53]. This material parameter represents an inherent property of the system. The data in Fig. 2.3(b) are plotted so that $[\eta]$ appears as an intercept at $C_{PVA} = 0$, i.e. Eqns. 2.1 and 2.2 are re-arranged as

$$\frac{\frac{\eta}{\eta_s} - 1}{C_{PVA}} = \frac{\eta_{sp}}{C_{PVA}} = [\eta] + k_H\, [\eta]^2\, C_{PVA} + O\left(C_{PVA}^2\right)$$

and

$$\frac{ln\left(\eta_r\right)}{C_{PVA}} = [\eta] - k_K\, [\eta]^2\, C_{PVA} + O\left(C_{PVA}^2\right).$$

The value of $[\eta] = 0.943 \pm 0.008$ 1/wt% was found from fitting both equations and averaging the results. Taking the inverse of the intrinsic viscosity yields an estimate for the overlap concentration of the polymer system [54]. We measured an overlap concentration of

$$\begin{aligned} C^* &= \frac{1}{[\eta]} \\ &= 1.06\, wt\% \\ &\approx 1.08 \times 10^{-2} \frac{g}{mL}. \end{aligned}$$

The measured value is remarkably close to the value $C^* = 1.03 \times 10^{-2} \frac{g}{mL}$ estimated by Cheng [55].

The overlap concentration C^* represents the critical concentration above which the polymer solution is in a semi-dilute unentangled regime due to the onset of chain interpenetration [56], [57]; however, the

polymer system is not yet entangled. The critical entanglement concentration is approximately 4-10 times the overlap concentration [58]. The compositions tested in MAOS are all above the critical overlap concentration, and thus have the potential to form inter-chain crosslinks and percolate a network (see Fig. 2.2). Furthermore, all compositions tested are below the critical entanglement concentration. This is important to our study of the mechanisms driving nonlinear elasticity because the material functions are dictated by the transient crosslinks instead of polymer entanglements.

2.2 Rheometry Methods

Measurements and parameter extractions were made using two different protocols. MAOS data were collected using either the conventional strain-sweep testing protocol for extracting nonlinear parameters, or, for the main results, using a new frequency-sweep MAOS method [31]. Both testing protocols and methods for parameter extraction will be discussed in the following sections.

2.2.1 ARES-G2 - Main Results

Measurements for the data shown in Chapter 3 were performed on a strain-controlled separated motor-transducer rotational rheometer (ARES-G2, TA Instruments) using a plate-plate geometry (diameter 50mm) at 25°C maintained by a Peltier system in the lower plate. A parallel plate geometry allows for faster material loading at the expense of a spatially inhomogeneous strain field [39], [59] which affects MAOS measurements. Thus, we apply single point corrections to account for the spatial inhomogeneity of the strain field [60]. For each test, if the sample had a relatively low viscosity it was poured onto the bottom plate; otherwise, the sample was cut, scooped and placed onto the bottom plate with a spatula. The upper geometry was slowly lowered onto it with a maximum normal force of 1 N to prevent stress build-up in the sample. Once the upper geometry was lowered enough to slightly overfill the gap, the sample was trimmed to ensure a proper fill and mineral oil was applied to the outer edge to prevent evaporation losses. Prior to starting any tests, the sample was allowed to relax for 15 minutes to ensure a fully relaxed sample.

The testing protocol for data collected on the ARES-G2 follows the MAOS frequency-sweep procedure developed by Singh and Ewoldt [31]. This technique is advantageous compared to the conventional strain-sweep method for extracting material functions because it is faster and material economical. The

protocol is summarized as follows. Strain-sweeps were performed at 0.3 rad/s and 30 rad/s to identify both the linear and asymptotically nonlinear regimes. Reversibility was checked by performing a forward and reverse sweep. Next, we measured the linear viscoelasticity across a range of frequencies by performing a frequency-sweep in the SAOS regime with a strain amplitude chosen from the linear plateaus identified from the strain-sweeps. Finally, we performed a frequency-sweep in the MAOS regime at non-constant strain amplitudes, $\gamma_0(\omega)$, with the strain and strain-rate amplitudes chosen from the "sweet spot" measured from the strain-sweeps. In theory, this "sweet spot" should follow a trajectory within the MAOS regime shown in Fig. 1.4.

2.2.1.1 MAOS Material Functions Extraction

The first-harmonic intrinsic nonlinearities were calculated using both SAOS and MAOS frequency-sweeps, while the third-harmonic intrinsic nonlinearities were calculated using only the MAOS frequency-sweep [31],

$$[e_1](\omega) = \frac{G'_{1,M} - G'_{1,S}}{\gamma_M^2} \tag{2.3}$$

$$[v_1](\omega) = \frac{G''_{1,M} - G''_{1,S}}{\omega\gamma_M^2} \tag{2.4}$$

$$[e_3](\omega) = -\frac{G'_{3,M}}{\gamma_M^2} \tag{2.5}$$

$$[v_3](\omega) = \frac{G''_{3,M}}{\omega\gamma_M^2}. \tag{2.6}$$

These equations were derived by neglecting higher order terms, $O\left(\gamma_0^4\right)$, and solving for the four MAOS material functions in Eqns. 1.9-1.12, where the first- and third-harmonic moduli are measured in the MAOS regime; thus, the moduli and strain amplitude γ have an additional subscript M in Eqns. 2.3-2.6. Furthermore, we assume the linear viscoelastic plateaus (G'_{LVE} and G''_{LVE} in Eqns. 1.9 and 1.10) are accurately measured from the SAOS frequency-sweep; thus, they are represented as $G'_{1,S}$ and $G''_{1,S}$ in Eqns. 2.3 and 2.4. In conclusion, we are able to measure all four MAOS material functions across a range of frequencies with just two frequency-sweeps.

2.2.2 DHR-3 - Complementary Data

Measurements for the complementary data shown in Chapter 4 were performed on a stress-controlled combined motor-transducer rotational rheometer (DHR-3, TA Instruments) using a plate-plate geometry (diameter 40mm, sandblasted) at 25°C maintained by a Peltier system in the lower plate. The loading protocol was similar to the one previously stated for the ARES-G2; however, instead of using mineral oil to prevent evaporation losses, we used a solvent trap.

We use the conventional strain-sweep method for MAOS material function extraction. The testing protocol for data collected on the DHR-3 is described as follows. A forward and reverse strain-sweep was performed at 10 rad/s to check reversibility, and to identify both the linear and asymptotically nonlinear regimes. Linear viscoelasticity was measured by performing a SAOS frequency-sweep at a strain chosen from the linear regime.

2.2.2.1 MAOS Material Functions Extraction

We fit Eqns. 1.9 and 1.10 to the strain-sweep data performed at $\omega_0 = 10$ rad/s. The fitting parameters were the linear plateaus G'_{LVE} and G''_{LVE}, as well as the first-harmonic intrinsic nonlinearities $[e_1]|_{\omega_0}$ and $[v_1]|_{\omega_0}$. Since we are fitting for the intrinsic nonlinearities, we fit data in the limit of the asymptotic expansion by choosing an arbitrary threshold and neglecting all data at higher strain amplitudes. We define the threshold for the asymptotic expansion as a 10% deviation from the observed linear plateau. In other words, we fit data up to a strain amplitude in which the apparent moduli are $G'_1 \approx \pm 1.10 \times G'_{LVE}$ and $G''_1 \approx \pm 1.10 \times G''_{LVE}$, respectively.

It is important to note that only one value of the frequency-dependent first-harmonic intrinsic nonlinearities $[e_1](\omega)$ and $[v_1](\omega)$ can be measured from a strain-sweep. As a result, we have one first-harmonic intrinsic measurement at 10 rad/s from the experiments performed on the DHR-3. In Chapter 4, we show that a single first-harmonic MAOS measurement at 10 rad/s is able to predict "unseen" third-harmonic MAOS signatures observed at 30 rad/s via a single nonlinear model parameter.

Chapter 3

Universal Scaling of MAOS for PVA-Borax Indicates Microstructural Mechanism of Nonlinearity

In this chapter, we seek to understand the mechanisms of strain-stiffening and shear-thickening often observed in transient or associative polymer hydrogels; specifically, PVA-Borax. We use medium amplitude oscillatory shear (MAOS) as a tool to measure asymptotically nonlinear viscoelastic material functions across a range of compositions of PVA-Borax with storage moduli ranging from $G_0 \approx 100 - 3000$ Pa by varying the concentrations of both polymer (PVA) and crosslinker (Sodium tetraborate). Linear viscoelastic frequency-dependent material functions were scaled by two degrees-of-freedom, using G_0, η_0, and $\lambda_0 = \frac{\eta_0}{G_0}$. Asymptotically nonlinear MAOS measures were scaled by $\lambda_0 = \frac{\eta_0}{G_0}$ and $[e_3]_\infty$. Using the strain-stiffening polymer network model of Bharadwaj et al. [1], we demonstrate that a single nonlinear parameter scales nonlinearities and argue that finite extensibility is the sub-dominant cause of nonlinearity ($< 5\%$) compared to stretch-induced crosslinking.

Rheological measurements were performed following the protocol discussed in Section 2.2.1. Strain controlled LAOS tests were performed to identify the linear and the asymptotically nonlinear regimes for SAOS and MAOS frequency-sweeps, respectively. Constant amplitude frequency-sweeps were performed at a strain amplitude consistent with the linear regime to identify a high frequency plateau modulus and a steady shear viscosity. Non-constant amplitude frequency-sweeps were performed at a strain and strain-rate chosen from the MAOS regime to extract the four MAOS material functions following the procedure

discussed in Section 2.2.1.1. This protocol was used for all eleven compositions of PVA-Borax (see Fig. 2.2 for composition map).

3.1 Linear Viscoelastic Results

To identify the linear viscoelastic (SAOS) regime, two strain-sweeps were performed at fixed frequencies of 0.3 rad/s and 30 rad/s. Strain-sweeps were carried out starting from $\gamma_0 = 0.1\%$ until deviations were observed from a linear behavior. A strain amplitude γ_0 was chosen from the linear viscoelastic regime for the SAOS frequency-sweep for each composition tested. The frequency-sweep was carried out from $\omega = 0.1$ to $\omega = 100$ rad/s.

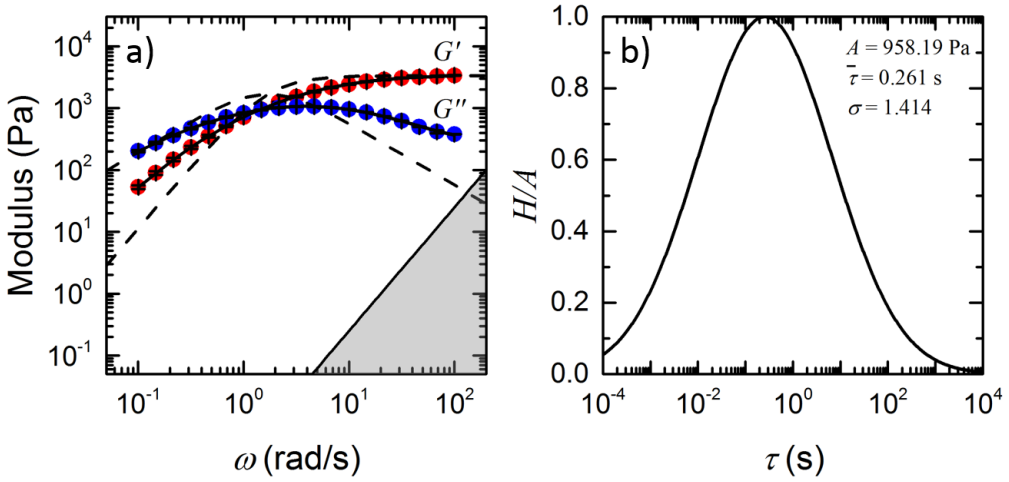

Figure 3.1: SAOS frequency-sweep on 3.5 wt% PVA with 1.25 wt% Borax shown in (a). Error bars from average of three measurements. Solid fit line is from a log-normal continuous spectrum model, shown in (b), which has three fit parameters: A, $\bar{\tau}$, and σ. Dashed fit line from a single mode Maxwell model, where the parameters taken from the linear plateau modulus G_0 and the steady shear viscosity η_0. The material inertial limit is shown in (a) [41].

Figure 3.1(a) shows the SAOS frequency-sweep for 3.5 wt% PVA with 1.25 wt% Borax. A single dominant timescale is apparent. This can be described by a log-normal relaxation spectrum with only three parameters: the maximum of the relaxation spectrum $H_{max} = A$, the maximum of the relaxation time $\bar{\tau}$, and the spread of the spectrum σ. Alternatively, the dominant timescale can be more approximated by a single mode Maxwell model, as shown by Bharadwaj et al. [1]. We will show that the two-degree-of-freedom description is sufficient to collapse data onto master curves of G' and η'. A log-normal continuous spectrum

(shown in Fig. 3.1(b)) was fit to the storage and loss moduli (G' and G'') [61]. We recast the loss modulus G'' data to its viscous perspective $\eta' = \frac{G''}{\omega}$ to identify a low-frequency plateau representing the steady shear viscosity η_0 of the material system (Fig. 3.2). Additionally, we identify the high-frequency plateau of the storage modulus G' to extract a plateau modulus G_0 representing the elastic modulus of the material at high frequencies. Using the two linear parameters G_0 and η_0, we can define a single mode Maxwell model to approximately describe the SAOS moduli (Fig. 3.1(a), dashed lines). The SAOS data for all compositions are shown in Appendix B.1.

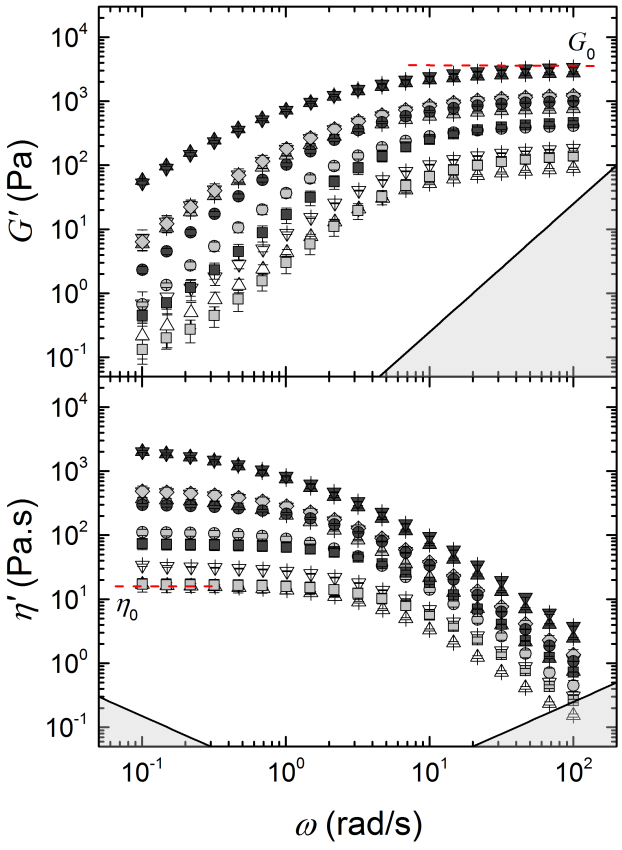

Figure 3.2: SAOS frequency-sweep on multiple compositions of PVA-Borax at a strain chosen from the linear regime. Error bars are the standard deviations from three repeat measurements. Symbol colors represent different wt% of PVA: white (2 wt%), light grey (2.75 wt%), dark grey (3.5 wt%). Symbol shapes represent different wt% of Borax: square (0.05 wt%), circle (0.1 wt%), up triangle (0.5 wt%), down triangle (1.25wt %), diamond (1.5wt %). The low torque limit and material inertial limit are shown in both figures [41].

From the two linear material parameters $\{G_0, \eta_0\}$, we calculated a characteristic relaxation timescale

$\lambda_0 = \frac{\eta_0}{G_0}$ for each composition. The relaxation timescale is a measure for the timescale at which a viscoelastic fluid will either exhibit a more dominant elastic response, or, a more dominant viscous response. Thus, at high frequencies PVA-Borax behaves more like an elastic solid with a modulus of G_0, while at low frequencies the material behaves more like a viscous fluid with a steady shear viscosity of η_0. Figure 3.2 shows the SAOS frequency-sweep for all compositions, and the linear parameters for all compositions are shown in Table 3.1.

Table 3.1: Summary of linear viscoelastic parameters for each composition. Errors are the standard deviations from three repeat measurements.

Composition (PVA wt% : Borax wt%)	G_0 (Pa)	η_0 (Pa.s)	λ_0 (s)
2 : 0.5	87.40 ± 3.64	16.73 ± 1.81	0.193 ± 0.013
2 : 1.25	178.98 ± 2.53	33.18 ± 1.01	0.185 ± 0.005
2.75 : 0.05	135.25 ± 20.42	16.93 ± 4.10	0.124 ± 0.012
2.75 : 0.1	406.95 ± 29.69	111.18 ± 12.96	0.274 ± 0.034
2.75 : 0.5	760.83 ± 20.80	364.16 ± 13.83	0.479 ± 0.005
2.75 : 1.25	1135.30 ± 47.04	469.11 ± 26.12	0.413 ± 0.006
2.75 : 1.5	1208.93 ± 161.41	479.05 ± 98.37	0.394 ± 0.027
3.5 : 0.05	452.76 ± 34.61	72.73 ± 13.71	0.160 ± 0.017
3.5 : 0.1	989.12 ± 22.26	294.35 ± 17.18	0.297 ± 0.011
3.5 : 0.5	2751.60 ± 119.27	1948.37 ± 132.46	0.708 ± 0.023
3.5 : 1.25	3336.06 ± 46.21	1942.36 ± 72.68	0.582 ± 0.014

For a fixed concentration of crosslinker, C_{Borax}, the linear parameters all increase as the concentration of polymer is increased, as seen in Fig. 3.3. Similarly, the linear parameters increase as the crosslinker concentration is increased; however, the linear parameters appear to approach a saturation value at higher concentrations of crosslinker. This suggests that for a fixed concentration of polymer, there is a limit in which any increase in C_{Borax} has little effect to the network formation.

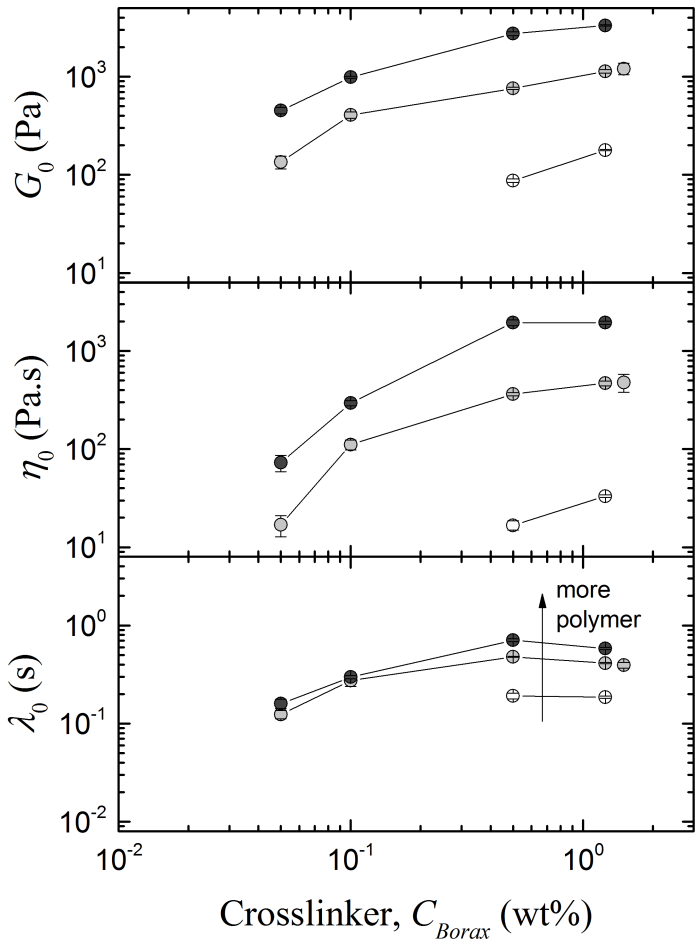

Figure 3.3: Linear parameters G_0, η_0, and $\lambda_0 = \frac{\eta_0}{G_0}$ as a function of crosslinker concentration C_{Borax}. Symbol colors represent different wt% of PVA: white (2 wt%), light grey (2.75 wt%), dark grey (3.5 wt%).

Figure 3.4 shows the linear viscoelastic frequency-dependent material functions normalized by the linear parameters G_0, η_0 and $\lambda_0 = \frac{\eta_0}{G_0}$ (given in Table 3.1). Remarkably, all compositions collapse across all frequencies to form a universal curve which suggests self-similarity of the material system at these compositions. The data will collapse at low and high frequencies by the definition of the normalization; however, this does not mean it should collapse at all frequencies. The collapse at intermediate frequencies suggests a self-similar distribution of relaxation timescales at all tested concentrations, e.g. as governed by the transient crosslink kinetics. It is important to note that only two degrees of freedom collapse the data, since λ_0 is not linearly independent from η_0 and G_0, $\lambda_0 = \frac{\eta_0}{G_0}$.

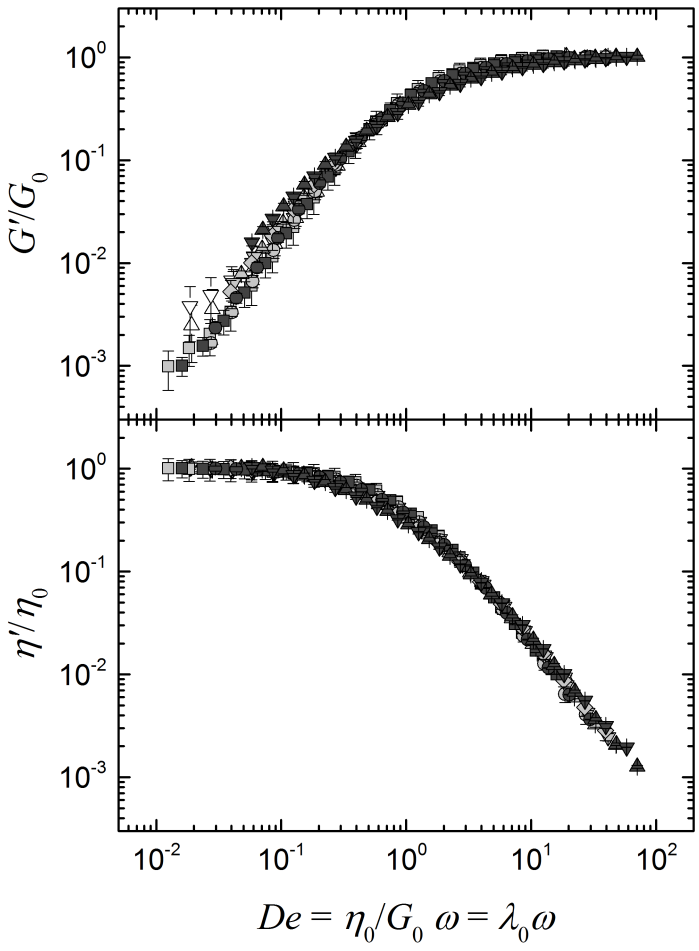

Figure 3.4: Frequency-dependent material functions G' and η' (Fig. 3.2) normalized by the linear parameters G_0 and η_0. Frequency is normalized by the relaxation timescale, $\lambda_0 = \frac{\eta_0}{G_0}$. Includes all 11 compositions shown in Table 3.1, with $C_{PVA} = 2C^* - 3.5C^*$ wt% and $C_{Borax} = 0.05 - 1.5$ wt%. Collapse of data suggests self-similarity.

3.2 Asymptotically Nonlinear Viscoelastic Results

To identify the asymptotically nonlinear (MAOS) regime, we analyze the strain-sweeps discussed in the previous section. The MAOS regime is identified by shear stress nonlinearities scaling as the power-law $\sigma \sim \gamma_0^3$, as seen in Eqns. 1.5-1.8 defining the first and third stress-harmonics. The range in which we see this power-law scaling has been called the "sweet spot" [31], where higher order $O(\gamma_0^5)$ terms are negligible, but the $O(\gamma_0^3)$ signals are above the minimum torque measurement resolution. MAOS frequency-sweeps are performed by following a strain-amplitude trajectory $\gamma_0(\omega)$ that stays in the sweet spot of each frequency to

extract the four MAOS material functions defined in Eqns. 2.3-2.6. The trajectory is defined by a constant strain γ_0 at high frequencies, followed by a constant strain-rate $\dot{\gamma}_0 = \gamma_0\omega$ at frequencies below some critical frequency (see Fig. 1.4). For each composition, the critical frequency we choose is the cross-over frequency from the SAOS frequency-sweep, where $G' = G''$.

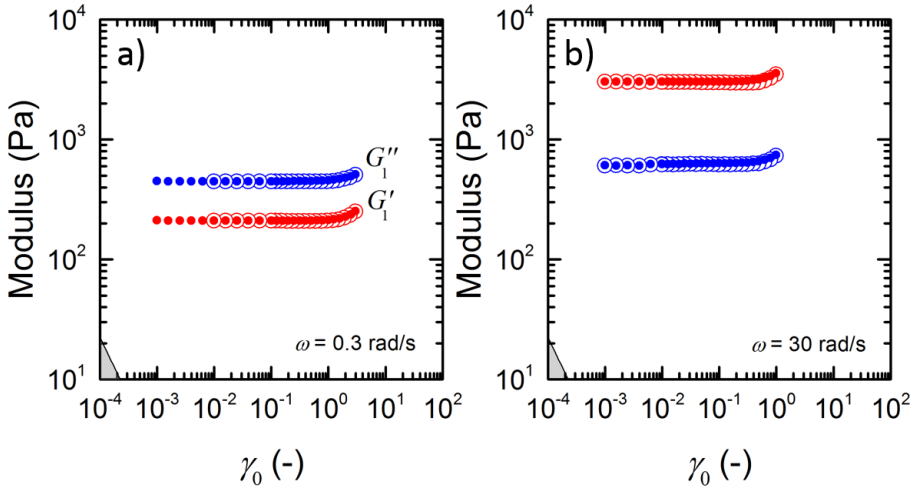

Figure 3.5: Strain-sweep on 3.5 wt% PVA with 1.25 wt% Borax at $\omega = 0.3$ rad/s in (a), and at $\omega = 30$ rad/s in (b). Solid symbols represent sweeping up γ_0, while open symbols represent sweeping down γ_0 to verify overlapping results.

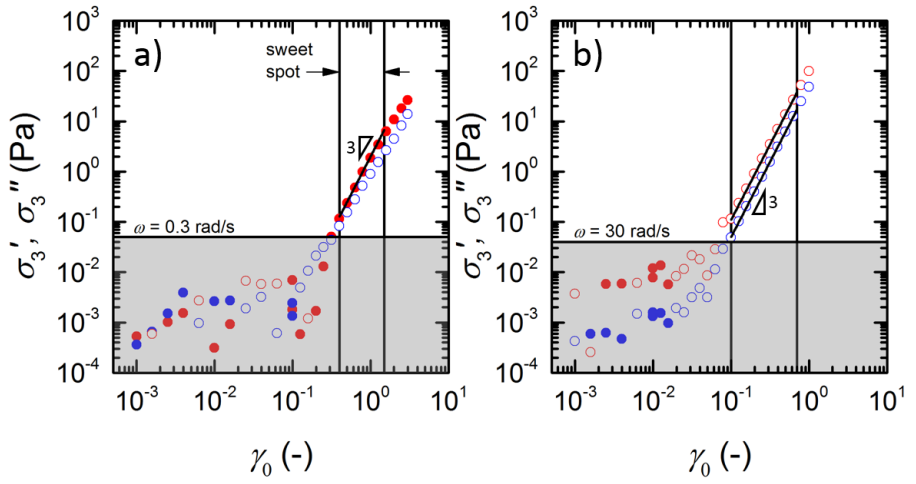

Figure 3.6: Third harmonic measurements from the strain-sweeps on 3.5 wt% PVA with 1.25 wt% Borax at $\omega = 0.3$ rad/s in (a), and at $\omega = 30$ rad/s in (b). Red symbols represent σ_3' and blue symbols represent σ_3'. Solid symbols represent positive values, while open symbols represent negative values.

Figure 3.5 shows the first-harmonic moduli for two strain-sweeps performed on 3.5 wt% PVA with 1.25 wt% Borax. Ramps up and down were performed to check for reversibility. The material exhibits both strain-stiffening and shear-thickening behavior at both frequencies. Since the material response is nonlinear, we can identify the MAOS regime from the third stress-harmonics shown in Fig. 3.6. The sweet spot for each strain-sweep is chosen as the range in which the third stress-harmonics show a power-law scaling $\sim \gamma_0^3$ and are above the minimum torque measurement resolution. We choose γ_0 for the MAOS frequency-sweep from the sweet spot identified in the high-frequency strain-sweep (Fig. 3.6(b)) such that, when multiplied by the cross-over frequency identified in the SAOS frequency-sweep (Fig. 3.1(a)), the strain-rate $\dot{\gamma}_0 = \gamma_0\omega$ will fall within the sweet spot at $\omega = 0.3$ rad/s (Fig. 3.6(a)). We performed a MAOS frequency-sweep following this $\gamma_0(\omega)$ trajectory. This procedure was used for all compositions of PVA-Borax. First-harmonic strain-sweep data for all compositions are shown in Fig. 3.7.

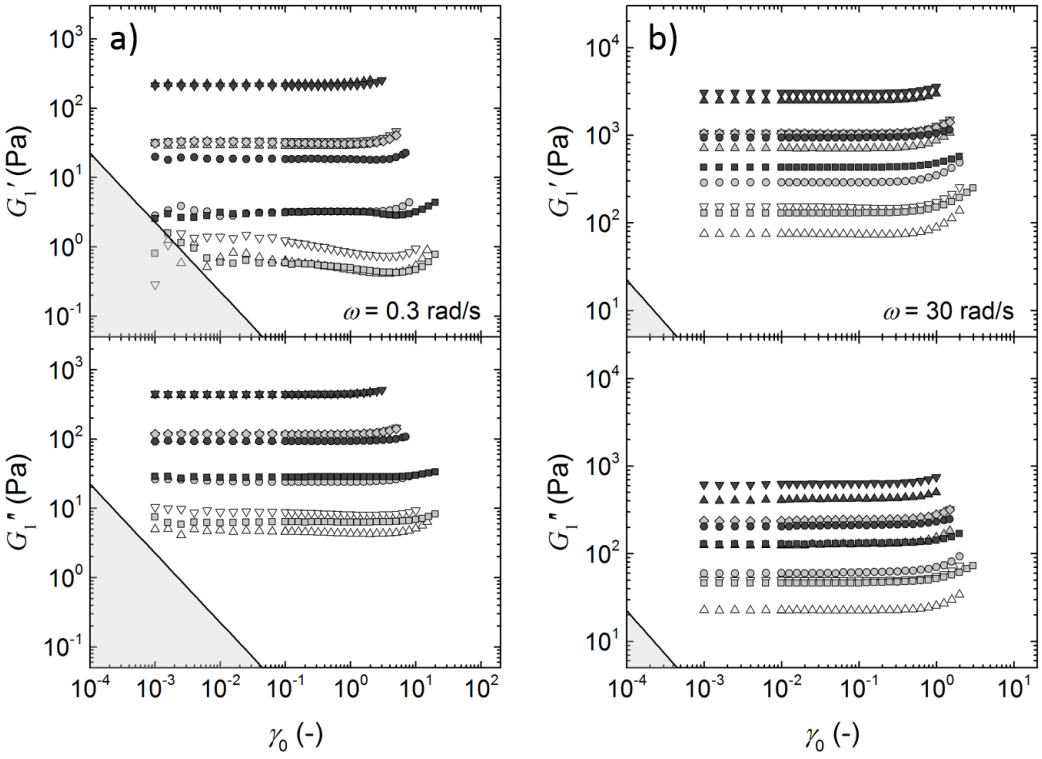

Figure 3.7: Strain-sweep on multiple compositions of PVA-Borax at 0.3 rad/s (a) and 30 rad/s (b). Symbols same as in Fig. 3.2. The low torque limit is shown [41].

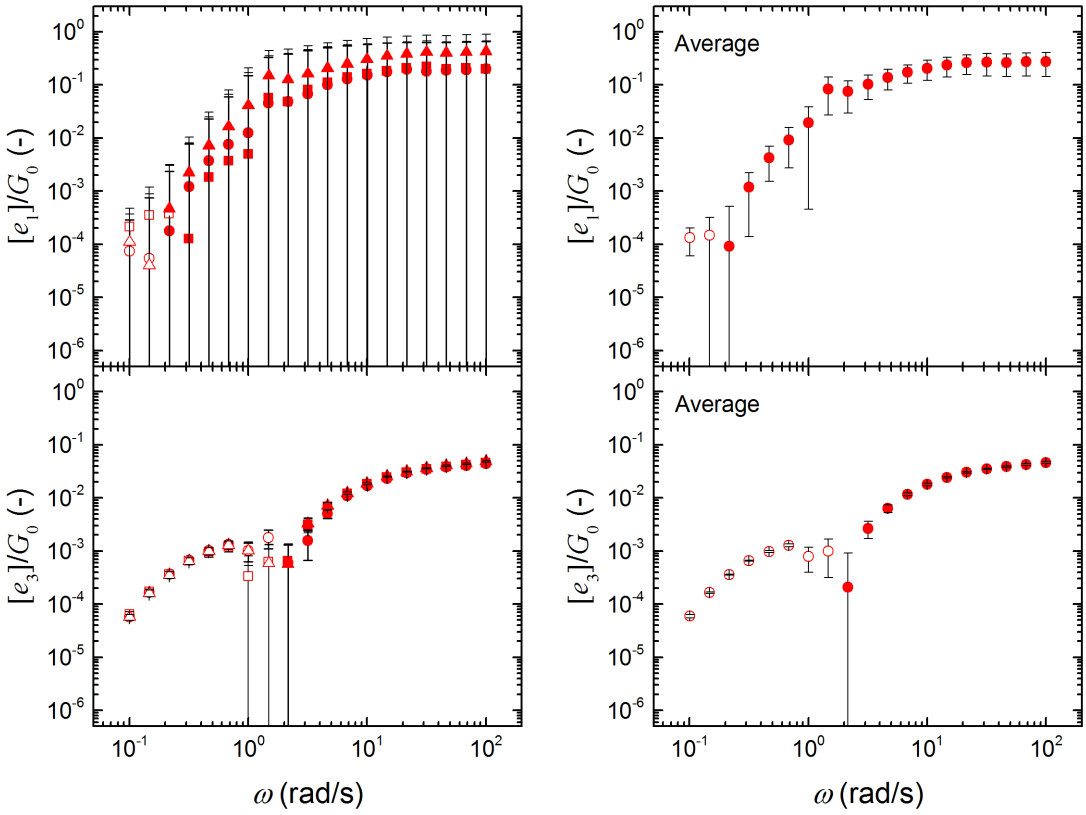

Figure 3.8: Measurements of the elastic MAOS material functions $[e_1]$ and $[e_3]$ normalized by the linear elastic modulus G_0 for 3.5 wt% PVA with 1.25 wt% Borax. The left column shows three measurements, where the error bars are from the error propagation using Eqns. 2.3 and 2.5. Error propagation is discussed in Appendix B.1.2. The right column shows the average of the measurements, where the error bars are the standard deviation.

The four MAOS material functions were calculated from the SAOS and MAOS frequency-sweeps using Eqns. 2.3-2.6 for all 11 compositions. The four MAOS measures for one example composition are shown in Figs. 3.8 and 3.9 for 3.5 wt% PVA with 1.25 wt% Borax. These rheological signatures can be interpreted by the signs of the MAOS material functions which relate to rotation and distortion of Lissajous curves (see Fig. 1.6). At high frequencies, the average elastic response is one of strain-stiffening and the average viscous response is one of shear-thickening ($[e_1] > 0$ and $[v_1] > 0$). At low frequencies, there is a frequency below which the average elastic response could be one of strain-softening ($[e_1] < 0$), while the average viscous response is one of the shear-thickening for all frequencies probed. There is a frequency, or timescale, in which the third-harmonic nonlinearities $[e_3]$ and $[v_3]$ change sign, which dictates whether the elastic and

viscous responses are driven by strains or strain-rates (see Fig. 1.6). This critical timescale may be different between the elastic and viscous responses, as is the case for 3.5 wt% PVA with 1.25 wt% Borax. Data similar to Figs. 3.8 and 3.9 for all compositions tested are shown in Appendix B.1.

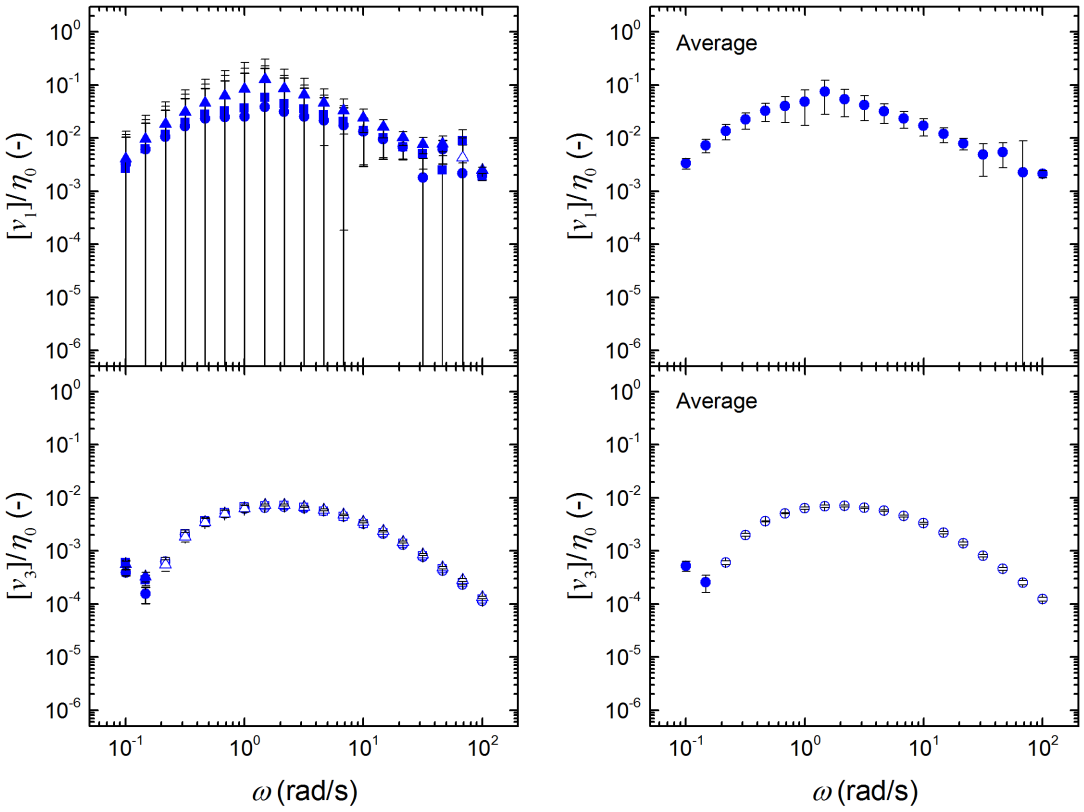

Figure 3.9: Measurements of the viscous MAOS material functions $[v_1]$ and $[v_3]$ normalized by the steady shear viscosity η_0 for 3.5 wt% PVA with 1.25 wt% Borax. The left column shows three measurements, where the error bars are from the error propagation using Eqns. 2.4 and 2.6. Error propagation is discussed in Appendix B.1.2. The right column shows the average of the measurements, where the error bars are the standard deviation.

At some frequencies, there is uncertainty about the signs of the MAOS nonlinearities, e.g. for $[e_1]$ where the material exhibits strain-stiffening or -softening elastic behavior, or for $[v_1]$ a shear-thickening or -thinning viscous behavior. Additionally, there is uncertainty on whether the response is driven by strain or strain-rates (signs of $[e_3]$ and $[v_3]$). This can be seen by the error bars extending past the lower limit of the vertical axis in Figs. 3.8 and 3.9, which represents uncertainty in whether the sign of the value is positive or negative. Another representation of this is shown in Fig. 3.10. We plot the relative error in the measurement

of the four MAOS material functions (using the average values in Figs. 3.8 and 3.9) across the frequency spectrum. If the relative error is greater than one, we are uncertain about the sign of the nonlinear parameters at that particular frequency.

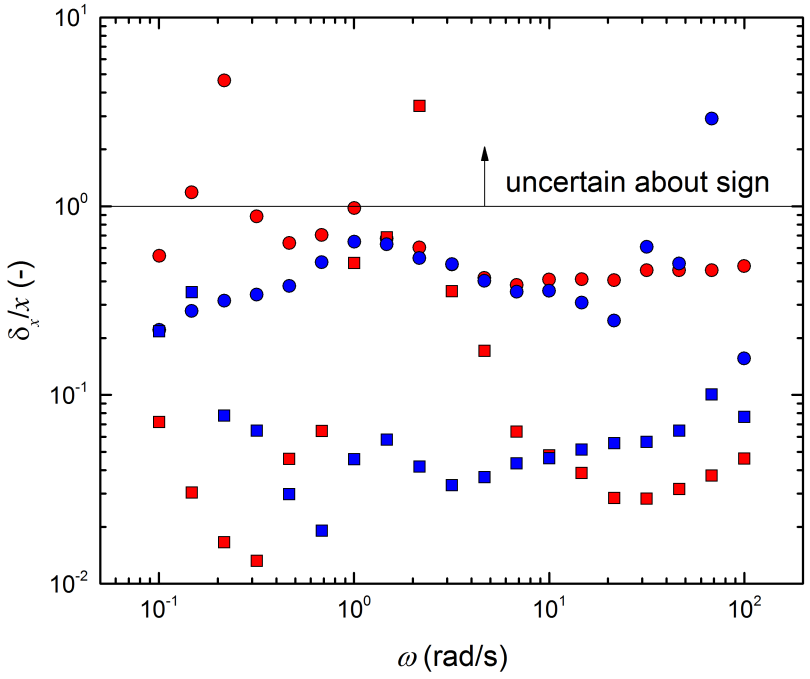

Figure 3.10: The relative error, $\frac{\delta_x}{x}$, for the four MAOS measures, where δ_x is the uncertainty in the measurement x and $x = \{[e_1], [v_1], [e_3], [v_3]\}$. We are uncertain of the sign for values greater than 1. Circles - first-harmonic nonlinear measures, squares - third-harmonic nonlinear measures. Red - elastic, blue - viscous.

We observed higher uncertainty with the first-harmonic MAOS measures relative to the third-harmonic nonlinearities across all compositions tested. We attribute this higher uncertainty to first-harmonic MAOS requiring a subtraction of the linear regime signal (e.g. see Eqns. 2.3 and 2.4), while third-harmonics are directly measurable (e.g. see Eqns. 2.5 and 2.6). Moreover, a full strain-sweep would improve the accuracy compared to the one-point and two-point MAOS frequency-sweep method for material parameter extraction (Eqns. 2.3-2.6). While the third-harmonic MAOS measures are directly measurable from third-harmonic stress responses, the calculation of the first-harmonic MAOS measures involve subtracting two numbers of similar order which introduces more error. For this reason we use the third-harmonic nonlinearities for our

detailed analysis here.

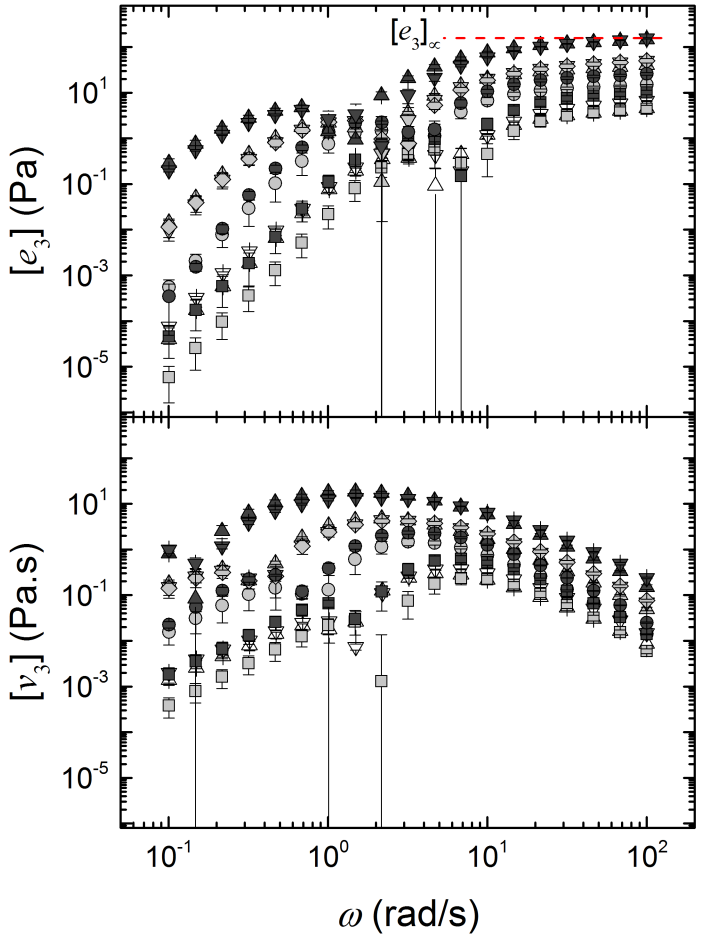

Figure 3.11: Third-harmonic MAOS measures calculated from SAOS and MAOS frequency-sweeps performed on multiple compositions of PVA-Borax. Error bars come from three repeat measurements. Symbols same as in Fig. 3.2.

Figure 3.11 shows the third-harmonic MAOS material functions for all 11 compositions and Fig. 3.12 shows the MAOS material functions normalized by the linear parameters G_0, η_0, and the linear relaxation timescale $\lambda_0 = \frac{\eta_0}{G_0}$, and a single nonlinear parameter χ, which we identify from $[e_3]_\infty = \lim_{De\to\infty}[e_3]$, as will be described. Remarkably, we see the data collapse, suggesting a self-similar material system across this wide range of compositions. It should be noted that the self-similarity is more evident from the elastic perspective, $\frac{[e_3]}{G_0}$. Although there is more scatter from the viscous contribution, $\frac{[v_3]}{\eta_0}$, it is noteworthy that the frequency-dependence collapses using only the linear timescale, and a single nonlinear measure is used

to vertically shift both $[e_3]$ and $[v_3]$. This is consistent with the structure-rheology model of Bharadwaj et al. [1].

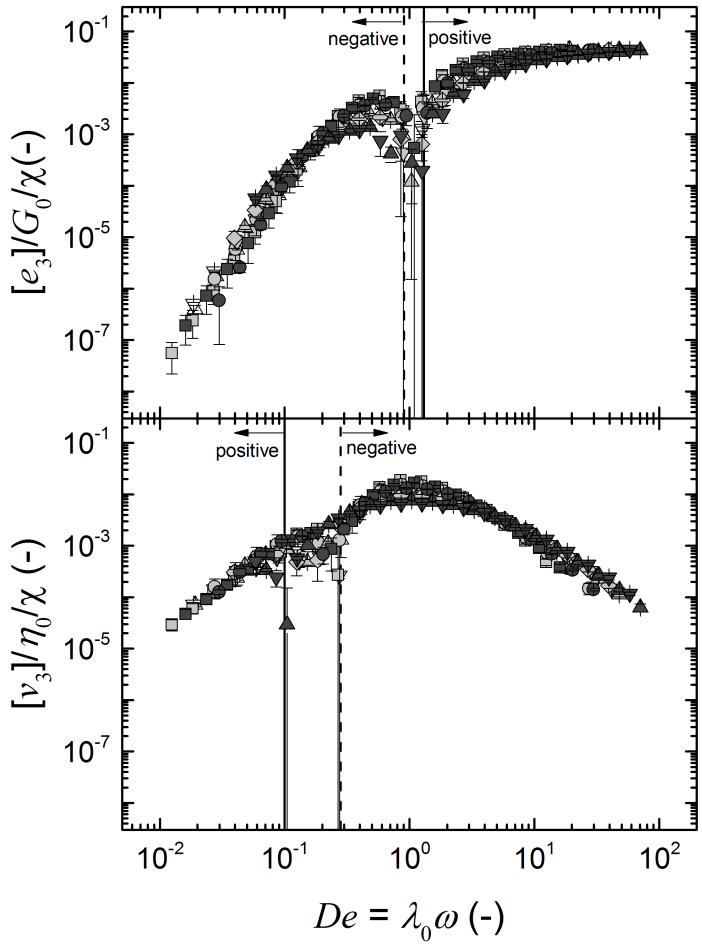

Figure 3.12: Third-harmonic MAOS material functions normalized by the linear parameters G_0 and η_0 and the nonlinear model parameter χ. Frequency is normalized by the relaxation timescale, $\lambda_0 = \frac{\eta_0}{G_0}$. Includes all 11 compositions shown in Table 3.1, with $C_{PVA} = 2C^* - 3.5C^*$ wt% and $C_{Borax} = 0.05 - 1.5$ wt%. Collapse of data suggests self-similarity.

We also note that the more coarse MAOS measure [33]

$$Q_0(\omega) = \frac{\sqrt{[e_3]^2 + \omega^2 [v_3]^2}}{\sqrt{G'^2 + G''^2}} \tag{3.1}$$

also shows universal scaling (see Fig. B.46). Clearly, this Q_0 representation of the third-harmonic MAOS

response is incomplete, not allowing for checking $[e_3]$ and $[v_3]$ responses separately (and losing sign information), and thus would generally be easier to show self-similarity. That our results with $[e_3]$ and $[v_3]$, across a wide range of De, show a universal scaling is a more robust test of the model of Bharadwaj et al. [1], and provides more insight to identify microstructural causes of the nonlinearity, as we will show.

3.3 Stiffening Mechanisms and Nonlinear Scaling

The material response of PVA-Borax exhibits a rich frequency-dependence due to its viscoelasticity, as is evident by the results discussed in the previous sections. At high Deborah number, $De = \lambda_0\omega >> 1$, the material behaves elastically with a linear shear modulus G_0 that asymptotically stiffens ($[e_1] > 0$) due to large strains (based on $[e_3] > 0$). This behavior is observed across all 11 compositions tested (see Table 3.1). To interpret the nonlinear results, we analyze the data through the lens of a recently developed model for a strain-stiffening transient polymer network developed by Bharadwaj et al. [1] and discussed in Chapter 1. The model describes viscoelastic nonlinearities across a range of frequencies based on a simple hypothesis of *stretch-induced stiffening* where stretch of elastic elements is governed by viscoelastic relaxation, and thus at low De stretch is caused by large strain-rates $\dot{\gamma}$, but at high De caused by large strains γ. The model involves a single nonlinear parameter, χ, which we calibrate to the data from the $[e_3]$ plateaus at high frequency, $[e_3]_\infty$ (see Fig. 3.11). This is similar to how we identify the two linear parameters η_0 and G_0 from observed plateaus, rather than curve fitting by minimizing residuals.

In the high De limit, the material response is approximated by Eqn. 1.2, where the modulus is a function of strain $G(\gamma) \approx G_0\left(1 + b\gamma^2 + O\left(\gamma^4\right)\right)$. The dimensionless coefficient b is a measure of the relative nonlinearity of the material, and is related to the linear shear modulus G_0 and the elastic MAOS measures by [1]

$$b = \frac{8}{5}\frac{\lim_{De\to\infty}[e_1](\omega)}{G_0} = 8\frac{\lim_{De\to\infty}[e_3](\omega)}{G_0}. \tag{3.2}$$

Furthermore, b is related to the nonlinear model parameter χ as [1]

$$b = \frac{1}{3}\chi, \tag{3.3}$$

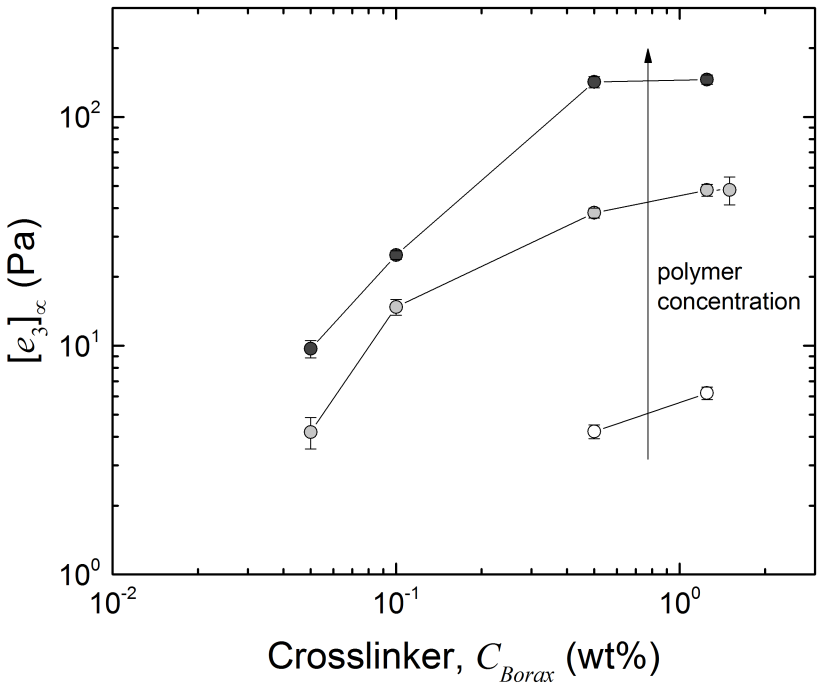

Figure 3.13: High-frequency plateau $[e_3]_\infty$ as a function of crosslinker concentration C_{Borax}. Symbol colors represent different wt% of PVA: white (2 wt%), light grey (2.75 wt%), dark grey (3.5 wt%).

and it can be seen that $[e_3]_\infty$ is related to χ as

$$\chi = 24\frac{\lim\limits_{De\to\infty}[e_3](\omega)}{G_0} = 24\frac{[e_3]_\infty}{G_0}. \tag{3.4}$$

We note that χ is used here in place of $\mathscr{H}$ in the paper discussing the model [1]. This single nonlinear parameter, χ, encodes both the elastic and viscous nonlinearities. The nonlinear response depends on the sign of χ. A stiffening response is represented as $\chi > 0$, or $b > 0$.

For each composition in Table 3.1, we calculate a χ value using Eqn. 3.4 by fitting a constant line to the high frequency plateau of $[e_3]$ seen in Fig. 3.11 as $[e_3]_\infty$. The values for each are shown in Figs. 3.13 and 3.14 as functions of C_{Borax}. It is important to note that the behavior of $[e_3]_\infty$ mirrors the behavior of the linear elastic shear modulus G_0 shown in Fig. 3.3. That is, G_0 and $[e_3]_\infty$ are correlated. The similarity is to be expected since G_0 sets the baseline of the stress response of the material, and the MAOS signatures are measures of the asymptotic deviation from the baseline response. This reinforces the idea that *relative*

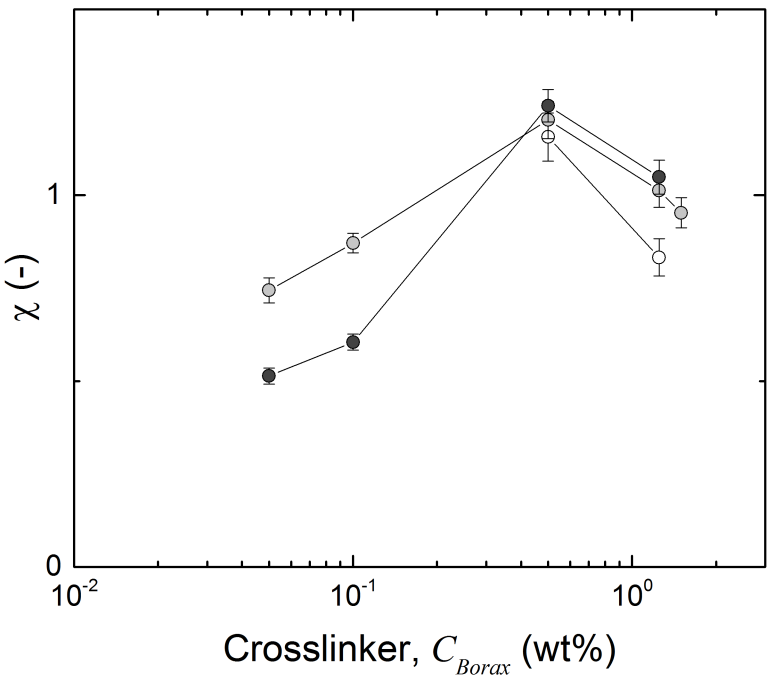

Figure 3.14: Nonlinear model parameter χ (from $[e_3]_\infty$ plateau) as a function of crosslinker concentration C_{Borax}. Symbol colors represent different wt% of PVA: white (2 wt%), light grey (2.75 wt%), dark grey (3.5 wt%).

nonlinearities, such as $\frac{[e_3]_\infty}{G_0}$, are important for comparing nonlinear strengths across material systems. Both b and χ are defined as relative nonlinearities (see Eqns. 3.2 and 3.4), as the nonlinear MAOS measure $[e_3]_\infty$ is normalized by the shear modulus G_0. Furthermore, it is observed that the nonlinear behavior of the *relative* nonlinearity does not follow, or, is not set by, the linear trends. While the linear and MAOS parameters (G_0 and $[e_3]_\infty$) tend to increase and approach a saturation value as a function of crosslinker (see Figs. 3.3 and 3.13), the relative nonlinearity χ increases to a maximum value and proceeds to decrease as a function of crosslinker (see Fig. 3.14). Table 3.2 shows a summary of the high-frequency elastic plateau $[e_3]_\infty$, as well as the computed relative nonlinearity model parameters b and χ for each compositon tested.

The model of Bharadwaj et al. [1] includes the possibility of multiple mechanisms of strain-stiffening in a transient hydrogel, as discussed in Chapter 1: the finite-extensibility of the polymer chains, and stretch-induced network structuring due to an increase in crosslink density. Theoretical curves describing stretch-dependent finite-extensibility, $h\,(Q)$, and stretch-induced network structuring, $n\,(Q)$, are shown in Fig. 1.3. Both the elastic shear modulus G_0 and the nonlinear model parameter χ are related to the stretch-dependent

Table 3.2: Summary of nonlinear parameters for each composition. The third-harmonic high-frequency plateau fit is represented as $[e_3]_\infty$, with the errors from fit. Corresponding model parameters b and χ calculated from Eqns. 3.2 and 3.3, with errors from error propagation discussed in Appendix B.1.1.

Composition (PVA wt% : Borax wt%)	$[e_3]_\infty$ (Pa)	b (-)	χ (-)
2 : 0.5	4.21 ± 0.29	0.386 ± 0.022	1.157 ± 0.065
2 : 1.25	6.21 ± 0.39	0.278 ± 0.017	0.833 ± 0.050
2.75 : 0.05	4.19 ± 0.66	0.248 ± 0.011	0.744 ± 0.034
2.75 : 0.1	14.77 ± 1.17	0.290 ± 0.009	0.871 ± 0.026
2.75 : 0.5	38.12 ± 1.91	0.401 ± 0.017	1.202 ± 0.050
2.75 : 1.25	47.91 ± 2.93	0.338 ± 0.015	1.013 ± 0.046
2.75 : 1.5	47.99 ± 6.73	0.318 ± 0.014	0.953 ± 0.041
3.5 : 0.05	9.69 ± 0.85	0.171 ± 0.007	0.514 ± 0.022
3.5 : 0.1	24.93 ± 1.05	0.202 ± 0.007	0.605 ± 0.022
3.5 : 0.5	142.26 ± 7.91	0.414 ± 0.014	1.241 ± 0.043
3.5 : 1.25	145.79 ± 6.65	0.350 ± 0.015	1.049 ± 0.046

driving mechanisms by

$$G_0 = \frac{1}{3} n\left(Q_{eq}\right) h\left(Q_{eq}\right) Q_{eq}^2, \tag{3.5}$$

$$\chi = \hbar + n, \tag{3.6}$$

where

$$\hbar = \left.\frac{\partial \ln h(Q)}{\partial \ln Q}\right|_{Q=Q_{eq}}, \tag{3.7}$$

$$n = \left.\frac{\partial \ln n(Q)}{\partial \ln Q}\right|_{Q=Q_{eq}}. \tag{3.8}$$

The shear modulus G_0 and nonlinear parameter χ are defined in the limits of zero strain, i.e. by the material characteristics at equilibrium, or more specifically, by the equilibrium stretch magnitude of a polymer chain between crosslinks Q_{eq}. All nonlinearities derive only from χ, i.e., from nonlinear elastic elements $\hbar$ or from stretch-induced network structuring from an increase in crosslink density n. From experimental measures of G_0 and χ, we can estimate molecular and network features including crosslink density n, the end-to-end distance between crosslinks Q_{eq}, and the ratio of the equilibrium end-to-end distance between crosslinks to the contour length between crosslinks, $\frac{Q_{eq}}{L}$. We follow the analysis done by Bharadwaj et al. [1] to estimate these parameters and compare them to values found in the literature. Throughout the

following analysis, we use the polymer (PVA) specific quantities and relations determined by ideal chain polymer physics ideas described by Eqns. (A58)-(A61) in the Appendix of [1], as well as in Appendix B.2.

To infer network features from experimental measurements of G_0 and χ we assume a functional form for $h(Q)$ describing the nonlinear behavior of the elastic elements. The FENE model is an analytical approximation to the inverse Langevin function which describes the force-extension behavior of a single polymer coil [59], [62]. The FENE model has been shown to capture the response of linear flexible polymers subject to small and large deformations [59]; therefore, it is reasonable to assume that this model is suitable for capturing the linear and asymptotically nonlinear response of a PVA polymer network. The functional form for an elastic element carrying a FENE spring force-extension law is defined as

$$h(Q)_{FENE} = \frac{3k_BT}{b_kL}\left(1 - \frac{Q^2}{L^2}\right)^{-1}, \tag{3.9}$$

where k_B is the Boltzmann constant, T the temperature, b_k is the Kuhn length of a polymer chain segment, Q is the end-to-end distance between crosslink junctions, and L denotes the contour length between junctions.

Given a functional form for the nonlinear elastic elements of the network $h(Q)$ and experimental measurements of G_0 and χ, one can estimate network features using Eqns. 3.5-3.8. We can estimate features assuming that the nonlinearity is either driven solely by finite-extensibility (n=0), or solely by a strain-induced increase in crosslink density ($\hbar$=0). Alternatively, we can allow $\hbar$ and n to be free parameters and estimate the relative contribution from each mechanism. Using this approach, we infer network features from the linear elastic shear modulus G_0. The procedure for extracting network features and calculating the relative contribution from each mechanism is summarized as follows. A more detailed derivation is shown in Appendix B.2.

Using Eqns. 3.5, 3.7 and 3.9, we calculate the FENE representation of the elastic shear modulus G_0 and the contribution from nonlinear elastic elements to the nonlinear response $\hbar$ as

$$G_{0,FENE} = \frac{n\left(Q_{eq}\right)k_BT}{b_K/L}\frac{Q_{eq}^2}{L^2}\left(1 - \frac{Q_{eq}^2}{L^2}\right)^{-1}, \tag{3.10}$$

$$\hbar_{FENE} = 2\frac{Q_{eq}^2}{L^2}\left(1 - \frac{Q_{eq}^2}{L^2}\right)^{-1}, \tag{3.11}$$

respectively. The linear elastic modulus G_0 depends on the ratio $\frac{Q_{eq}}{L}$ because this sets the equilibrium force-extension sensitivity. Similarly, $\hbar$ depends on the ratio because it depends on the end-to-end distance of the polymer chain compared to the contour length. We can therefore combine equations to eliminate the ratio to produce an equation for $\hbar$ as a function of G_0 (see Appendix B.2 for details). This calculation requires polymer specific information such as the characteristic ratio C_∞, and takes the functional form $\hbar(G_0; k_B T, C_\infty, l, \theta)$, where k_B, T and C_∞ have previously been defined, l is the length of the C-C bond of a polymer chain and θ is the bond (valence) angle [1]. Finally, comparing $\hbar$ to χ identifies the relative contribution from stretch-induced crosslinking $\varkappa = \chi - \hbar$.

Table 3.3: Summary of structure features derived by allowing both mechanisms to contribute to the nonlinear response. The end-to-end distance between crosslinks Q_{eq} are estimated to range from 10 to 35 nm, the ratio $\frac{Q_{eq}}{L}$ ranges from 0.045 to 0.15, and the FENE finite-extensibility contribution $\hbar_{FENE,rel} = \frac{\hbar}{\chi}$ ranges from 0.35% to 5%.

Composition (PVA wt% : Borax wt%)	Q_{eq} (nm)	$\frac{Q_{eq}}{L}$ (-)	$\hbar_{FENE,rel}$ (%)
2 : 0.5	34	0.046	0.36
2 : 1.25	27	0.058	0.82
2.75 : 0.05	30	0.053	0.76
2.75 : 0.1	21	0.077	1.4
2.75 : 0.5	17	0.094	1.5
2.75 : 1.25	15	0.11	2.3
2.75 : 1.5	15	0.11	2.6
3.5 : 0.05	20	0.079	2.5
3.5 : 0.1	16	0.10	3.5
3.5 : 0.5	11	0.14	3.4
3.5 : 1.25	10	0.15	4.6

Table 3.3 shows a summary for the network features inferred from the experimental measurements of G_0 and χ. It is important to note that the following observations regarding the structure of the PVA-Borax network are based on the underlying assumption for our analysis: the nonlinear elastic elements in the polymer network obey a FENE force-extension law, which leads to G_0 defining the ratio of the end-to-end distance between crosslinks Q_{eq} to the contour length between crosslinks L (see Eqn. 3.10). This assumption guarantees that there is a positive relationship between the modulus and the ratio (i.e., the ratio increases as the modulus increases) suggesting that Q_{eq} and L are more comparable in length as G_0 increases. Additionally, it is observed that Q_{eq} decreases with G_0 because a higher crosslink density underlies a higher elastic modulus. This is consistent with our assumed functional form $n(Q) \approx 1/Q_{eq}$

and with other polymer network models, such as the phantom network model [58]. The distance between crosslinks Q_{eq} is estimated to range from $10-35$ nm. This range is about $3-7$ times the reported correlation length (e.g. mesh size ξ) of PVA-Borax networks from dynamic light scattering (DLS) experiments, which were estimated to be on the order of $\xi \sim 3 - 5.5$ nm [44], [48], [49], [63]. It is natural that $Q_{eq} > \xi$ if there are entanglements that are not crosslinked, i.e. a topological constraint that appears in DLS but is not crosslinked with a borate ion. Thus, the crosslink density and Q_{eq} estimates from our analysis are reasonably consistent with measurements found in the literature.

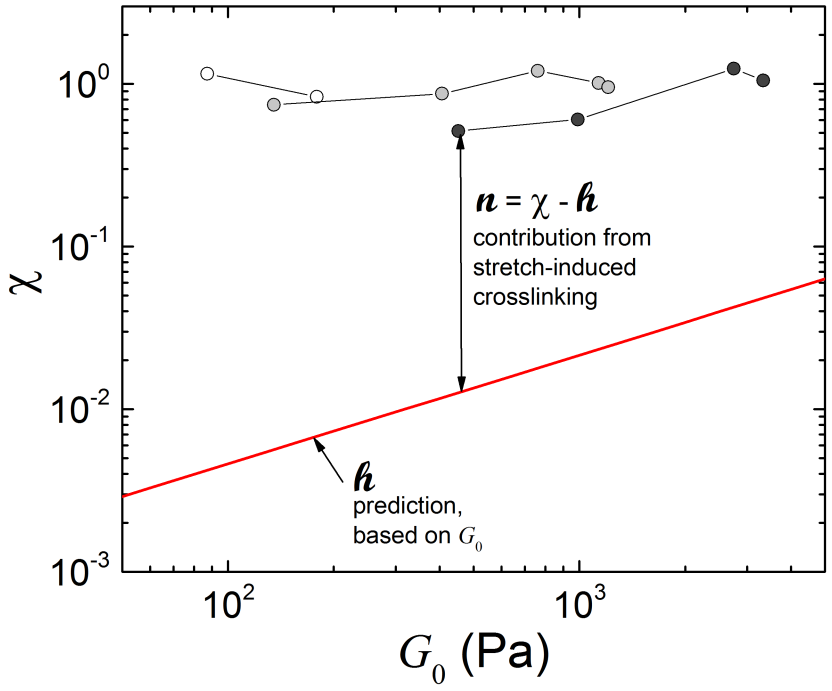

Figure 3.15: Nonlinear model parameter χ as a function of linear shear modulus G_0. Red line is the predicted FENE contribution for a given G_0. Results suggest that strain-induced network structuring is the more dominant mechanism driving the strain-stiffening response. Symbol colors represent different wt% of PVA: white (2 wt%), light grey (2.75 wt%), dark grey (3.5 wt%).

Figure 3.15 compares χ to the $\hbar$ prediction from G_0, clearly demonstrating that finite-extensibility is a sub-dominant ($< 5\%$) contribution to the inherent nonlinearity of PVA-Borax across these 11 compositions. While $\hbar$ increases monotonically with G_0, the experimentally measured nonlinear parameter χ does not, and in fact, is nearly constant as a function of G_0. Thus, it is observed that for this material system, as the

stiffness of the material G_0 increases, the relative contribution from network structuring decreases, as seen by rearranging Eqn. 3.6 as $\mathscr{n} = \chi - \mathscr{h}$. The key observation is that stretch-induced network structuring allows for a softer material to achieve the same nonlinear strength as one with a higher elastic modulus.

We interpret the network structuring value using the definition in Eqn. 3.8 which can be written as $n = \frac{dn/n}{dQ/Q}\Big|_{Q_{eq}}$. In words, this value represents the comparison between the fractional increase in the crosslink density to the distance between crosslinks. For example, for the nonlinear response of 2 wt% PVA with 0.5 wt% Borax, the relative contribution from stretch-induced network structuring is $\mathscr{n} = \chi - \mathscr{h} = 1.157 - 0.004 = 1.153$. This means that a 1% increase in the distance between crosslinks dQ/Q would cause a 1.153% increase in the crosslink density. The range in $\mathscr{n}$ is from 0.5-1.2 for the PVA-Borax systems tested. This is qualitatively consistent with observed trends of stretch-induced network structuring [27]. In summary, the results shown in Fig. 3.15 strongly indicate that the dominant mechanism driving the nonlinear response is stretch-induced network structuring. This explains the full frequency-dependent third-harmonic MAOS signatures, which collapse $G'(\omega)$, $\eta'(\omega)$, $[e_3]\,(\omega)$, and $[v_3]\,(\omega)$ using only three degrees of freedom: G_0, η_0, and χ.

Chapter 4

First-Harmonic MAOS Can Predict Unseen Third-Harmonic MAOS

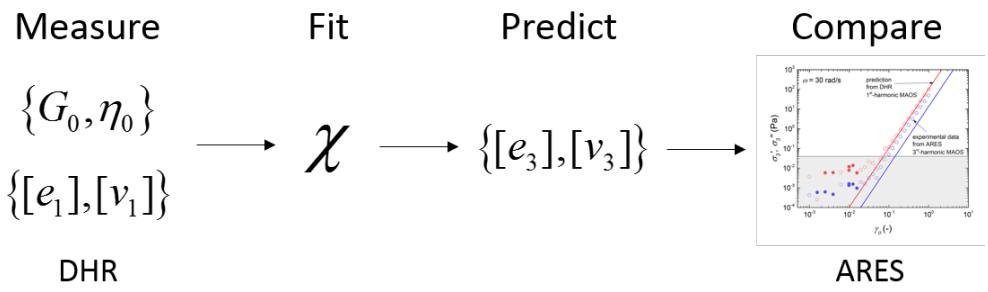

Figure 4.1: Graphical Abstract. Linear and asymptotically nonlinear parameters were measured to fit/calibrate model parameters. The model parameters are used to predict third-harmonic MAOS measurements. We compare the prediction to the experimentally measured third-harmonic MAOS measures.

Our discussion focuses on how first-harmonic MAOS measures can predict third-harmonic MAOS, demonstrating the credibility of a structure-rheology model for PVA-Borax. Figure 4.1 shows a graphical summary of the protocol discussed in this chapter. First-harmonic MAOS measures from a stress-controlled rotational rheometer (DHR-3, TA Instruments) are used to calibrate model parameters and make predictions of the full MAOS signatures measured on a strain-controlled rotational rheometer (ARES-G2, TA Instruments; data from Chapter 3). It is important to explicitly make a distinction between instruments because we have more confidence in MAOS measurements from a strain-controlled rheometer where torque is measured from a fixed boundary [64]. The successful prediction provides evidence of the power of first-harmonic MAOS and

of model validity of this specific structure-rheology model as it is tested across 11 different compositions of PVA-Borax.

4.1 Linear Viscoelastic Results

Rheological measurements of first-harmonic MAOS measures $[e_1]$ and $[v_1]$ were performed on a stress-controlled combined motor-transducer rotational rheometer (DHR-3, TA Instruments) following the protocol discussed in Section 2.2.2. To identify the linear viscoelastic (SAOS) regime, strain-sweeps were performed at 10 rad/s starting from $\gamma_0 = 0.01\%$ until deviations from a linear behavior were observed. We performed a forward and reverse sweep to check for reversibility. A strain amplitude γ_0 was chosen from the linear viscoelastic regime for the SAOS frequency-sweep carried out from $\omega = 0.1$ to $\omega = 100$ rad/s. We followed the protocol discussed in Section 3.1 for extracting the linear parameters G_0, η_0, and $\lambda_0 = \frac{\eta_0}{G_0}$. In summary, we fit high and low frequency plateaus to extract the storage modulus G_0 and steady shear viscosity η_0, respectively. We then calculate the relaxation timescale $\lambda_0 = \frac{\eta_0}{G_0}$. We follow this protocol for each composition. Table 4.1 shows the set of linear parameters $\{G_0, \eta_0, \lambda_0\}$ for each composition.

Table 4.1: Summary of the linear parameters $\{G_0, \eta_0, \lambda_0\}$ measured on the stress-controlled rheometer (DHR-3).

Label	Composition (PVA wt% : Borax wt%)	G_0 (Pa)	η_0 (Pa.s)	λ_0 (s)
A1	2 : 0.5	94.64	20.78	0.220
A2	2 : 1.25	194.46	42.44	0.218
B1	2.75 : 0.05	148.17	18.99	0.128
B2	2.75 : 0.1	446.66	133.70	0.299
B3	2.75 : 0.5	1013.61	495.97	0.489
B4	2.75 : 1.25	1222.20	511.90	0.419
B5	2.75 : 1.5	1129.29	435.55	0.386
C1	3.5 : 0.05	342.49	50.54	0.148
C2	3.5 : 0.1	999.40	348.40	0.349
C3	3.5 : 0.5	2551.81	1876.68	0.735
C4	3.5 : 1.25	3391.11	2158.69	0.637

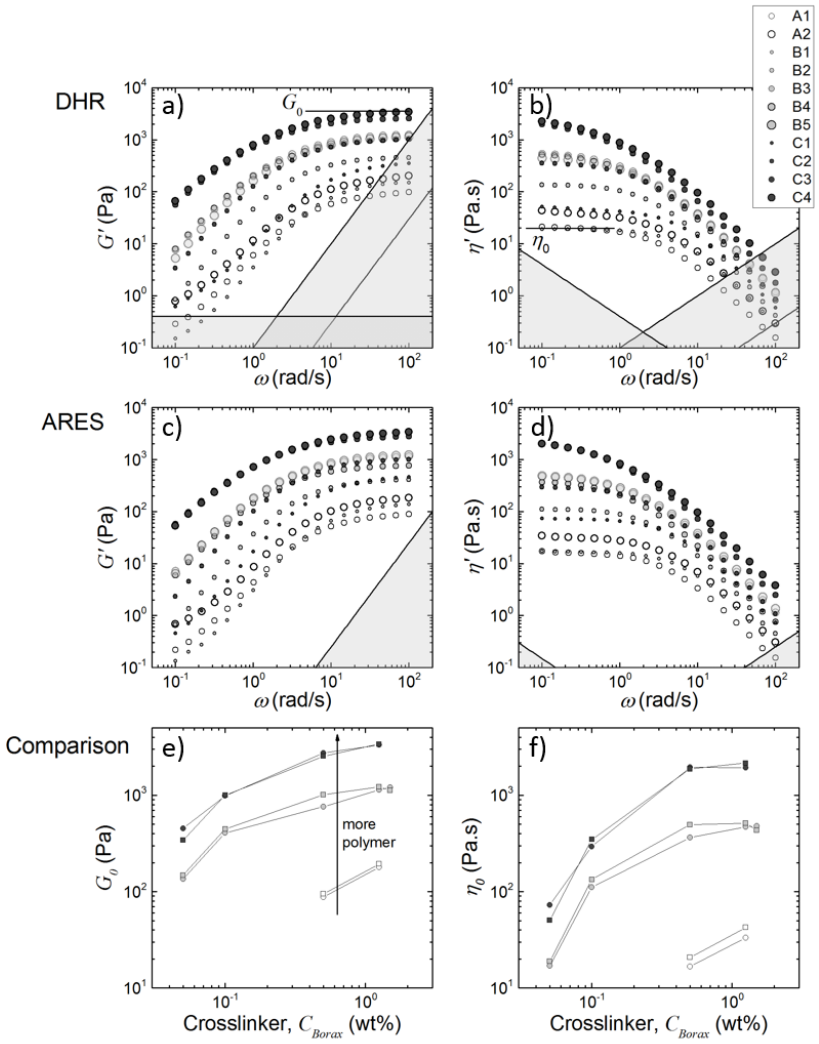

Figure 4.2: SAOS frequency-sweep on multiple compositions of PVA-Borax shown in (a)-(d). DHR data is shown in (a) and (b), while ARES data is shown in (c) and (d). The legend shown near (b) is valid for (a)-(d). The linear parameters G_0 and η_0 are compared in (e) and (f), where the squares represent DHR data and circles represent ARES data. The torque limit is shown as a constant line, while the material inertia and instrument inertial limits are shown as lines with scaling $\sim \omega^2$ [41].

We compare the linear viscoelastic data from the stress-controlled rheometer (DHR) to those from a strain-controlled rheomoeter (ARES) to establish a baseline expectation for agreement between different instruments and different samples. Qualitatively, the data appear to be consistent across the frequency spectrum, as seen in Figs. 4.2(a)-(d). The linear parameters $\{G_0, \eta_0, \lambda_0\}$ are compared in Figs. 4.2(e)-(f)

and Fig. 4.3. As expected, the linear parameters qualitatively agree and exhibit the same trends as a function of crosslinker. The linear parameters are expected to agree between instruments since the measurements are made in the linear regime.

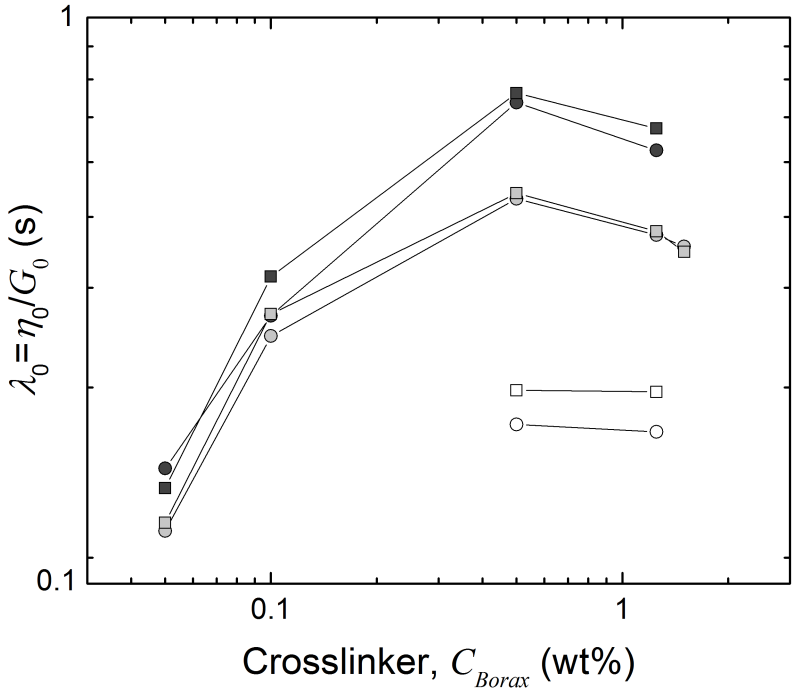

Figure 4.3: Comparison between the linear relaxation timescales $\lambda_0 = \frac{\eta_0}{G_0}$ measured from the DHR and ARES from multiple compositions of PVA-Borax. Squares denote DHR data, while circles represent ARES data.

In Table 4.2, we quantify the agreement between instruments using the relative difference between measurements of the linear parameters as a metric. The differences are calculated as

$$\delta_X = \frac{X_{ARES} - X_{DHR}}{X_{ARES}}, \tag{4.1}$$

where X represents any measured parameter and the subscripts represent which instrument the data were collected on. We observe that the relative difference between measured values of G_0 ranged from approximately 1-30% across all compositions of PVA-Borax. It is worth noting that measurements of G_0 for

Table 4.2: Summary of the relative difference between measurements of the linear parameters $\{G_0, \eta_0, \lambda_0\}$ from the strain-controlled rheometer (ARES-G2) to those from the stress-controlled rheometer (DHR-3). The differences are calculated using Eqn. 4.1, where $X = \{G_0, \eta_0, \lambda_0\}$ represents the set of linear parameters.

Composition (PVA wt% : Borax wt%)	δ_{G_0} (%)	δ_{η_0} (%)	δ_{λ_0} (%)
2 : 0.5	-8.29	-24.23	-14.91
2 : 1.25	-8.65	-27.90	-17.72
2.75 : 0.05 -	9.55	-12.18	-3.38
2.75 : 0.1	-9.76	-20.25	-9.33
2.75 : 0.5	-33.22	-36.19	-2.24
2.75 : 1.25	-7.65	-9.12	-1.40
2.75 : 1.5	6.59	9.08	2.08
3.5 : 0.05	24.35	30.51	7.63
3.5 : 0.1	-1.04	-18.36	-17.20
3.5 : 0.5	-7.26	-3.68	-3.92
3.5 : 1.25	-1.65	-11.14	-9.36

most compositions had a relative difference less than 10% (with just two exceptions). Similarly, the relative difference between measured values of λ_0 were observed to fall between a relatively small window of approximately 1-15%, in which only three compositions had a relative difference greater than 10%. The relative difference between measured values of η_0 were greater than those of G_0 and λ_0 for almost all compositions (approximately 5-30%, only three compositions less than 10%). On average, measurements of $\{G_0, \eta_0, \lambda_0\}$ differed by $\{10.7, 18.4, 8.1\}\%$ across all compositions, i.e. on average having larger values on the DHR instrument (negative values in Table 4.2).

It is important to note that there appears to be a systematic error between the two instruments since most measurements of $\{G_0, \eta_0, \lambda_0\}$ on the DHR are larger than those measured on the ARES instrument. The disagreement between instruments could come from using different batches of formulated PVA-Borax compositions used for testing on each instrument. Another possible source of error is from instrument calibration, since the disagreement tends to be systematic. Nevertheless, measurements of the linear parameters are reasonably consistent between instruments, as expected. Based on our quantitative observations, it is reasonable to assume that the instruments agree to within 15%. We use this as a baseline expectation for agreement between different instruments and different samples.

4.2 Asymptotically Nonlinear Viscoelastic Results

To identify the asymptotically nonlinear (MAOS) regime, we analyze the strain-sweeps performed at $\omega = 10$ rad/s on the DHR discussed in the previous section. The frequency of $\omega = 10$ rad/s was chosen to probe the material in the elastic limit, where $De > 1$ (note $\lambda_{0,min} = 0.128$ s, Table 4.1). At $\omega = 10$ rad/s, the range of Deborah numbers for all compositions of PVA-Borax were between $De = \lambda_0\omega \approx 1.5 - 7$, in which it is reasonable to assume that the material behaves more elastically. We could not choose a higher frequency for some compositions because the measurements would be affected by instrument inertia (see Fig. 4.2). It should be noted that instrument inertia is an artifact of a combined motor-transducer (DHR). Figure 4.4 shows the strain-sweeps at 10 rad/s for all compositions tested on the DHR. The MAOS regime is identified by the stress-harmonic nonlinearity exhibiting a scaling $\sim \gamma_0^3$ (Eqns. 1.5-1.8).

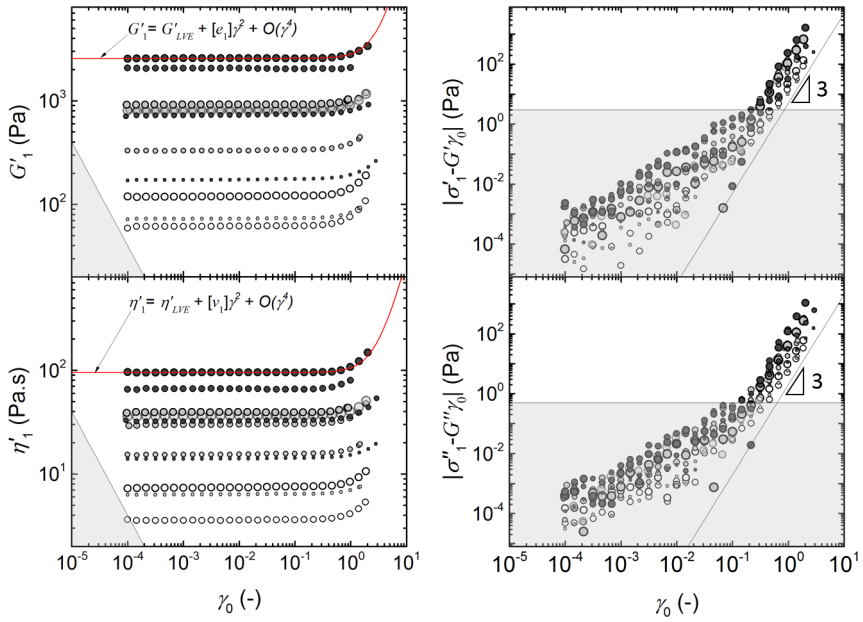

Figure 4.4: First-harmonic MAOS signatures from strain-sweeps at 10 rad/s on multiple compositions of PVA-Borax performed on DHR. Fit lines from Eqns. 1.9 and 1.10, where $\eta' = \frac{G''}{\omega}$. Symbols same as in Fig. 4.2. Noise floor shown in grey. Right panel is transformed stress response data, in which the MAOS regime is identified by a power-law scaling $\sim \gamma_0^3$.

We use the conventional strain-sweep method for MAOS material parameter extraction outlined in Section 2.2.2.1. We fit for the linear viscoelastic plateaus, G'_{LVE} and η'_{LVE}, and the first-harmonic MAOS

Table 4.3: Summary of asymptotically nonlinear parameters measured on the stress-controlled rheometer (DHR-3). First-harmonic measures $[e_1]$ and $[v_1]$ are used to calculate an estimate of model parameters χ_e and χ_v, respectively. The average $\bar{\chi} = \frac{\chi_e + \chi_v}{2}$ is used as a calibration model parameter to predict third-harmonic MAOS measures.

Composition (PVA wt% : Borax wt%)	$[e_1]$ (Pa)	$[v_1]$ (Pa.s)	χ_e (-)	χ_v (-)	$\bar{\chi}$ (-)
2 : 0.5	18.66	0.66	1.34	1.17	1.25
2 : 1.25	26.53	1.39	0.93	1.20	1.06
2.75 : 0.05	12.85	0.81	1.00	0.93	0.96
2.75 : 0.1	72.14	2.63	0.94	1.15	1.05
2.75 : 0.5	172.11	5.99	0.88	1.67	1.27
2.75 : 1.25	126.81	5.29	0.55	1.07	0.81
2.75 : 1.5	119.54	4.37	0.57	0.90	0.74
3.5 : 0.05	26.76	1.31	0.75	0.62	0.68
3.5 : 0.1	83.70	3.51	0.47	0.76	0.61
3.5 : 0.5	16.73	10.47	0.03	1.67	0.85
3.5 : 1.25	258.65	10.44	0.38	1.10	0.74

measures $[e_1]$ and $[v_1]$ at 10 rad/s using Eqns. 1.9 and 1.10, seen in Fig. 4.4. It is important to note that there is subjectivity in the process of fitting for material parameters, especially those pertaining to the MAOS regime. There is subjectivity when choosing how many data points to fit since we only want to fit asymptotic changes to the linear baseline. We chose data points up to a 10% change from the linear baseline for our analysis. We followed this procedure for each composition of PVA-Borax tested, and the values for $[e_1]$ and $[v_1]$ are shown in the second and third columns in Table 4.3. We discuss the last three columns in Table 4.3 in the following section, in which the linear parameters and first-harmonic MAOS measures from a stress-controlled rheometer (Tables 4.1 and 4.3, respectively) were used to calibrate model parameters and then make predictions of third-harmonic MAOS from a strain-controlled rheometer.

4.3 Structure-Rheology Model and Predictions

We use the transient polymer network model of Bharadwaj et al. discussed in Sections 1.1 and 3.3, where the key ingredient for describing a nonlinear response is a single nonlinear parameter, χ [1]. The first-harmonic MAOS measures are related to χ by Eqns. 51 and 53 in [1],

$$\frac{[e_1]}{G_0} = \frac{5}{6}\chi \left(\frac{De^4 \left(De^2 + \frac{2}{5}\right)}{\left(1 + De^2\right)^2 \left(1 + 4De^2\right)} \right), \tag{4.2}$$

$$\frac{[v_1]}{\eta_0} = \frac{3}{4}\chi\left(\frac{De^2\left(De^2+\frac{1}{3}\right)}{\left(1+De^2\right)^2\left(1+4De^2\right)}\right). \tag{4.3}$$

In principle, χ could be fit to the full MAOS description which is defined by the four frequency-dependent first- and third-harmonic MAOS measures $\{[e_1](\omega), [v_1](\omega), [e_3](\omega), [v_3](\omega)\}$ defined in Eqns. 1.9-1.12. Here, we use measurements of the first-harmonic MAOS measures at a single frequency ($\omega = 10$ rad/s) to calibrate χ. Solving for χ in Eqns. 4.2 and 4.3 yields an estimate of the model parameter from either the elastic or viscous response, which we denote respectively as χ_e and χ_v,

$$\chi_e = \frac{6}{5}\frac{[e_1]}{G_0}\left(\frac{\left(1+De^2\right)^2\left(1+4De^2\right)}{De^4\left(De^2+\frac{2}{5}\right)}\right) \tag{4.4}$$

and

$$\chi_v = \frac{4}{3}\frac{[v_1]}{\eta_0}\left(\frac{\left(1+De^2\right)^2\left(1+4De^2\right)}{De^2\left(De^2+\frac{1}{3}\right)}\right), \tag{4.5}$$

respectively. These calculations require calibration of model parameters G_0, η_0 and λ_0 ($De = \lambda_0\omega$), which we take from Table 4.1. We use the average of χ_e and χ_v

$$\bar{\chi} = \frac{\chi_e + \chi_v}{2} \tag{4.6}$$

as an estimate of χ for each PVA-Borax composition tested on the DHR. Table 4.3 shows the values for $\{\chi_e, \chi_v, \bar{\chi}\}$ for each composition and Fig. 4.5 shows $\bar{\chi}$ as a function of crosslinker. Moreover, $\bar{\chi}$ serves as a calibration parameter used to predict the frequency-dependent third-harmonic MAOS measures.

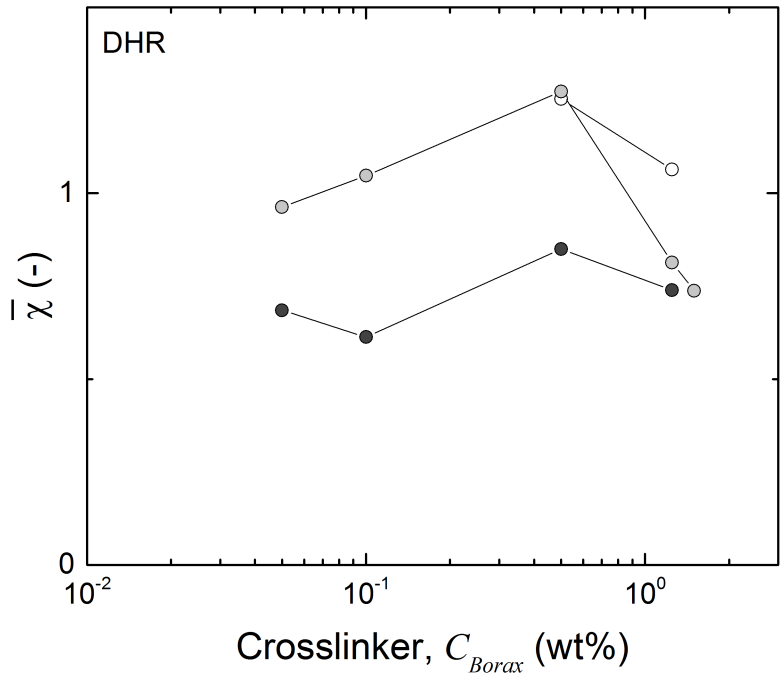

Figure 4.5: The parameter $\bar{\chi}$ (Eqn. 4.6), calibrated to first-harmonic MAOS parameters $[e_1]$ and $[v_1]$ from the DHR for each PVA-Borax composition tested. Polymer concentration increases with symbol color from white to gray to black.

The third-harmonic MAOS measures are related to χ by Eqns. 52 and 54 in [1],

$$\frac{[e_3]}{G_0} = \frac{1}{6}\chi\left(\frac{De^4\left(De^2-2\right)}{\left(1+De^2\right)^2\left(1+4De^2\right)}\right), \tag{4.7}$$

$$\frac{[v_3]}{\eta_0} = -\frac{5}{12}\chi\left(\frac{De^2\left(De^2-\frac{1}{5}\right)}{\left(1+De^2\right)^2\left(1+4De^2\right)}\right). \tag{4.8}$$

Thus, we can predict third-harmonic MAOS measures at any frequency by solving for $[e_3]$ and $[v_3]$ in Eqns. 4.7 and 4.8 using the linear parameters $\left\{G_0, \eta_0, \lambda_0 = \frac{\eta_0}{G_0}\right\}$ (Table 4.1) and the calibrated nonlinear model parameter $\bar{\chi}$ (Table 4.3), where $\chi \to \bar{\chi}$ in Eqns. 4.7 and 4.8. Furthermore, we can predict the third-harmonic stress response at any frequency using Eqns. 1.7 and 1.8. Figure 4.6 is a graphical representation for the process of predicting third-harmonic MAOS from first-harmonic MAOS for 3.5 wt% PVA with 1.25 wt% Borax. In summary, we fit $[e_1]$ and $[v_1]$ to strain-sweep data at 10 rad/s from measurements performed on the DHR-3, calibrate the model parameter $\bar{\chi}$ and predict third-harmonic MAOS measures $[e_3]$

and $[v_3]$ at 30 rad/s, and compare this to measurements on an ARES-G2 rheometer. Third-harmonic data and predictions for all compositions are shown in Figs. 4.7-4.9.

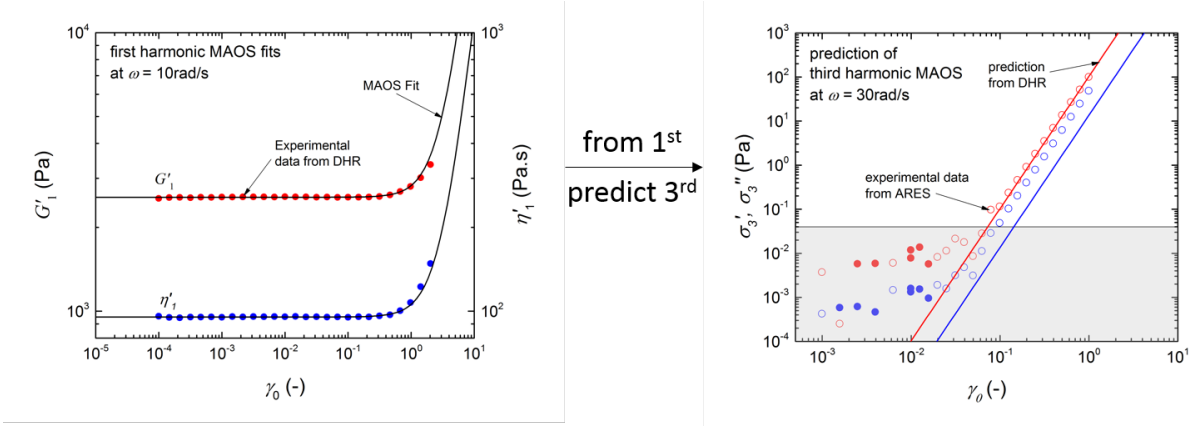

Figure 4.6: Summary of process for predicting third-harmonic MAOS from first-harmonic MAOS for 3.5 wt% PVA with 1.25 wt% Borax. Amplitude sweep data at 10 rad/s (left) is used to obtain first-harmonic MAOS measures $[e_1]$ and $[v_1]$ to predict third-harmonic MAOS measures $[e_3]$ and $[v_3]$ at 30 rad/s, based on the nonlinear transient network model for PVA-Borax from Bharadwaj et al. [1].

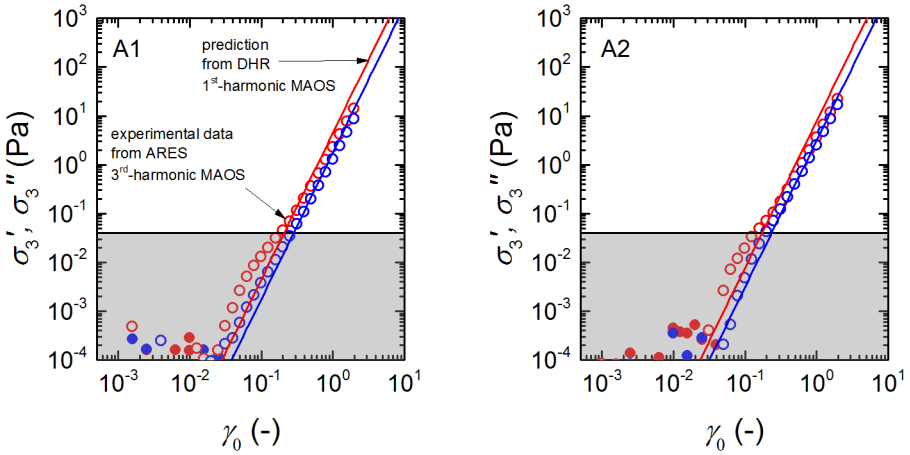

Figure 4.7: Prediction of third harmonic MAOS measures for each composition of $C_{PVA} =$ 2 wt% and $C_{Borax} = \{0.5, 1.25\}$ wt%. The labels in each graph represent the composition labeled in Table 4.1.

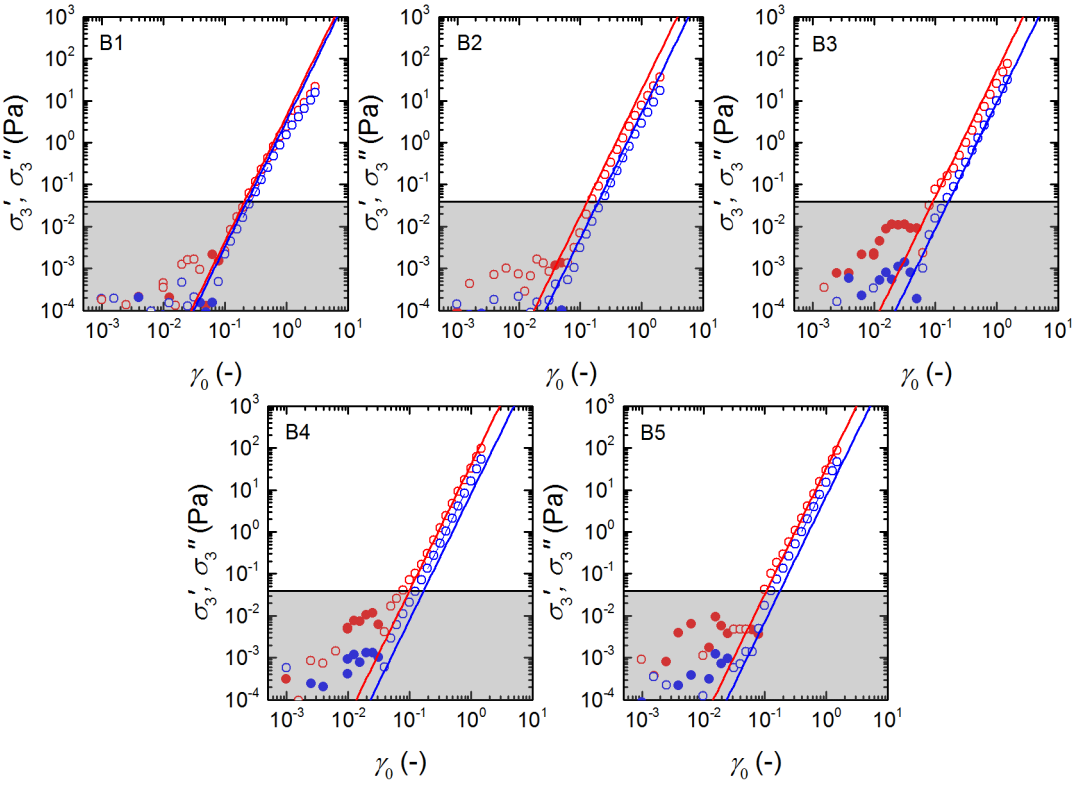

Figure 4.8: Prediction of third harmonic MAOS measures for each composition of $C_{PVA} = 2.75$ wt% and $C_{Borax} = \{0.05, 0.1, 0.5, 1.25, 1.5\}$ wt%. The labels in each graph represent the composition labeled in Table 4.1.

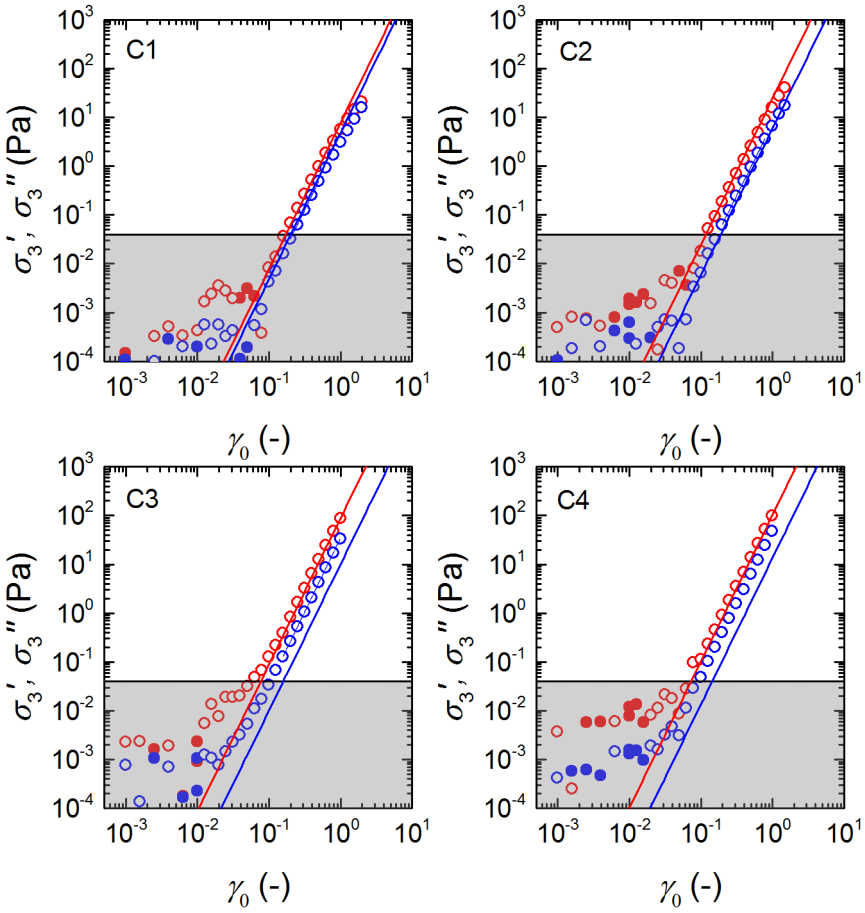

Figure 4.9: Prediction of third harmonic MAOS measures for each composition of $C_{PVA} = 3.5$ wt% and $C_{Borax} = \{0.05, 0.1, 0.5, 1.25\}$ wt%. The labels in each graph represent the composition labeled in Table 4.1.

As seen in Figs. 4.7-4.9, the agreement between prediction and experimental observation is remarkable, indicating an ability of first-harmonic MAOS to predict otherwise unseen third-harmonic MAOS, even at a frequency three times larger, when a valid constitutive model is available. Table 4.4 shows a summary of the observed (ARES) and predicted (DHR) values of $[e_3]$ and $[v_3]$, as well as their relative differences,

$$\delta_X = \frac{X_{obs} - X_{pred}}{X_{obs}}, \tag{4.9}$$

for each composition of PVA-Borax tested. We use the relative difference as a metric for model prediction accuracy. We observe that the relative difference between values of the third-harmonic elastic parameter $[e_3]$

Table 4.4: Summary of observed and predicted values of $[e_3]$ and $[v_3]$ and their prediction accuracy. Metric is relative difference between fit to third-harmonic data and the prediction value. The differences are calculated using Eqn. 4.9, where $X = \{[e_3], [v_3]\}$.

Composition (PVA wt% : Borax wt%)	$[e_3]_{obs}$ (Pa)	$[e_3]_{pred}$ (Pa)	$[v_3]_{obs}$ (Pa.s)	$[v_3]_{pred}$ (Pa.s)	$\delta_{[e_3]}$ (%)	$\delta_{[v_3]}$ (%)
2 : 0.5	2.74	4.48	0.047	0.059	-63.33	-24.58
2 : 1.25	4.27	7.80	0.083	0.104	-82.65	-24.67
2.75 : 0.05	3.73	4.44	0.120	0.110	-18.91	8.47
2.75 : 0.1	11.21	18.48	0.113	0.175	-64.84	-55.87
2.75 : 0.5	31.47	52.74	0.345	0.302	-67.57	12.56
2.75 : 1.25	37.17	40.32	0.558	0.270	-8.48	51.55
2.75 : 1.5	33.85	33.63	0.529	0.246	0.69	53.61
3.5 : 0.05	8.85	7.85	0.133	0.163	11.39	-22.31
3.5 : 0.1	23.48	24.54	0.264	0.199	-4.50	24.65
3.5 : 0.5	102.75	89.53	1.153	0.339	12.87	70.57
3.5 : 1.25	112.42	103.21	1.707	0.453	8.19	73.49

ranged from approximately 0.5-80% across all compositions of PVA-Borax. Similarly, the relative difference between measured values of the third-harmonic viscous parameter $[v_3]$ were observed to fall between approximately 10-75%. On average, the median magnitude of the relative difference between observed and predicted values of $\{[e_3], [v_3]\}$ is 13% and 25%, respectively, across all compositions. Although some compositions have larger disagreement, our general observations agree to within a similar accuracy of the linear viscoelastic parameters tested on different instruments with different batches of sample, as discussed in Section 4.1.

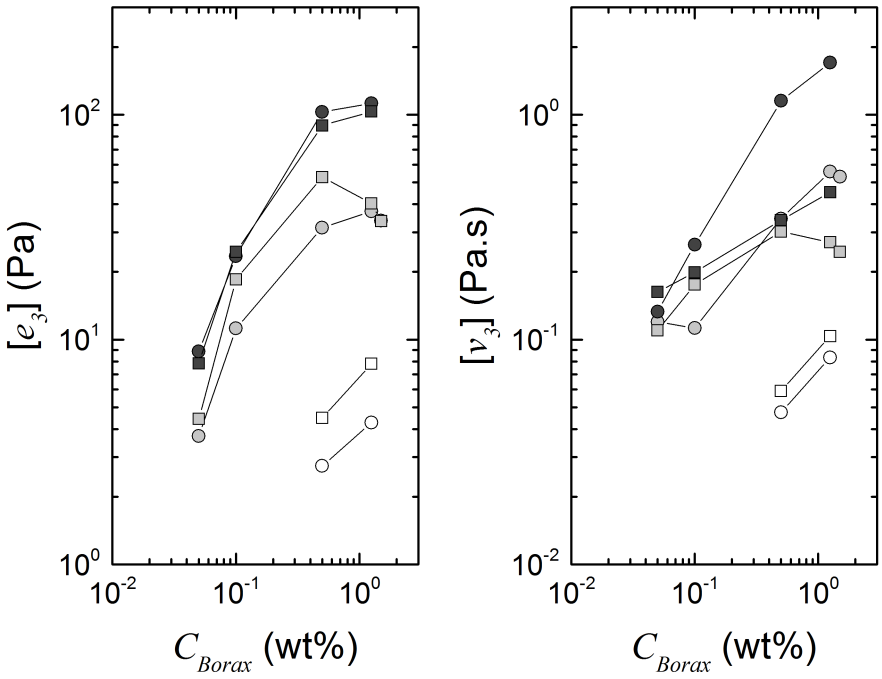

Figure 4.10: Comparison between the observed third-harmonic MAOS parameters from the ARES (circles) and the predicted values (squares) from first-harmonic MAOS measurements from the DHR.

Figure 4.10 shows a comparison between the observed third-harmonic MAOS parameters (ARES) and the predicted values from first-harmonic MAOS measurements (DHR) using the transient polymer network model of Bharadwaj et al. [1]. The model is better at predicting $[e_3]$ than $[v_3]$; thus, it can be improved (e.g. with a more complex viscoelastic spectrum rather than a single mode). The disagreement suggests specifically where the model is failing. Nevertheless, first-harmonic nonlinearities are able to predict "unseen" third-harmonic MAOS harmonic data to within a similar accuracy of the linear viscoelastic parameters for most of the compositions tested. Furthermore, first-harmonic MAOS were able to correctly predict the signs of all third-harmonic MAOS measures. Thus, the transient polymer network is considered a good model for predicting the nonlinear behavior of a PVA-Borax polymer network across the wide range of compositions tested here (with range of $G_0 = 100 - 3000$ Pa). In conclusion, the successful predictions are evidence of model validation, and a testament to the value of first-harmonic MAOS, which has often been overlooked in the recent experimental MAOS literature.

Chapter 5

Ashby Style Perspective

Nonlinear elasticity for a purely elastic solid is described as the first order deviation from the linear response, as discussed in Chapter 1. The stress response for such a system is shown in Fig. 1.1 and defined in Eqn. 1.2. Here, we define the dimensionless parameter b in Eqn. 1.2 as the universal nonlinear elastic parameter representing the intrinsic nonlinearity of a material system subject to a shear strain. A stiffening response corresponds to $b > 0$ and $b < 0$ represents a softening response. While the intrinsic nonlinearity is well defined for a purely elastic solid, it is more complicated to define nonlinear parameters for viscoelastic materials because of their rich time-dependence. The universal elastic parameter, b, is useful because it can be related to stiffening parameters defined in theoretical models, and we can define b for any test measuring stress as a function of strain for any elastic material.

For a purely elastic material, a quasi-static test in which a strain is applied is often the experimental technique used to measure an elastic modulus. The apparent modulus is defined as

$$G(\gamma) = G_0 + \beta\gamma^2 + \cdots . \tag{5.1}$$

Substituting the apparent modulus $G(\gamma)$ in Eqn. 5.1 for that in Eqn. 1.2 and then comparing the result to the original equation yields the following relationship,

$$b = \frac{\beta}{G_0}. \tag{5.2}$$

Thus, for any quasi-static stress-strain test, we can fit the nonlinear parameter β in Eqn. 5.1 and calculate a value for the intrinsic nonlinearity, b.

For a viscoelastic material, the elastic modulus is often frequency-dependent. For this reason, the modulus is often measured by an oscillation test at a fixed frequency. For this testing protocol, the elastic modulus is derived from the first-harmonic elastic stress coefficient in the Chebyshev interpretation [24], [38] and is defined in Eqn. 1.9. We can relate b to the first-harmonic intrinsic elastic nonlinearity $[e_1]$; however the relationship is non-trivial due to the stress response in Eqn. 1.2 being decomposed into integer harmonics. It can be shown that the nonlinearity is distributed between the first and third elastic stress-harmonics [65]. We derive the relation between b and $[e_1]$ in Appendix C.1 and yield the following result,

$$b = \frac{4}{3}\frac{[e_1]}{G_{LVE}}. \tag{5.3}$$

The parameter b can also be related to theoretical models describing an elastic material. To relate b to model parameters, we define the governing equation for an elastic material as

$$\sigma_{e,ij} = 2\left[\left(\frac{\partial U}{\partial I_1} + I_1\frac{\partial U}{\partial I_2}\right)B_{ij} - \frac{\partial U}{\partial I_2}B_{ik}\cdot B_{kj}\right], \tag{5.4}$$

where U is the elastic potential, I_1 and I_2 are the first and second invariants of the finger tensor, $\underline{\underline{\boldsymbol{B}}}$ [39]. The finger tensor in simple shear defined as

$$\underline{\underline{\boldsymbol{B}}} = \begin{bmatrix} 1+\gamma^2 & \gamma & 0 \\ \gamma & 1 & 0 \\ 0 & 0 & 1 \end{bmatrix} \tag{5.5}$$

where γ represents the shear strain [39]. Thus, given the elastic potential U for any model describing an elastic material, we can relate b to the model parameters by comparing an asymptotic expansion of the elastic stress in Eqn. 5.4 to the stress defined in Eqn. 1.2. Here, we are concerned with nonlinear responses subjected to a shear deformation, as seen by the definition of the finger tensor in Eqn. 5.5.

The neo-Hookean model can be used for predicting the nonlinear stress-strain behavior of a purely elastic material [39], [66]. The elastic potential is defined as

$$U = \frac{G_0}{2}\left(I_1 - 3\right). \tag{5.6}$$

The stress is computed using the elastic potential and the finger tensor defined in Eqn. 5.5, giving

$$\sigma_{e,xy} = G_0\gamma, \tag{5.7}$$

where $\sigma_{e,xy}$ represents the shear stress components of the stress tensor. Comparing Eqn. 5.7 to Eqn. 1.2 yields the following result,

$$b = 0. \tag{5.8}$$

It is apparent that the neo-Hookean model shows a linear dependence in response to a shear deformation and does not predict nonlinear behavior. However, it can be shown that the neo-Hookean model does predict nonlinear behavior in response to a uniaxial extension. Since we are concerned with shear nonlinearities, the neo-Hookean model is an insufficient description of nonlinear elasticity.

The Fung model is a constitutive equation developed to describe the behavior of elastic soft tissues [7]. The elastic potential is defined as

$$U = \frac{G_0}{2\alpha}e^{\alpha(I_1-3)}, \tag{5.9}$$

and the shear stress is calculated as

$$\sigma_{e,xy} = G_0\gamma e^{\alpha\gamma^2}. \tag{5.10}$$

To relate b to the Fung model nonlinear parameter α, we use a Taylor Expansion about $\gamma = 0$ (small shear deformations); hence,

$$\sigma_{e,xy} = G_0\gamma\left(1 + \alpha\gamma^2\right). \tag{5.11}$$

It is clear that

$$b = \alpha \tag{5.12}$$

when comparing Eqn. 5.11 to Eqn. 1.2. Thus, the Fung model does predict a nonlinear response with a shear deformation input. It can be shown that the model also predicts nonlinear behavior in response to a uniaxial extension. The Fung model is useful for fitting uniaxial extensional data and then converting the nonlinear parameter to a shear nonlinearity using Eqn. 5.12. The Taylor Expansion derivation is shown in Appendix C.2.

Here, we have shown that the dimensionless parameter b can be related to various testing protocols and model parameters. In the following section we compare the shear nonlinearities, b, of various materials using these relations.

5.1 Comparing Materials

We compare elastic nonlinearities, b, across material systems with distinct microstructures using the relations previously discussed. We digitized stress-strain data from the literature for various materials broadly categorized into three categories: biological tissues, biopolymers, and hydrogels (see Table 5.1). For data collected using a quasi-static shear test we fit for β in Eqn. 5.1 and calculated b using Eqn. 5.2. If the data were collected using an oscillation protocol we fit for $[e_1]$ in Eqn. 1.9 and use the relation in Eqn. 5.3 to calculate b. Finally, if the testing protocol was one for quasi-static extension, we fit for α in Eqn. 5.9 and convert the extensional nonlinearity to a shear nonlinearity using Eqn. 5.12. Ashby diagrams are used in design and material selection to compare various low-dimensional material parameters for different materials [67]. Using this framework, we compare the elastic shear nonlinearity b to the linear elastic modulus G for various materials in Fig. 5.1.

Table 5.1: Table of various materials found in the literature that exhibit nonlinear elasticity when subjected to large strains.

Material	G (Pa)	b (-)	Ref	Comments
Achilles Tendon	3.1×10^{11}	-	Levental et al. [68]	See reference
Articular Cartilage	9.5×10^{5}			
Skeletal Muscle	1.0×10^{5}			
Carotid Artery	9.0×10^{4}			
Thyroid Cancer	4.5×10^{4}			
Cardiac Muscle	1.5×10^{5}			
Skeletal Muscle	1.2×10^{4}			
Thyroid	9000			
Breast Tumor	4000			
Kidney	2500			
Premalignant Breast	2200			
Fibrotic Liver	1600			
Lymph w/ Metastasis	330			
Lymph Node	120			
Mammary Gland	160			
Fat	17			
Actin	94.71	96.91	Storm et al. [8]	Oscillation shear
Fibrin	19.15	9.64		
Collagen	13.22	179.30		
Vimentin	3.66	11.69		
Polyacrylamide	180	0.03		
Fibrin (1.6T)	4.99	21.87	Bharadwaj [69]	Oscillation shear
Fibrin (6.4T)	540.77	24.19		
Polyacrylamide (M/C=100)	900	0.09	Zhang et. al [22]	Quasi-Static shear
Polyacrylamide (M/C=300)	300	0.13		

Table 5.1: Continued from previous page

Material	G (Pa)	b (-)	Ref	Comments
Agarose (2.5A)	104534.30	0.85	Barrangou et al. [19]	Quasi-Static shear
Agarose (2A)	64719.90	2.14		
Agarose (1.5A)	31760.90	1.72		
Agarose + Glycerol (1.5A/40G)	46713.10	1.95		
Agarose + Glycerol (1A/60G)	25152.80	1.34		
Agar (1.93 dry wt%)	37466.15	45.56	Pavan et al. [20]	Quasi-Static shear
Gelatin (7.3%)	28858	1.78		
Agar (2.81%) + Gelatin (3%)	115189.50	23.66		
Agar (1.71%) + Gelatin (3%)	41963.01	27.21		
Agar (0.58%) + Gelatin (3%)	5067.10	21.04		
Ballistic Gel	3580500	8.506	Salisbury et al. [21]	Quasi-Static extension
Lung Tissue	4077.923	24.03	Yuan et al. [11]	Quasi-Static extension
	2625.35	15.94		
Brain Tissue	581.42	-11.42	Bilston et al. [12]	Quasi-Static shear
Cell Monolayer	910.79	-1244.54	Fernandez et al. [13]	Oscillation shear
Liver Tissue	212.86	-0.59	Tan et al. [14]	Oscillation shear
Spinal Chord	157730	2761.48	Cheng et al. [9]	Quasi-Static extension
Arterial Wall	18313.91	1.39	Hayashi et al. [10]	Quasi-Static extension

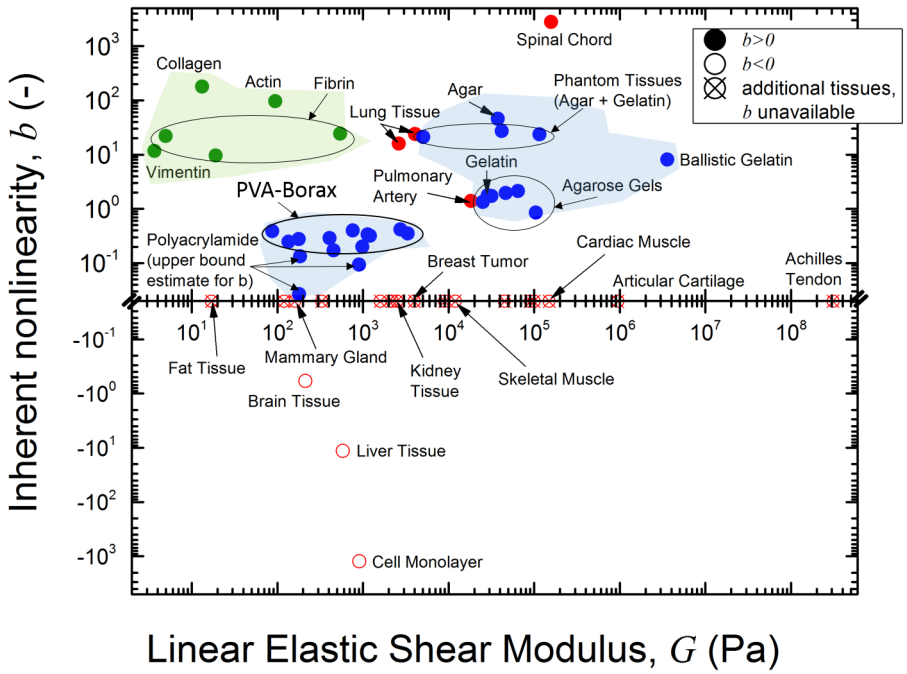

Figure 5.1: Ashby diagram showing the elastic nonlinearity b versus the linear elastic shear modulus G for various materials (See Table 5.1). Red symbols - biological tissues, green - biological polymer gels, blue - synthetic materials.

The Ashby diagram in Fig. 5.1 provides useful information about the elastic response of a material system. Biological tissues, biopolymers and hydrogels show a wide range of nonlinear behavior. The linear elastic modulus can span approximately eight orders of magnitude, while the elastic nonlinearity can vary by approximately five orders of magnitude. Additionally, there is no clear relationship between the linear elastic modulus and the shear nonlinearity across material systems. It is interesting to note that the hydrogels share similar nonlinear characteristics. The agarose gels tested by Barrangout et al. [19] exhibit the same peak in nonlinearity at intermediate polymer concentrations we observed in the PVA-Borax system (Chapter 3). Additionally, the nonlinearity across different compositions of agarose gels, agar combined with gelatin, and PVA-Borax all show a weak dependence with the polymer concentrations. In conclusion, the Ashby diagram can be used for material selection and design. One can choose a material with a certain modulus and nonlinearity to model materials such as biological tissues. In addition, this Ashby diagram provides insight for designing materials in which nonlinear elasticity is a favorable material characteristic.

Chapter 6

Conclusions and Future Outlook

In this thesis, we have discussed how MAOS signatures are useful for understanding the mechanisms driving nonlinearities arising from a change in structure. We showed that the dominant mechanism driving a strain-stiffening response from a transient polymer network (PVA-Borax) is attributed to stretch-induced network structuring by an increase in crosslink density (Chapter 3). It is important to note that not only the linear information $\{G_0, \eta_0, \lambda_0\}$, but the asymptotically nonlinear information $\{[e_1], [v_1], [e_3], [v_3]\}$ are essential ingredients for microstructural inference via model parameters. Our work reinforces the idea that nonlinear information is useful for inferring molecular and network features.

We observed that the strength of the nonlinearity remains relatively constant across a range of compositions of PVA-Borax, while the stiffness of the material (characterized by G_0) varied across two orders of magnitude. The key conclusion is that stretch-induced network structuring allows for softer materials to achieve the same nonlinear response as one with a higher elastic modulus. Our analysis is consistent with video evidence of stretch-induced network structuring for a PVA-Borax composition in which $C_{PVA} < C^*$, where we would expect little overlap of polymer chains and a "weaker" initial network formation (see Fig. A.3).

A natural extension of this current work is to explore how the nonlinearities change as a function of the network conformation. One method for studying this is by imposing an orthogonal superposition of stretch due to flow and oscillatory shear to probe viscoelasticity. In this testing protocol, one measures the viscoelastic properties from a stretched state. Thus, we could stretch the material, facilitate a higher crosslink density due to stretch-induced network structuring, and perform the same analysis from a different network equilibrium. This would be an interesting study aimed to answer the question: how nonlinear can a

material be?

Another method for studying how the nonlinearities change as function of the network conformation is by studying the temperature dependence. The temperature dependent properties of the 2.75 wt% PVA and 1.25 wt% Borax network are shown in Fig. S.3 of the supplementary information in [1]. In summary, both the steady shear viscosity η_0 and relaxation timescale λ_0 show a strong temperature dependence as a decreasing trend with heating. This is expected due to reduced friction and weaker physical crosslinks as the system is heated. The elastic shear modulus G_0 shows a relatively weak temperature dependence. Thus, an increase in temperature results in a comparably stiff material at high frequencies, but with weaker crosslinks that relax faster at elevated temperature. We assume that these trends hold across the range of compositions of PVA-Borax networks discussed in this work. We claim the assumption is warranted because we observed self-similarity across the material systems, especially with respect to the linear viscoelastic results (see Fig. 3.4); thus, the linear parameters should follow similar trends. If G_0 remains relatively constant, but λ_0 decreases with an increase in temperature, we predict that the nonlinearity, χ, will decrease with heating since χ decreases as λ_0 decreases (see Fig. B.45). Interestingly, the multiple changes in slope suggest that there could be limits to network formation as a function of both λ_0 and the concentration of polymer. A study on temperature-dependent nonlinearities would be useful for material design, as temperature could be introduced as another design parameter.

Additionally, future research would include performing the same analysis carried out in this work with different materials. As a first step, we can estimate the strength of finite-extensibility of a PVA polymer chain by forming a polymer network with permanent crosslinks. In this material system, stretch-induced network structuring would not be possible since the crosslinks are not transient, but permanent. This can be achieved by crosslinking PVA by glutaraldehyde. The effects of temperature and crosslinker content on the structural properties of this material system are examined in [70]. Another candidate for performing this analysis is on different hydrogels, such as Agarose. Agarose gels are primarily elastic with a slight frequency-dependence [19], which is different from the rich viscoelastic behavior observed in the PVA-Borax system. Furthermore, Agarose gels are stiffer and more nonlinear compared to PVA-Borax (see Fig. 5.1); thus, it would be interesting to compare the asymptotically nonlinear rheological signatures between the two materials. We envision Ashby-style cross plots similar to Fig. 5.1 which document low-dimensional material

signatures to be useful for material design and material selection for performance.

Appendix A

PVA-Borax Additional Characterization

This Appendix provides supplemental information for the PVA-Borax polymer network discussed in Chapter 2.

A.1 Strain-Rate Data for Overlap Concentration Calculation

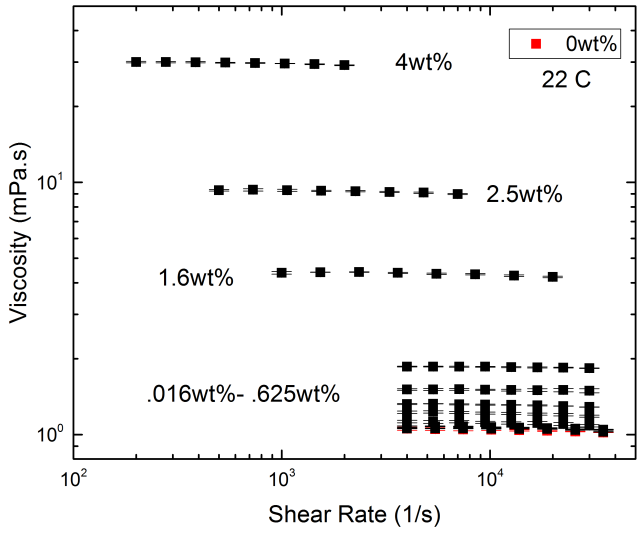

Figure A.1: Shear-rate sweep for each PVA solution shown in Fig. 2.2(a) where $C_{Borax} = 0$. We took the average across all shear rates as the mean viscosity seen in Fig. 2.3.

A.2 Linear Viscoelasticity of PVA Solution

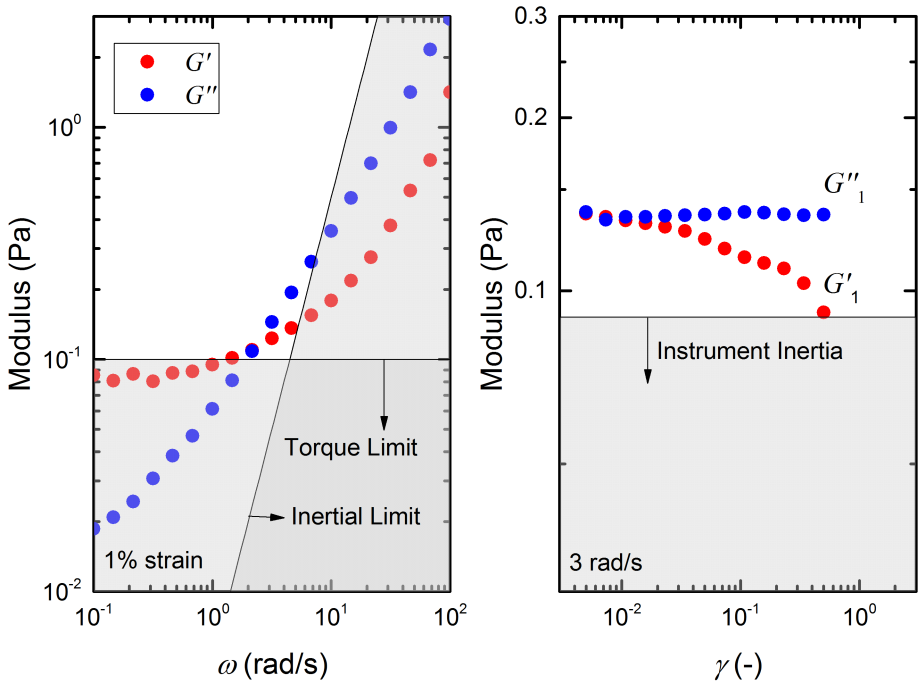

Figure A.2: Viscoelastic characterization of 4 wt% PVA polymer solution. Frequency sweep shows little measurable viscoelasticity. Polymer solution shows strain softening.

A.3 Video Evidence for Stretch-Induced Network Structuring

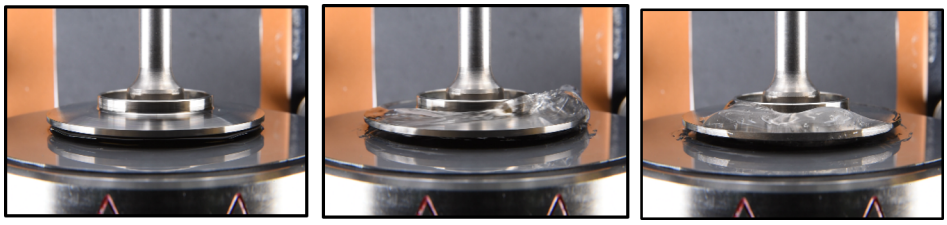

Figure A.3: Visual observations of stretch-induced network structuring for a 1.5 wt% PVA and 1.25 wt% Borax network. Here, we assume there is little overlap of polymer chains since $C_{PVA} < C^*_{PVA}$. The network builds up structure as a constant shear rate of $\dot{\gamma} = 30$ 1/s. Time elapses from left to right.

Appendix B

Supplemental Information for Chapter 3

This Appendix provides supplemental information for the main results in Chapter 3.

B.1 Data for All Compositions

SAOS data and MAOS data for all 11 compositions tested.

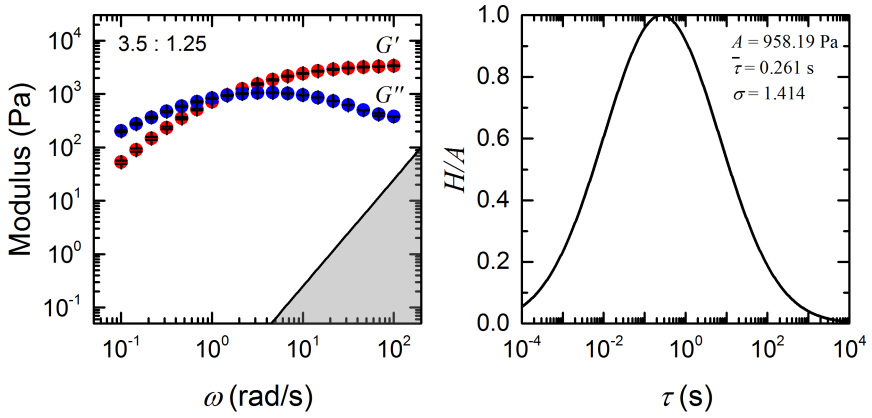

Figure B.1: SAOS frequency-sweep on 3.5 wt% PVA with 1.25 wt% Borax. Error bars are from average of three measurements. Log-normal continuous spectrum shown on right.

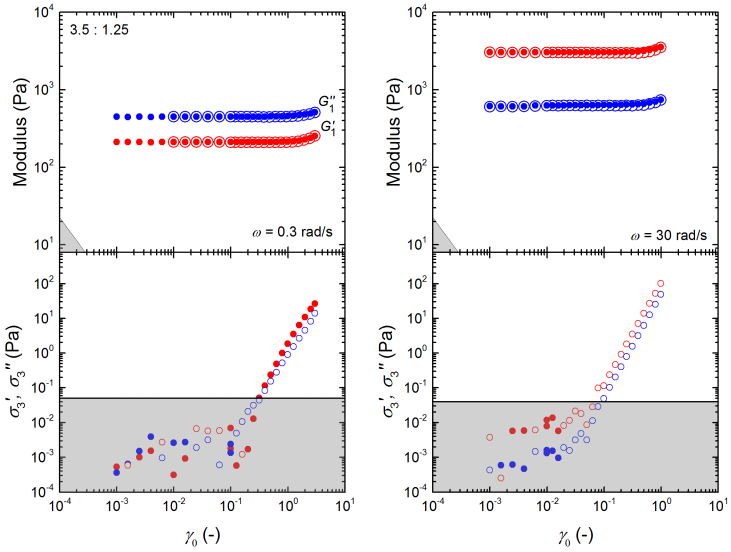

Figure B.2: Strain-sweep on 3.5 wt% PVA with 1.25 wt% Borax (top) and third-harmonic measurements (bottom).

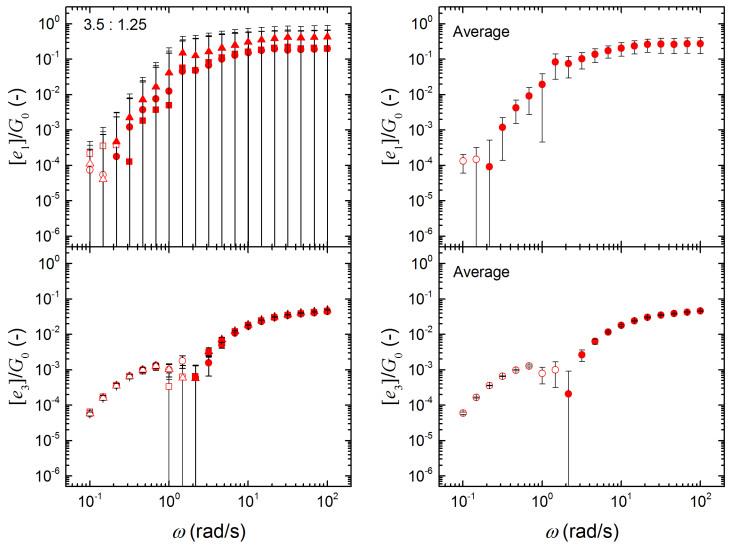

Figure B.3: Measurements of the elastic MAOS material functions $[e_1]$ and $[e_3]$ normalized by the linear elastic modulus G_0 for 3.5 wt% PVA with 1.25 wt% Borax.

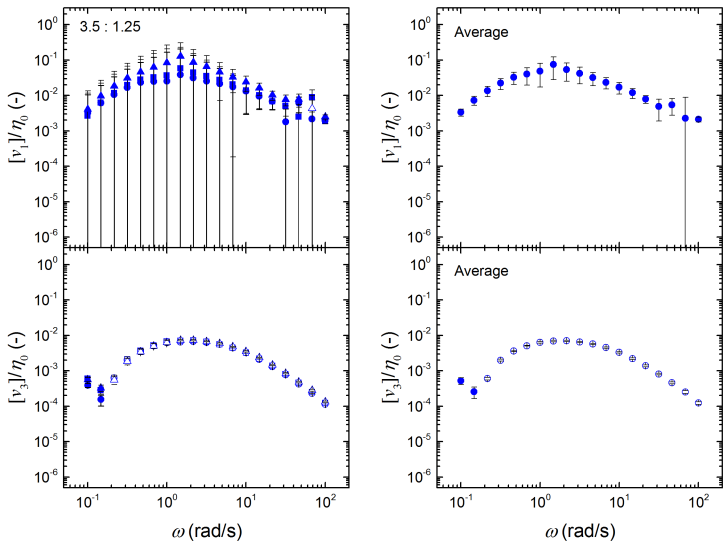

Figure B.4: Measurements of the viscous MAOS material functions $[v_1]$ and $[v_3]$ normalized by the steady shear viscosity η_0 for 3.5 wt% PVA with 1.25 wt% Borax.

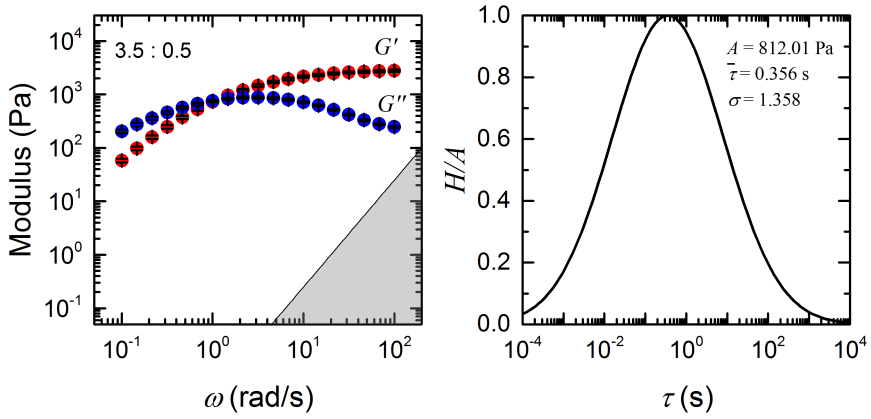

Figure B.5: SAOS frequency-sweep on 3.5 wt% PVA with 0.5 wt% Borax. Error bars are from average of three measurements. Log-normal continuous spectrum shown on right.

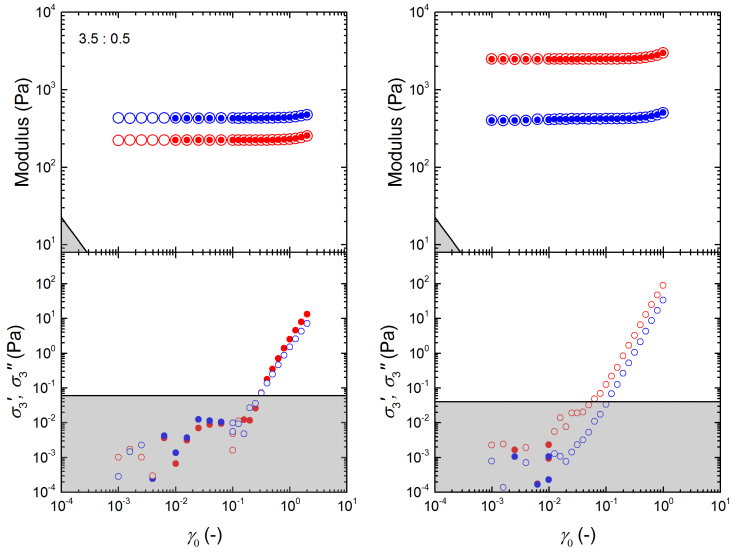

Figure B.6: Strain-sweep on 3.5 wt% PVA with 0.5 wt% Borax (top) and third-harmonic measurements (bottom).

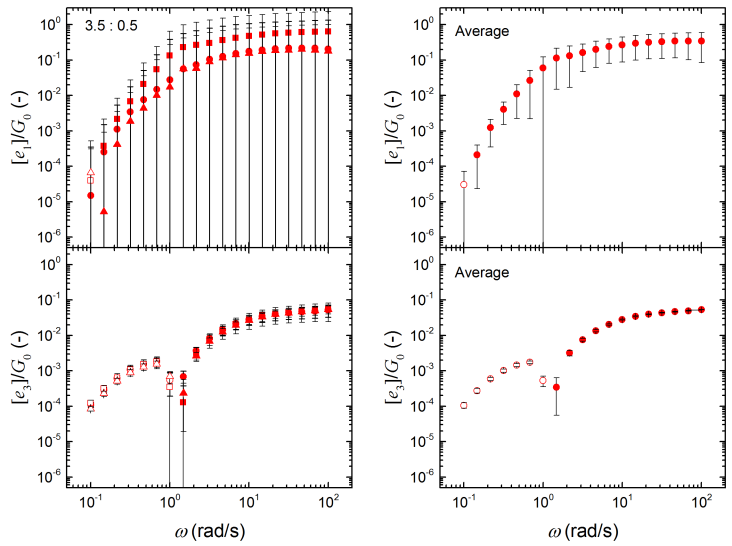

Figure B.7: Measurements of the elastic MAOS material functions $[e_1]$ and $[e_3]$ normalized by the linear elastic modulus G_0 for 3.5 wt% PVA with 0.5 wt% Borax.

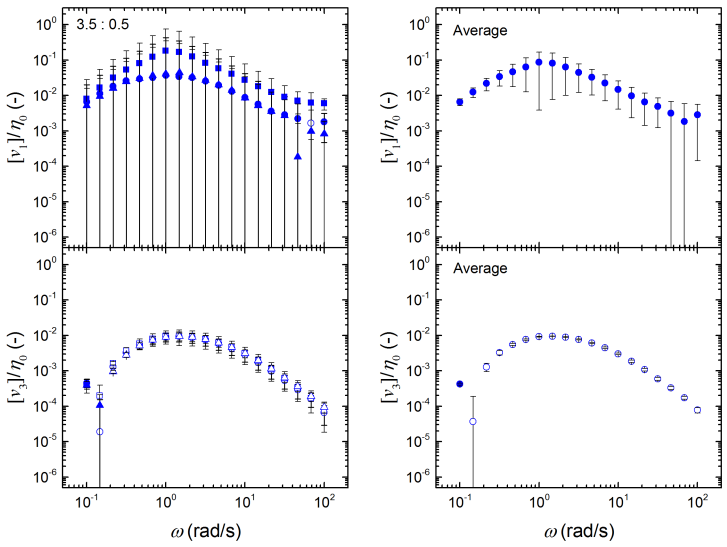

Figure B.8: Measurements of the viscous MAOS material functions $[v_1]$ and $[v_3]$ normalized by the steady shear viscosity η_0 for 3.5 wt% PVA with 0.5 wt% Borax.

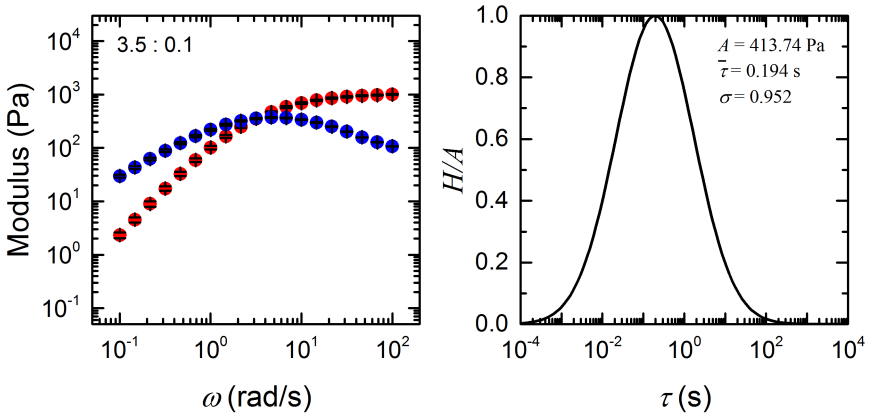

Figure B.9: SAOS frequency-sweep on 3.5 wt% PVA with 0.1 wt% Borax. Error bars are from average of three measurements. Log-normal continuous spectrum shown on right.

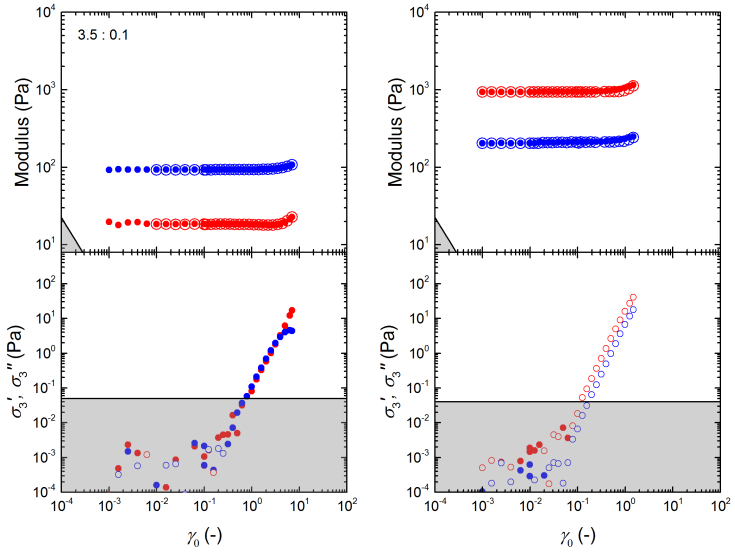

Figure B.10: Strain-sweep on 3.5 wt% PVA with 0.1 wt% Borax (top) and third-harmonic measurements (bottom).

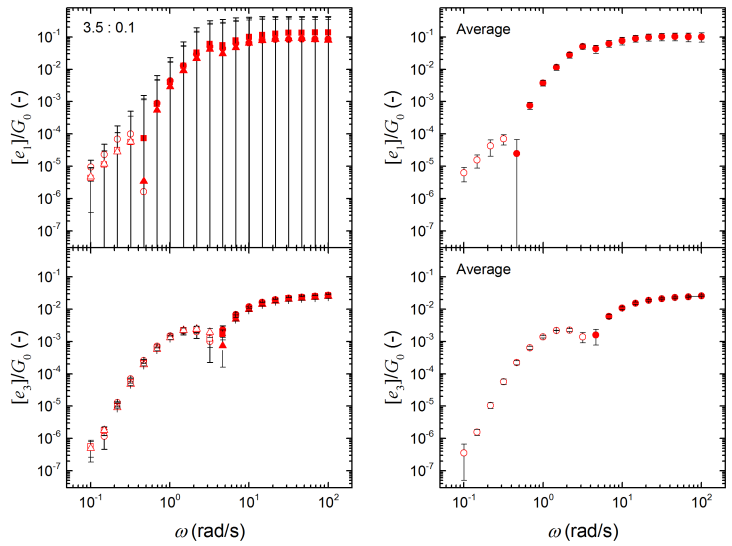

Figure B.11: Measurements of the elastic MAOS material functions $[e_1]$ and $[e_3]$ normalized by the linear elastic modulus G_0 for 3.5 wt% PVA with 0.1 wt% Borax.

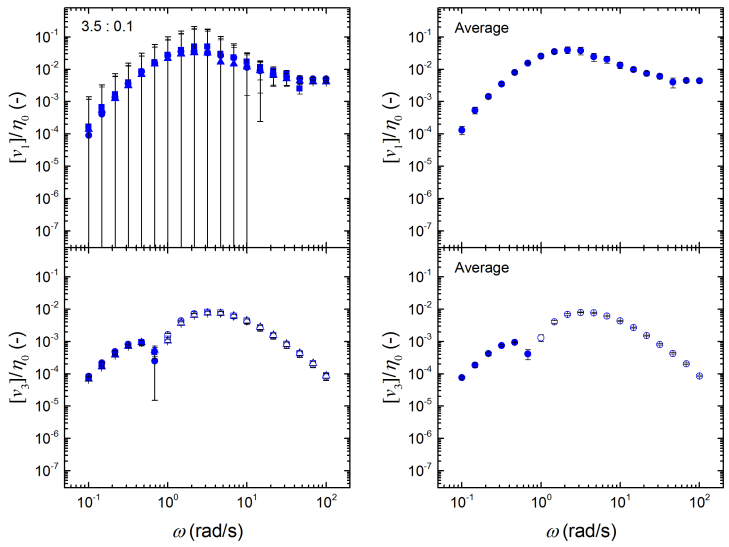

Figure B.12: Measurements of the viscous MAOS material functions $[v_1]$ and $[v_3]$ normalized by the steady shear viscosity η_0 for 3.5 wt% PVA with 0.1 wt% Borax.

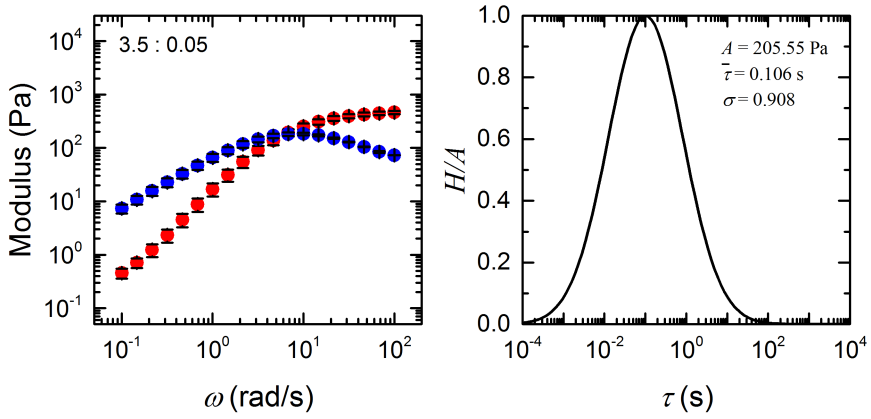

Figure B.13: SAOS frequency-sweep on 3.5 wt% PVA with 0.05 wt% Borax. Error bars are from average of three measurements. Log-normal continuous spectrum shown on right.

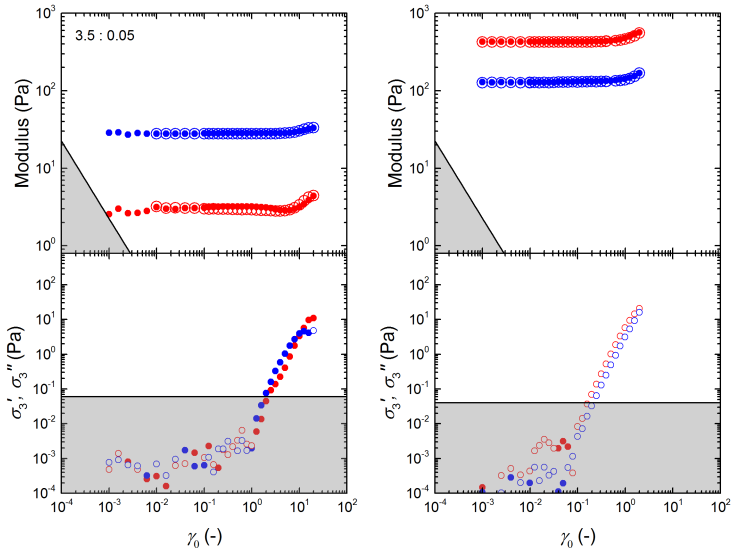

Figure B.14: Strain-sweep on 3.5 wt% PVA with 0.05 wt% Borax (top) and third-harmonic measurements (bottom).

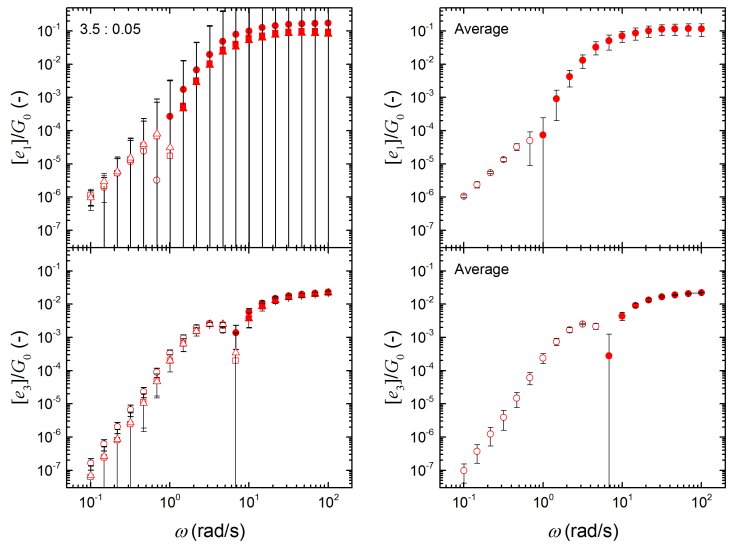

Figure B.15: Measurements of the elastic MAOS material functions $[e_1]$ and $[e_3]$ normalized by the linear elastic modulus G_0 for 3.5 wt% PVA with 0.05 wt% Borax.

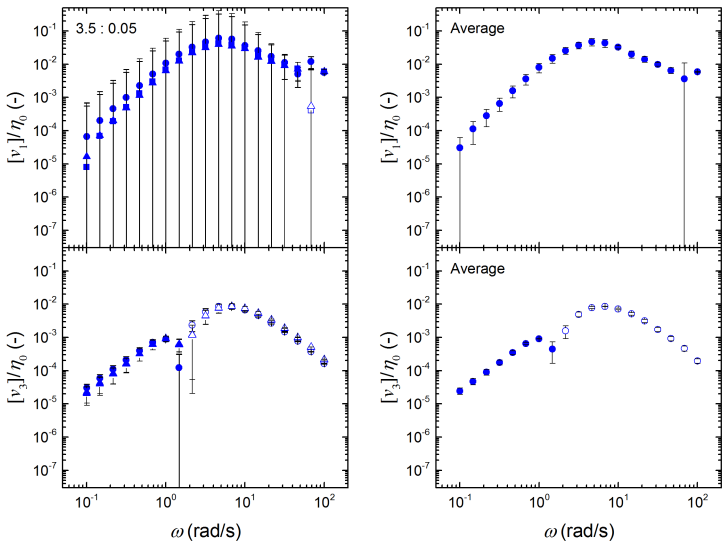

Figure B.16: Measurements of the viscous MAOS material functions $[v_1]$ and $[v_3]$ normalized by the steady shear viscosity η_0 for 3.5 wt% PVA with 0.05 wt% Borax.

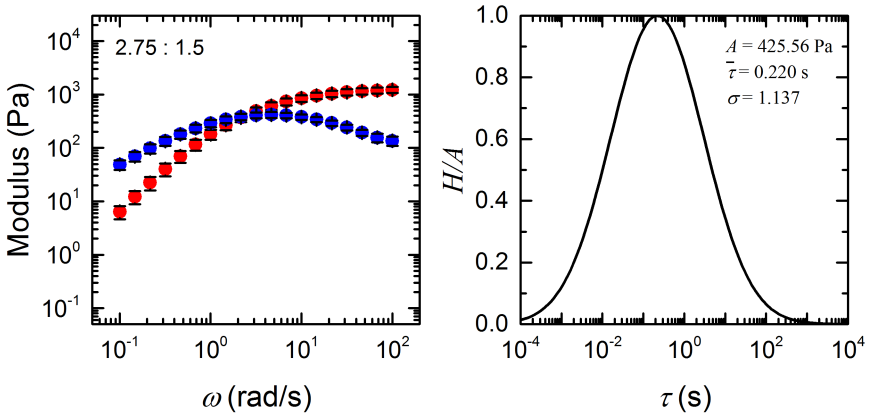

Figure B.17: SAOS frequency-sweep on 2.75 wt% PVA with 1.5 wt% Borax. Error bars are from average of three measurements. Log-normal continuous spectrum shown on right.

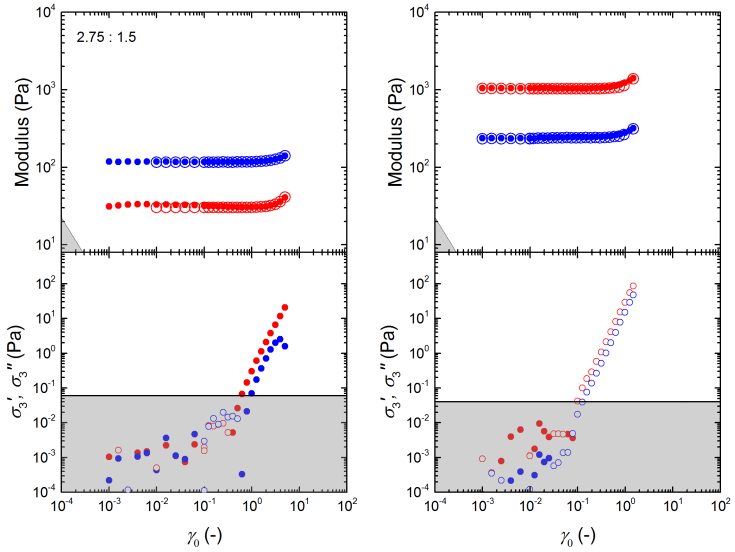

Figure B.18: Strain-sweep on 2.75 wt% PVA with 1.5 wt% Borax (top) and third-harmonic measurements (bottom).

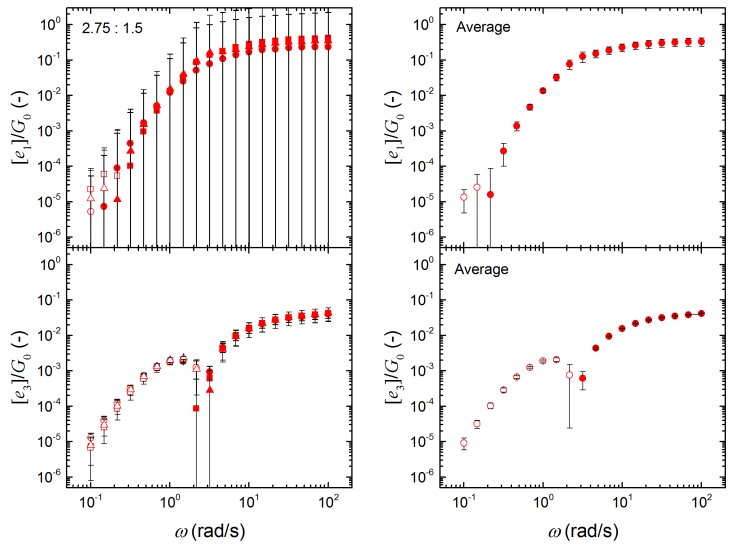

Figure B.19: Measurements of the elastic MAOS material functions $[e_1]$ and $[e_3]$ normalized by the linear elastic modulus G_0 for 2.75 wt% PVA with 1.5 wt% Borax.

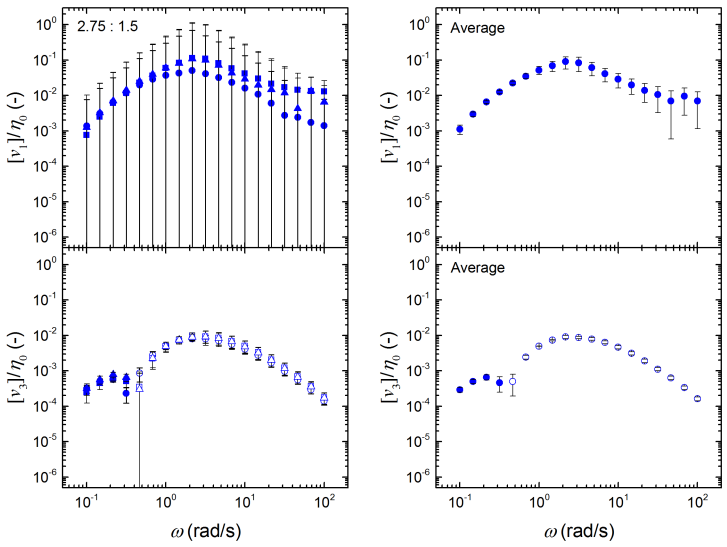

Figure B.20: Measurements of the viscous MAOS material functions $[v_1]$ and $[v_3]$ normalized by the steady shear viscosity η_0 for 2.75 wt% PVA with 1.5 wt% Borax.

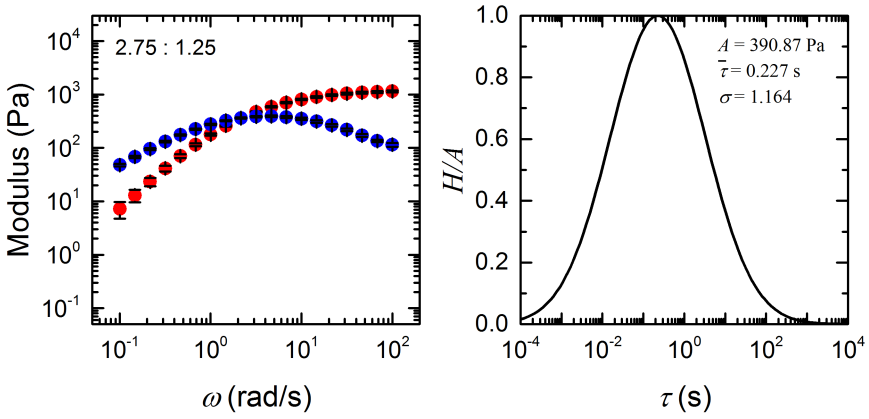

Figure B.21: SAOS frequency-sweep on 2.75 wt% PVA with 1.25 wt% Borax. Error bars are from average of three measurements. Log-normal continuous spectrum shown on right.

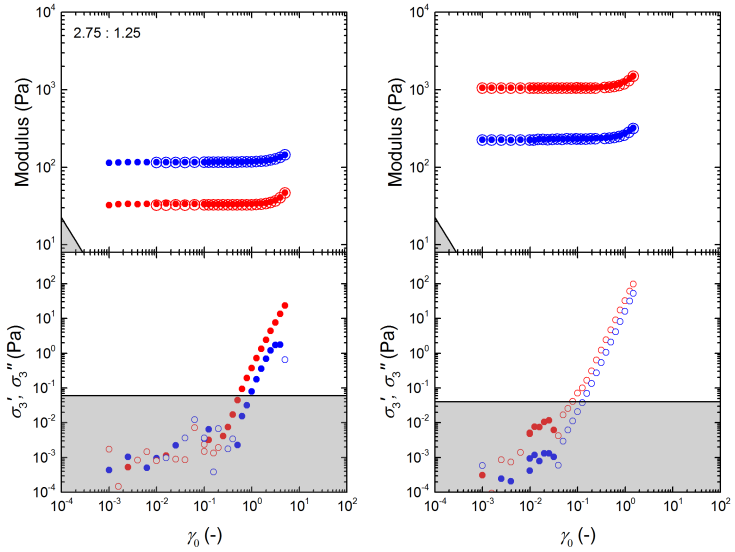

Figure B.22: Strain-sweep on 2.75 wt% PVA with 1.25 wt% Borax (top) and third-harmonic measurements (bottom).

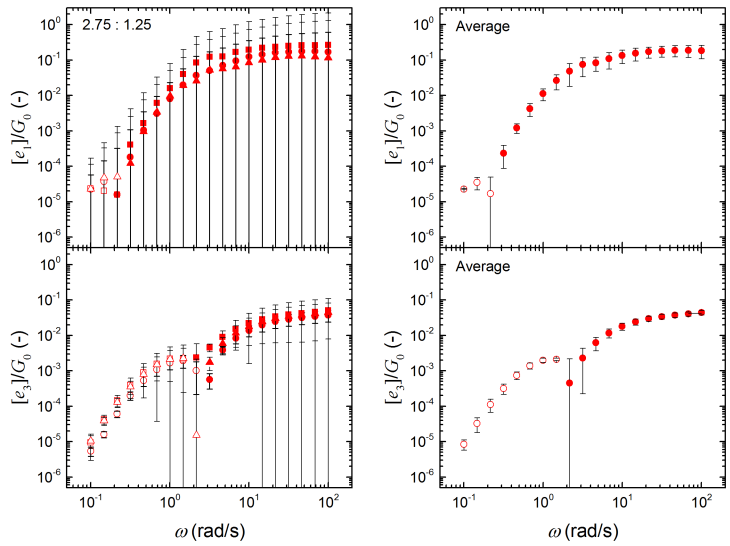

Figure B.23: Measurements of the elastic MAOS material functions $[e_1]$ and $[e_3]$ normalized by the linear elastic modulus G_0 for 2.75 wt% PVA with 1.25 wt% Borax.

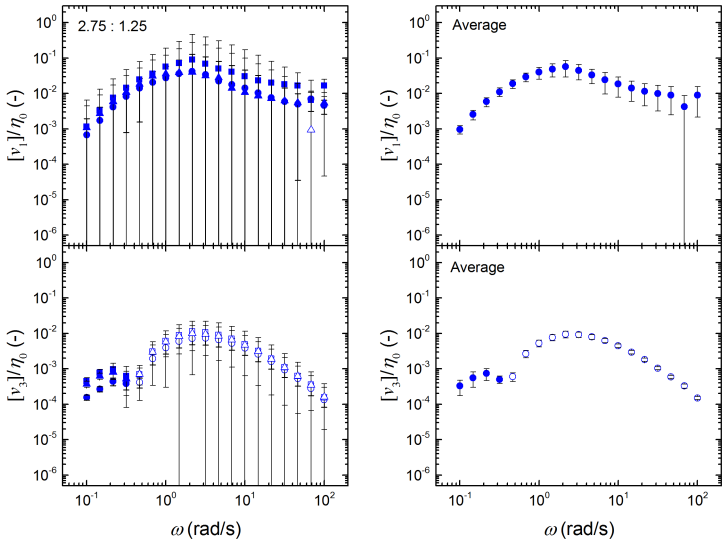

Figure B.24: Measurements of the viscous MAOS material functions $[v_1]$ and $[v_3]$ normalized by the steady shear viscosity η_0 for 2.75 wt% PVA with 1.25 wt% Borax.

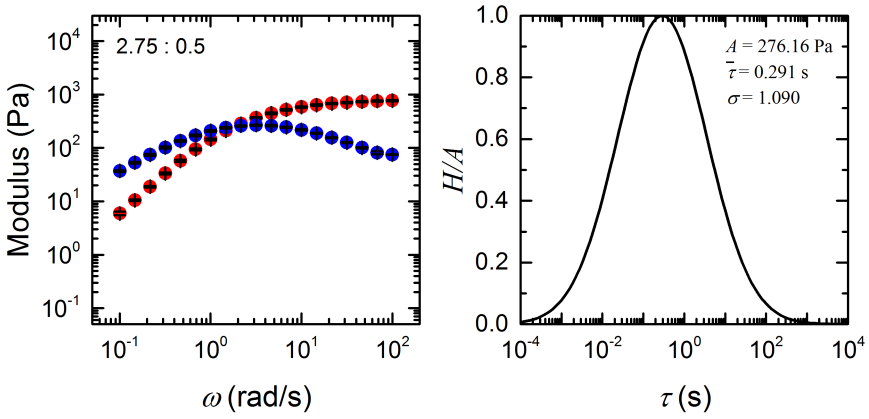

Figure B.25: SAOS frequency-sweep on 2.75 wt% PVA with 0.5 wt% Borax. Error bars are from average of three measurements. Log-normal continuous spectrum shown on right.

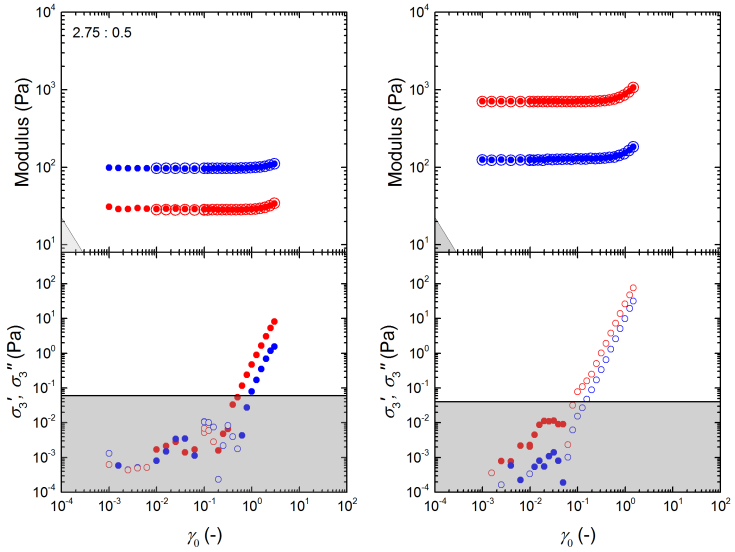

Figure B.26: Strain-sweep on 2.75 wt% PVA with 0.5 wt% Borax (top) and third-harmonic measurements (bottom).

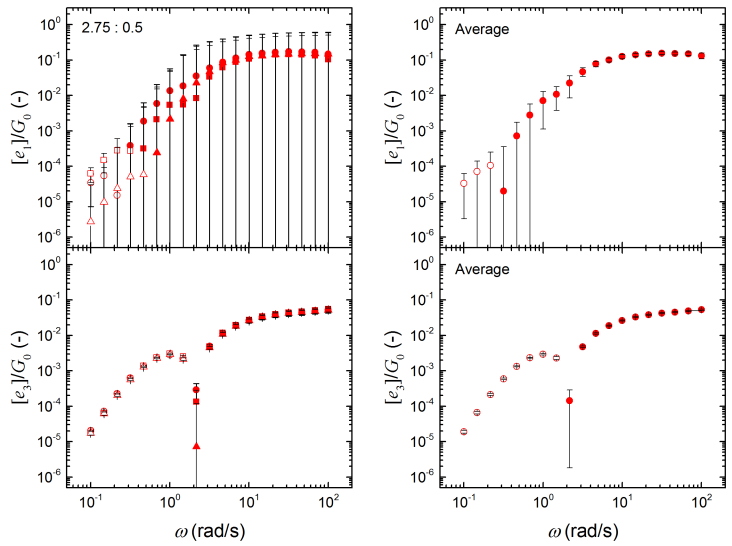

Figure B.27: Measurements of the elastic MAOS material functions $[e_1]$ and $[e_3]$ normalized by the linear elastic modulus G_0 for 2.75 wt% PVA with 0.5 wt% Borax.

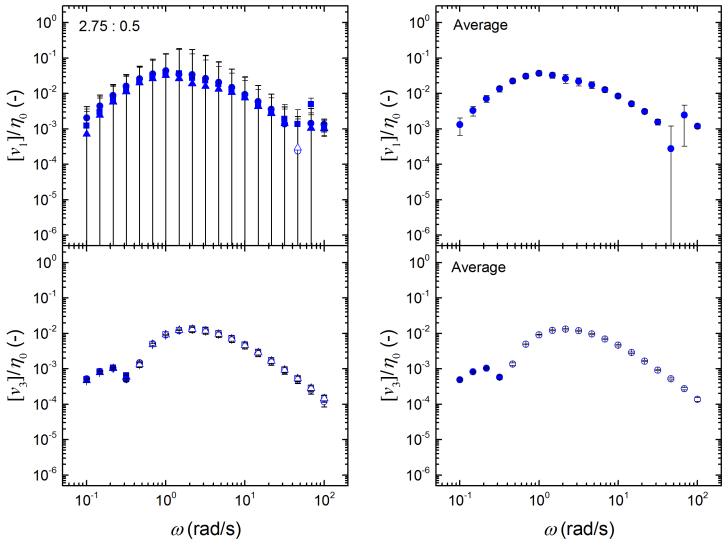

Figure B.28: Measurements of the viscous MAOS material functions $[v_1]$ and $[v_3]$ normalized by the steady shear viscosity η_0 for 2.75 wt% PVA with 0.5 wt% Borax.

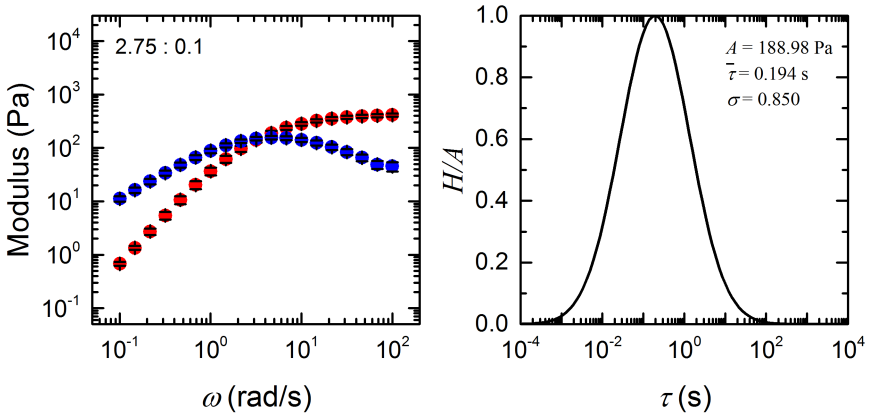

Figure B.29: SAOS frequency-sweep on 2.75 wt% PVA with 0.1 wt% Borax. Error bars are from average of three measurements. Log-normal continuous spectrum shown on right.

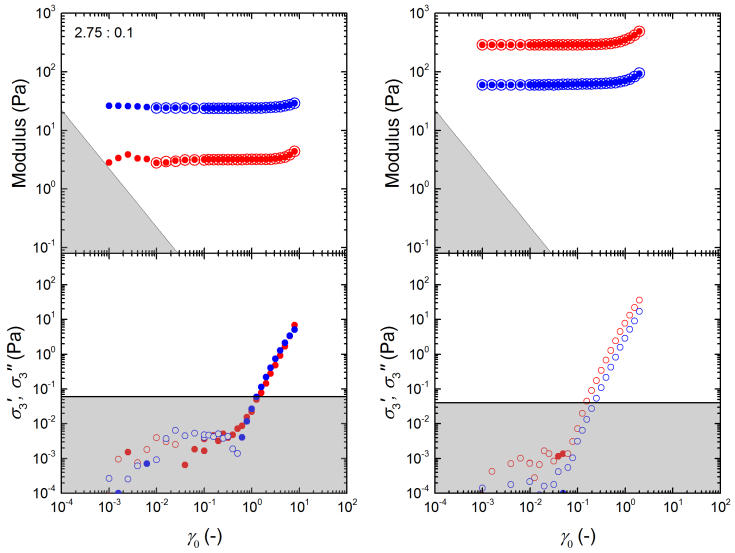

Figure B.30: Strain-sweep on 2.75 wt% PVA with 0.1 wt% Borax (top) and third-harmonic measurements (bottom).

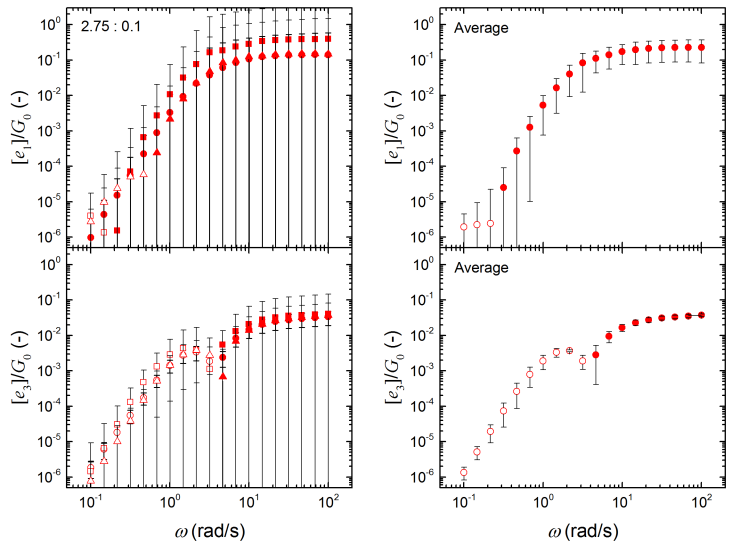

Figure B.31: Measurements of the elastic MAOS material functions $[e_1]$ and $[e_3]$ normalized by the linear elastic modulus G_0 for 2.75 wt% PVA with 0.1 wt% Borax.

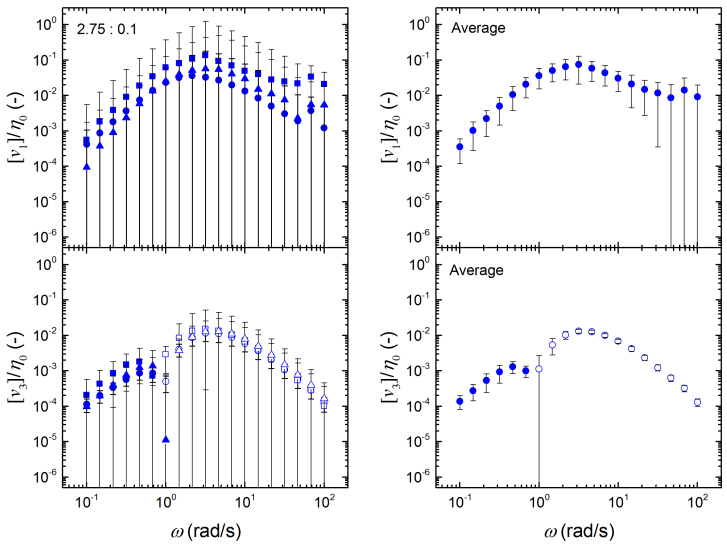

Figure B.32: Measurements of the viscous MAOS material functions $[v_1]$ and $[v_3]$ normalized by the steady shear viscosity η_0 for 2.75 wt% PVA with 0.1 wt% Borax.

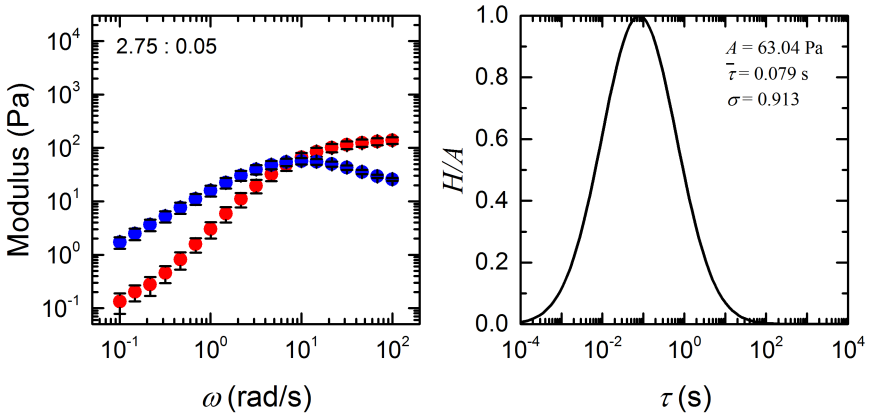

Figure B.33: SAOS frequency-sweep on 2.75 wt% PVA with 0.05 wt% Borax. Error bars are from average of three measurements. Log-normal continuous spectrum shown on right.

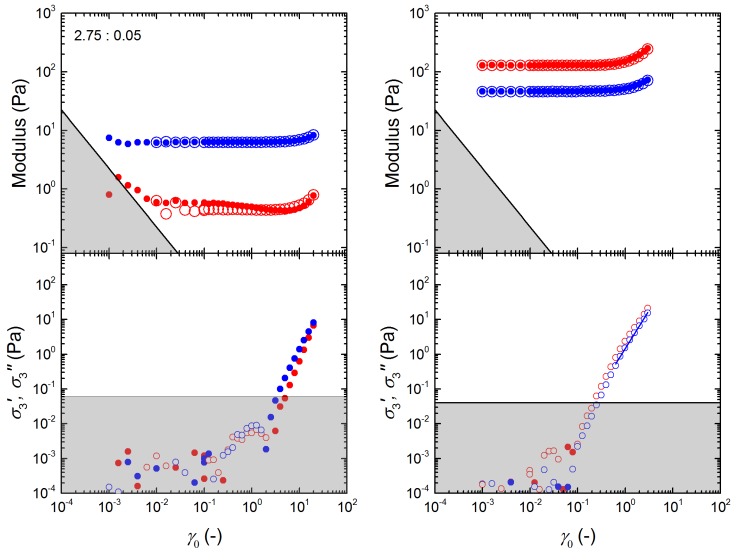

Figure B.34: Strain-sweep on 2.75 wt% PVA with 0.05 wt% Borax (top) and third-harmonic measurements (bottom).

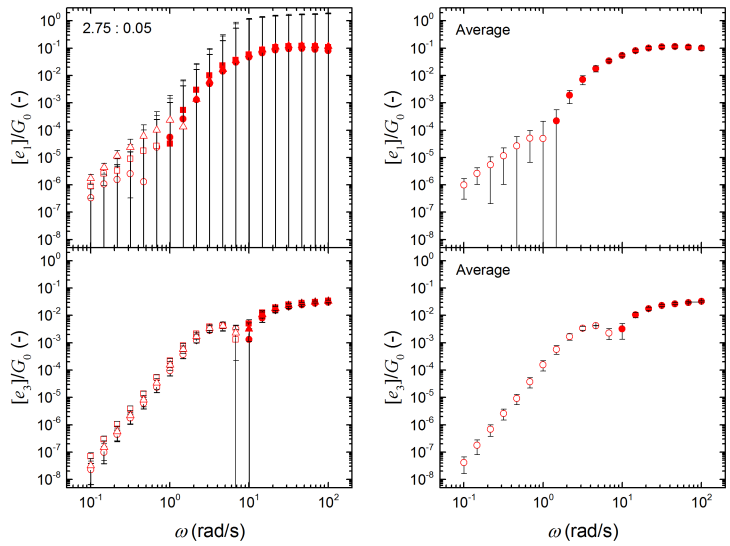

Figure B.35: Measurements of the elastic MAOS material functions $[e_1]$ and $[e_3]$ normalized by the linear elastic modulus G_0 for 2.75 wt% PVA with 0.05 wt% Borax.

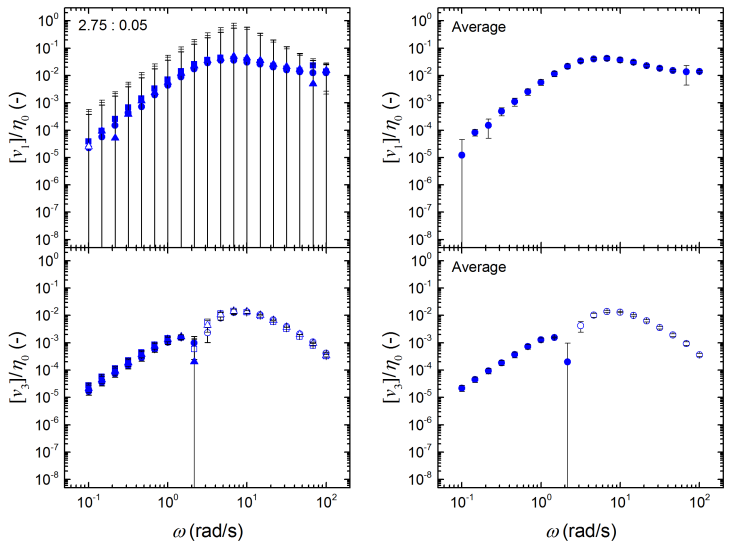

Figure B.36: Measurements of the viscous MAOS material functions $[v_1]$ and $[v_3]$ normalized by the steady shear viscosity η_0 for 2.75 wt% PVA with 0.05 wt% Borax.

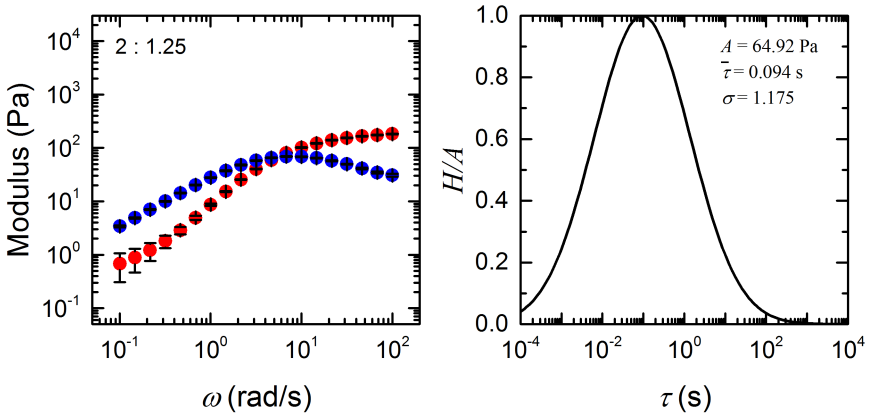

Figure B.37: SAOS frequency-sweep on 2 wt% PVA with 1.25 wt% Borax. Error bars are from average of three measurements. Log-normal continuous spectrum shown on right.

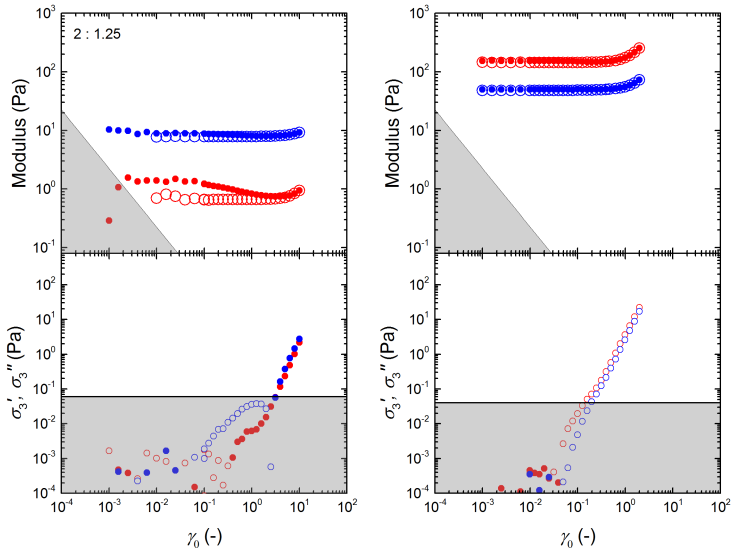

Figure B.38: Strain-sweep on 2 wt% PVA with 1.25 wt% Borax (top) and third-harmonic measurements (bottom).

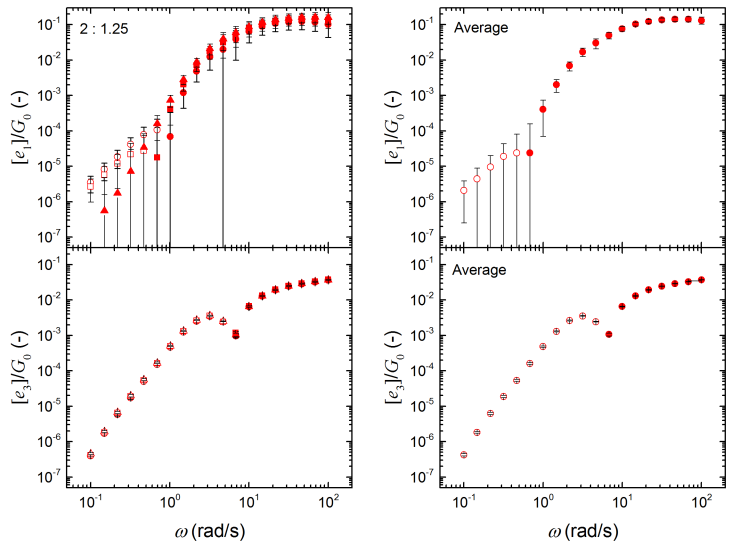

Figure B.39: Measurements of the elastic MAOS material functions $[e_1]$ and $[e_3]$ normalized by the linear elastic modulus G_0 for 2 wt% PVA with 1.25 wt% Borax.

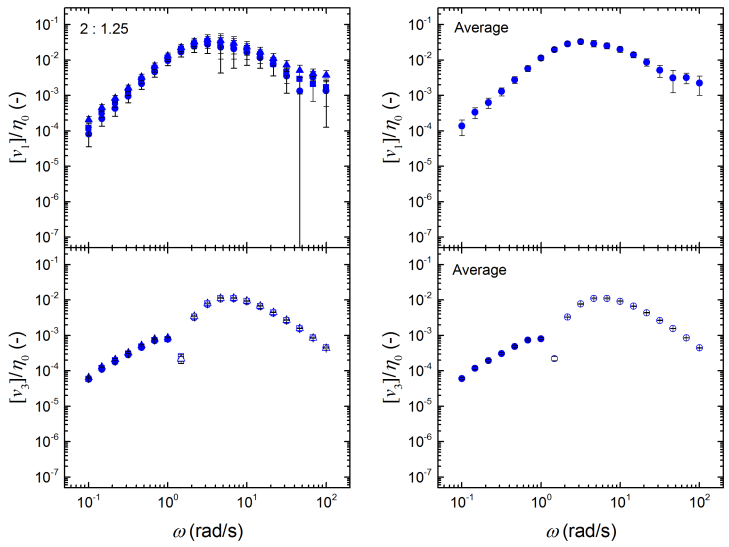

Figure B.40: Measurements of the viscous MAOS material functions $[v_1]$ and $[v_3]$ normalized by the steady shear viscosity η_0 for 2 wt% PVA with 1.25 wt% Borax.

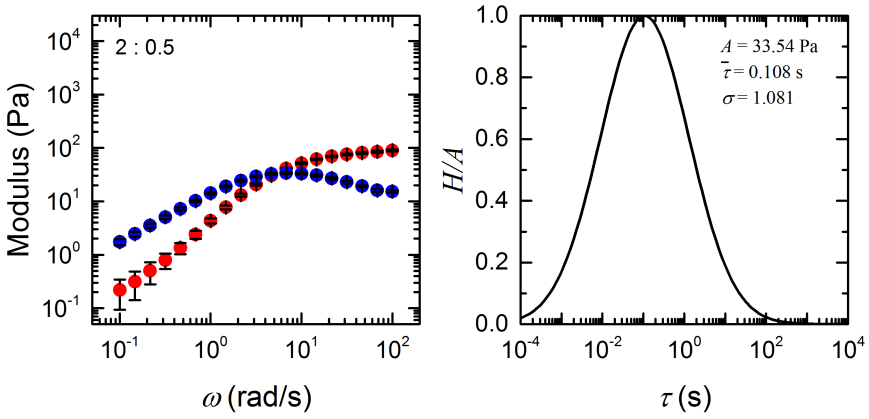

Figure B.41: SAOS frequency-sweep on 2 wt% PVA with 0.5 wt% Borax. Error bars are from average of three measurements. Log-normal continuous spectrum shown on right.

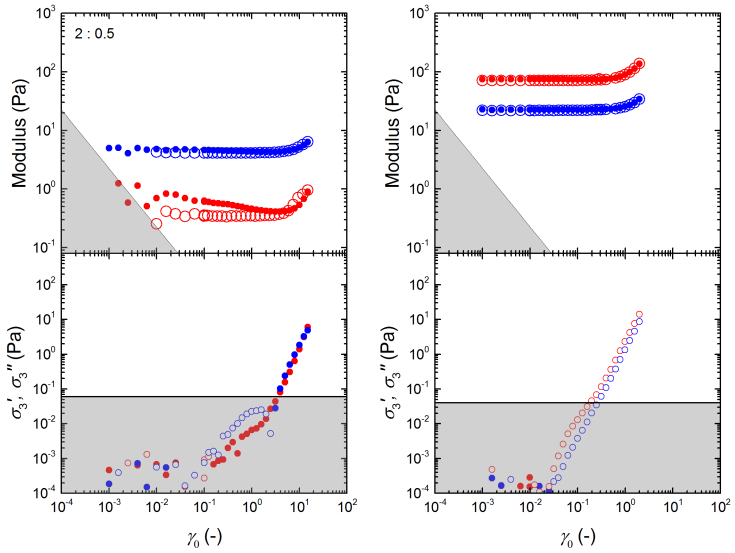

Figure B.42: Strain-sweep on 2 wt% PVA with 0.5 wt% Borax (top) and third-harmonic measurements (bottom).

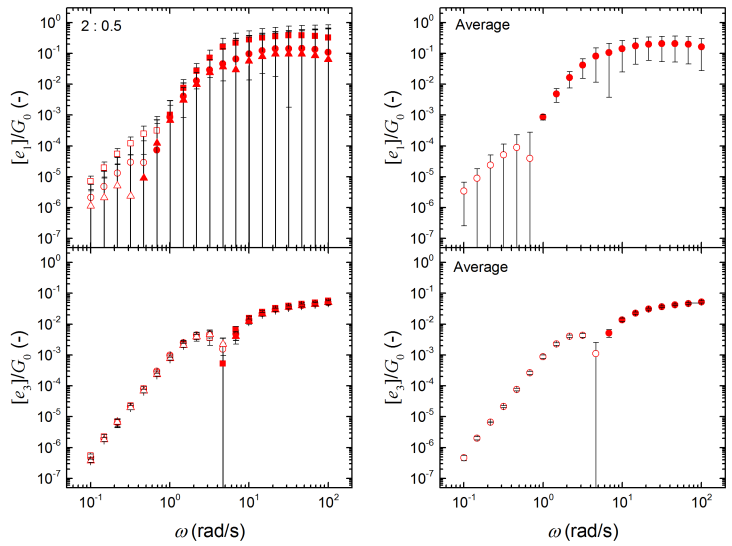

Figure B.43: Measurements of the elastic MAOS material functions $[e_1]$ and $[e_3]$ normalized by the linear elastic modulus G_0 for 2 wt% PVA with 0.5 wt% Borax.

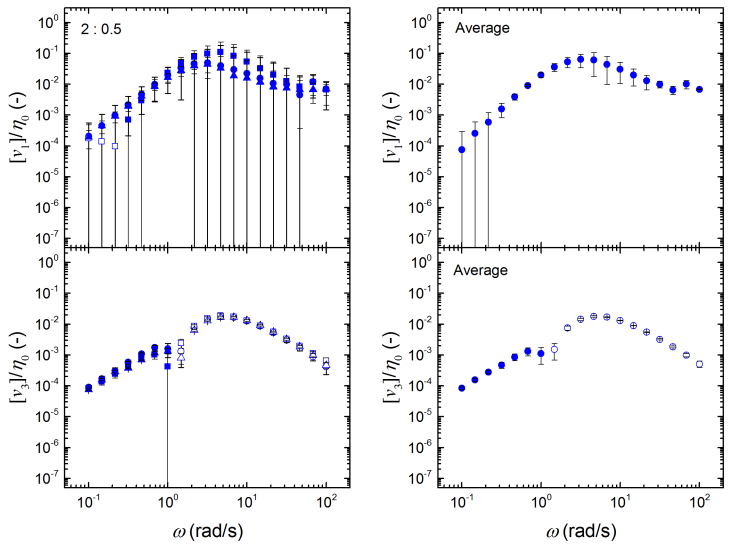

Figure B.44: Measurements of the viscous MAOS material functions $[v_1]$ and $[v_3]$ normalized by the steady shear viscosity η_0 for 2 wt% PVA with 0.5 wt% Borax.

B.1.1 Low-Dimensional Descriptors

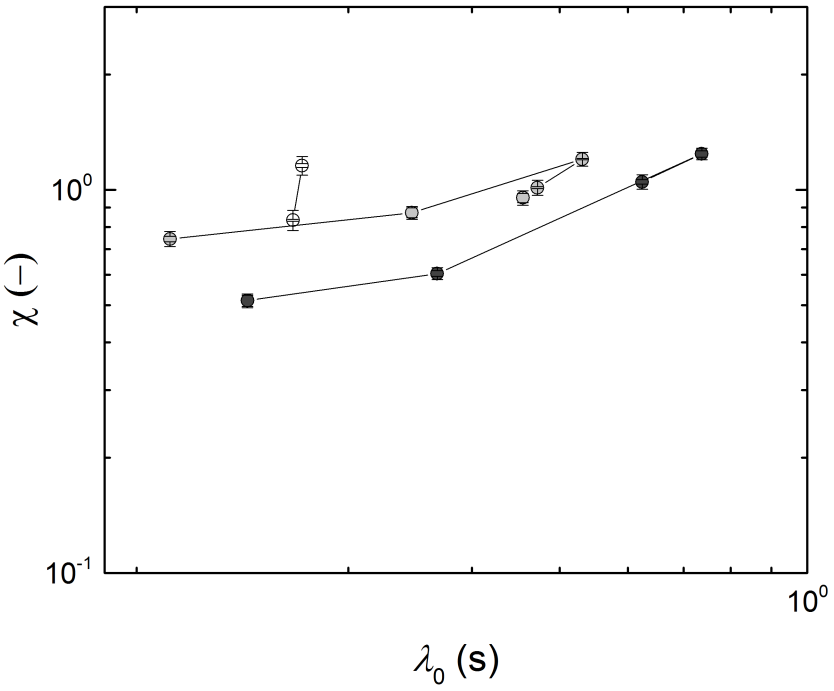

Figure B.45: Nonlinear model parameter χ as a function of relaxation timescale λ_0.

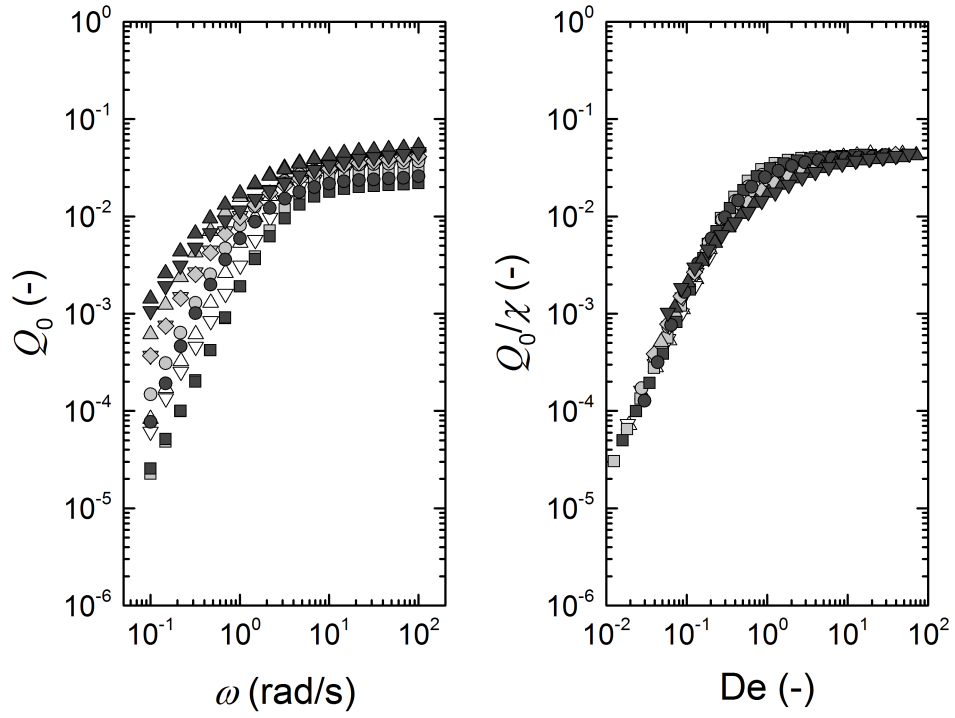

Figure B.46: Course MAOS measure Q_0 as a function of frequency. The nonlinear model parameter χ and the relaxation timescale λ_0 normalize and collapse the data for 11 composotions of PVA-Borax networks.

B.1.2 Error Propagation

The MAOS frequency-sweep method for extracting MAOS material functions (discussed in Section 2.2.1.1) involves a one-point calculation for third-harmonic asymptotic nonlinearities and a two-point calculation for first-harmonic asymptotic nonlinearities (see Eqns. 2.3-2.6) [31]. This section provides the formula for error propagation used for measuring asymptotic nonlinearities using the MAOS frequency-sweep method.

The error propagation formula is defined as

$$\delta_x^2 = \sum_i \left(\frac{\partial x}{\partial y_i}\right)^2 \delta_{y_i}^2, \tag{B.1}$$

where x is a function of variables y_i. For the intrinsic nonlinearities defined in Eqns. 2.3-2.6, the error propagates as

$$\delta_{[e_1]}^2 = \left(\frac{1}{\gamma_M^2}\right)^2 \delta_{G'_{1,M}}^2 + \left(-\frac{1}{\gamma_M^2}\right)^2 \delta_{G'_{1,S}}^2 \tag{B.2}$$

$$\delta^2_{[v_1]} = \left(\frac{1}{\omega\gamma_M^2}\right)^2 \delta^2_{G''_{1,M}} + \left(-\frac{1}{\omega\gamma_M^2}\right)^2 \delta^2_{G''_{1,S}} \tag{B.3}$$

$$\delta^2_{[e_3]} = \left(-\frac{1}{\gamma_M^2}\right)^2 \delta^2_{G'_{3,M}} \tag{B.4}$$

$$\delta^2_{[v_3]} = \left(\frac{1}{\omega\gamma_M^2}\right)^2 \delta^2_{G''_{3,M}}, \tag{B.5}$$

where γ_M is the strain amplitude from the MAOS frequency-sweep, ω is the frequency, and here, the error in measuring first- and third-harmonic moduli δ_G is taken as the standard deviation of three SAOS and MAOS frequency-sweeps. The errors in the asymptotic nonlinear parameters are used throughout this work in the propagation of error for other material functions (e.g. the first-harmonic relative nonlinear material function $\frac{[e_1]}{G_0}$) using Eqn. B.1.

B.2 Model Analysis

The following process for inferring network features for a transiently crosslinked polymer network is outlined in the Appendix of [1]. We use polymer physics ideas in which a polymer is treated as an arrangement of independent ideal coil strands (polymer chains) with end-to-end distance between crosslinks defined as

$$Q_{eq} = l\sqrt{N_x C_\infty}, \tag{B.6}$$

where N_x is the number of backbone bonds between crosslinks, C_∞ is the characteristic ratio, and l is the length of the C-C bond. The maximum extensional distance of the polymer chain between crosslinks L is defined as,

$$L = N_x l \cos(\theta/2), \tag{B.7}$$

where θ is the bond (valance) angle. One can define the ratio of Eqns. B.6 and B.7 as

$$\frac{Q_{eq}}{L} = \frac{1}{\sqrt{N_x}} \frac{\sqrt{C_\infty}}{\cos(\theta/2)} = \frac{3.56}{\sqrt{N_x}} \tag{B.8}$$

using $C_\infty = 8.3$ and $\theta = 71^\circ$ as PVA specific quantities used in [1]. Finally, the Kuhn length b_K is defined in [1] as

$$b_K = \frac{C_\infty l}{\cos(\theta/2)} \approx 16\ \mathring{A}. \tag{B.9}$$

Equations B.6-B.9 are polymer specific quantities and are constant.

We used the strain-stiffening transiently crosslinked polymer network model of Bharadwaj et al. [1] in Section 3.3 to infer network features of multiple compositions of PVA-Borax. The shear modulus was defined in Eqn. 3.5 as

$$G_0 = \frac{1}{3} n\left(Q_{eq}\right) h\left(Q_{eq}\right) Q_{eq}^2. \tag{B.10}$$

We assumed a functional form (FENE model) for the nonlinear force-extension law $h(Q)$ which describes the finite-extensibility of the polymer,

$$h(Q)_{FENE} = \frac{3k_BT}{b_kL}\left(1 - \frac{Q^2}{L^2}\right)^{-1}. \tag{B.11}$$

The nonlinear contribution from a FENE nonlinear force-extension law is derived using Eqn. 3.7, here as

$$\hbar = \left.\frac{\partial \ln h(Q)}{\partial \ln Q}\right|_{Q=Q_{eq}}, \tag{B.12}$$

resulting in

$$\hbar_{FENE} = 2\frac{Q_{eq}^2}{L^2}\left(1 - \frac{Q_{eq}^2}{L^2}\right)^{-1}. \tag{B.13}$$

Additionally, we assumed that the ensemble average crosslink density is approximated by one of a cubic lattice,

$$n(Q) \approx \frac{1}{Q^3}. \tag{B.14}$$

We estimate network features using the polymer specific quantities defined in Eqns. B.6-B.9 and the descriptors modeling the polymer network defined in Eqns. B.10-B.14.

Substituting Eqns. B.11 and B.14 into Eqn. B.10 and using Eqns. B.6-B.9 reveals that the shear modulus G_0 is only dependent on N_x,

$$\begin{aligned} G_{0,FENE} &= \frac{n\left(Q_{eq}\right) k_B T}{b_K/L} \frac{Q_{eq}^2}{L^2} \left(1 - \frac{Q_{eq}^2}{L^2}\right)^{-1} \\ &= \frac{k_B T}{b_K/L} \frac{1}{Q_{eq}^3} \frac{Q_{eq}^2}{L^2} \left(1 - \frac{Q_{eq}^2}{L^2}\right)^{-1} \\ &= \frac{k_B T}{b_K} \frac{1}{Q_{eq} L} \left(1 - \frac{Q_{eq}^2}{L^2}\right)^{-1} \\ &= \frac{k_B T}{b_K} \frac{1}{l^2\sqrt{C_\infty}\cos(\theta/2)} \frac{1}{N_x^{3/2}} \left(1 - \frac{3.56^2}{N_x}\right)^{-1} \\ &= A \frac{1}{N_x^{3/2}} \left(1 - \frac{3.56^2}{N_x}\right)^{-1}, \end{aligned} \tag{B.15}$$

where A is a constant defined by the polymer specific quantities in Eqns. B.6-B.9, temperature $T = 25°\text{C}$, and the Boltzmann constant k_B,

$$\begin{aligned} A &= \frac{k_B T}{b_K} \frac{1}{l^2\sqrt{C_\infty}\cos(\theta/2)} \\ &\approx 4 \times 10^7. \end{aligned} \tag{B.16}$$

Thus for each composition of a PVA polymer network, A is constant (same polymer and same testing environment), G_0 is composition-dependent and experimentally measured, and the only unknown in Eqn. B.15 is N_x. We rearrange Eqn. B.15 to set up an algebraic equation used to solve for N_x as

$$N_x^{1/2}\left(N_x - 3.56^2\right) = \frac{A}{G_0}. \tag{B.17}$$

Therefore, for any elastic shear modulus G_0, one can use an equation solver to calculate the number of backbone bonds between crosslinks N_x using Eqn. B.17. In other words, the experimentally measured shear modulus G_0 is a function of N_x. Consequently, G_0 is a function of the ratio $\frac{Q_{eq}}{L}$ by a change of variables using Eqn. B.8. We calculate Q_{eq} and L independently using Eqns. B.6 and B.7, respectively, to define the ratio $\frac{Q_{eq}}{L}$ for each composition. Finally, the ratio $\frac{Q_{eq}}{L}$ predicts a value for the finite-extensibility contribution $\not{h}$ using Eqn. B.13.

In summary, we compute $\hbar(G_0; k_BT, C_\infty, l, \theta)$ by combining Eqns. B.8, B.9, B.16, B.17 with Eqn. B.13. Comparing $\hbar$ to χ identifies the relative contribution from stretch-induced crosslinking by

$$\chi = \hbar + \eta. \tag{B.18}$$

We use this procedure to infer network features of 11 compositions of a PVA-Borax polymer network (results in Table 3.3).

Appendix C

Universal Nonlinear Parameter Relation Derivations

This Appendix provides the derivation of Eqn. 5.3 and the Taylor Series expansion for the Fung Model discussed in Chapter 5.

C.1 Relation Between MAOS Parameter and Universal Nonlinear Parameter

Here, we provide the derivation of Eqn. 5.3. For this derivation, we compare the strain-dependent elastic moduli for the constitutive equation defined for the universal nonlinear parameter b and the low-dimensional MAOS descriptor $[e_1]$. The shear stress response for a purely elastic material (Eqn. 1.2) is defined as

$$\begin{aligned} \sigma(\gamma) &= G(\gamma)\gamma \\ &= G_0\gamma\left(1 + b\gamma^2 + O(\gamma^4)\right), \end{aligned} \tag{C.1}$$

where the elastic modulus depends on the shear strain,

$$G(\gamma) = G_0\left(1 + b\gamma^2 + O(\gamma^4)\right). \tag{C.2}$$

The shear stress for an oscillation measurement can be represented by a Fourier series involving higher harmonics (Eqn. 1.4),

$$\sigma(t) = \sum_n \sigma'_n sin(n\omega t) + \sigma''_n cos(n\omega t). \tag{C.3}$$

Using the Chebyshev framework discussed in Section 1.2, the first harmonic elastic modulus (Eqn. 1.9) is defined as

$$\begin{aligned} G'_1(\gamma_0, \omega_0) &= \frac{\sigma'_1}{\gamma} \\ &= G'_{LVE} + [e_1]|_{\omega_0} \gamma_0^2 + O\left(\gamma_0^4\right) \\ &= G'_{LVE}\left(1 + \frac{[e_1]}{G'_{LVE}}\gamma^2\right). \end{aligned} \tag{C.4}$$

We plug in the oscillation strain $\gamma(t) = \gamma_0 \sin(\omega t)$ to Eqn. C.1,

$$\sigma = G_0\gamma_0\left(sin(\omega t) + b\gamma_0^2 \sin^3(\omega t)\right). \tag{C.5}$$

Expanding the Chebyshev stress in Eqn. C.3 to third order and only using the elastic coefficients $\sigma'_n = G'_n\gamma_0$ (to compare the elasticity of materials) yields

$$\begin{aligned} \sigma &= \gamma_0\left(G'_1 sin(\omega t) + G'_3 sin(3\omega t)\right) \\ &= \gamma_0\left(G'_1 sin(\omega t) + 3G'_3 sin(\omega t) - 4G'_3 sin^3(\omega t)\right) \end{aligned} \tag{C.6}$$

using the trigonometric identity

$$sin(3\omega t) = -4sin^3(\omega t) + 3sin(\omega t). \tag{C.7}$$

Equating coefficients for $sin(\omega t)$ in Eqns. C.5 and C.6 yields

$$G_0 = G'_1 + 3G'_3, \tag{C.8}$$

while equating coefficients for $sin^3(\omega t)$ yields

$$G_0\gamma_0^2 b = -4G_3'. \tag{C.9}$$

Solving for G_1' in Eqn. C.8 and plugging in G_3' found in Eqn. C.9 yields

$$G_1' = G_0\left(1 + \frac{3}{4}\gamma_0^2 b\right). \tag{C.10}$$

Finally, we compare Eqn. C.10 to Eqn. C.4 to derive the relation between b and $[e_1]$

$$b = \frac{4}{3}\frac{[e_1]}{G'_{LVE}}, \tag{C.11}$$

where we assume G'_{LVE} is approximately equal to the linear storage modulus G_0. This should be a fair assumption if the oscillation measurement is taken in the elastic limit where $De > 1$.

C.2 Taylor Series Expansion for Fung Model

Here, we derive the Taylor Series expansion for the Fung model defined in Eqn. 5.10,

$$\sigma(\gamma) = G_0\gamma e^{\alpha\gamma^2}. \tag{C.12}$$

To compute the relation defined in Eqn. 5.12 we must perform a Taylor Series expansion for Eqn. C.12 about small strains ($\gamma = 0$),

$$\sigma(\gamma) \approx \sigma(\gamma)|_{\gamma=0} + \left.\frac{d\sigma}{d\gamma}\right|_{\gamma=0}\frac{\gamma}{1!} + \left.\frac{d^2\sigma}{d\gamma^2}\right|_{\gamma=0}\frac{\gamma^2}{2!} + \left.\frac{d^3\sigma}{d\gamma^3}\right|_{\gamma=0}\frac{\gamma^3}{3!} + \cdots. \tag{C.13}$$

The derivatives (up to third order) and their values at $\gamma = 0$ are defined as follows

$$\sigma(\gamma)|_{\gamma=0} = 0 \tag{C.14}$$

$$\frac{d\sigma}{d\gamma} = G_0 e^{\alpha\gamma^2} + 2G_0\alpha\gamma^2 e^{\alpha\gamma^2} \tag{C.15}$$

$$\left.\frac{d\sigma}{d\gamma}\right|_{\gamma=0} = G_0 \tag{C.16}$$

$$\frac{d^2\sigma}{d\gamma^2} = 6G_0\alpha\gamma e^{\alpha\gamma^2} + 4G_0\alpha^2\gamma^3 e^{\alpha\gamma^2} \tag{C.17}$$

$$\left.\frac{d^2\sigma}{d\gamma^2}\right|_{\gamma=0} = 0 \tag{C.18}$$

$$\frac{d^3\sigma}{d\gamma^3} = 6G_0\alpha e^{\alpha\gamma^2} + 24G_0\alpha^2\gamma^2 e^{\alpha\gamma^2} + 8G_0\alpha^3\gamma^4 e^{\alpha\gamma^2} \tag{C.19}$$

$$\left.\frac{d^3\sigma}{d\gamma^3}\right|_{\gamma=0} = 6G_0\alpha. \tag{C.20}$$

Plugging in Eqns. C.14-C.20 to Eqn. C.13 yields

$$\begin{aligned}\sigma(\gamma) &\approx G_0\gamma + G_0\alpha\gamma^3 \\ &= G_0\gamma\left(1+\alpha\gamma^2\right).\end{aligned} \tag{C.21}$$

Thus, comparing Eqn. C.21 to Eqn. C.1 yields the relation between the Fung nonlinear model parameter α and the universal nonlinear parameter b:

$$b = \alpha. \tag{C.22}$$

Bibliography

[1] N. Ashwin Bharadwaj, Kenneth S. Schweizer, and Randy H. Ewoldt. "A strain stiffening theory for transient polymer networks under asymptotically nonlinear oscillatory shear". In: *Journal of Rheology* 61.4 (2017), pp. 643–665.

[2] S P Beeby, M J Tudor, and NM White. "Energy harvesting vibration sources for microsystems applications". In: *Measurement science and technology* 17.12 (2006), R175.

[3] Roszaidi Ramlan, MJ Brennan, BR Mace, et al. "Potential benefits of a non-linear stiffness in an energy harvesting device". In: *Nonlinear Dynamics* 59.4 (2010), pp. 545–558.

[4] B Ando, S Baglio, C Trigona, et al. "Nonlinear mechanism in MEMS devices for energy harvesting applications". In: *Journal of Micromechanics and Microengineering* 20.12 (2010), p. 125020.

[5] Mohammed F Daqaq. "On intentional introduction of stiffness nonlinearities for energy harvesting under white Gaussian excitations". In: *Nonlinear Dynamics* 69.3 (2012), pp. 1063–1079.

[6] Mohammed F Daqaq, Ravindra Masana, Alper Erturk, et al. "On the role of nonlinearities in vibratory energy harvesting: a critical review and discussion". In: *Applied Mechanics Reviews* 66.4 (2014), p. 040801.

[7] Yuan-cheng Fung. *Biomechanics: mechanical properties of living tissues*. Springer Science & Business Media, 2013.

[8] Cornelis Storm, Jennifer J Pastore, Fred C MacKintosh, et al. "Nonlinear elasticity in biological gels". In: *Nature* 435.7039 (2005), pp. 191–194.

[9] Shaokoon Cheng, Elizabeth C Clarke, and Lynne E Bilston. "Rheological properties of the tissues of the central nervous system: a review". In: *Medical engineering & physics* 30.10 (2008), pp. 1318–1337.

[10] Kozaburo Hayashi. "Experimental approaches on measuring the mechanical properties and constitutive laws of arterial walls". In: *Transactions-American society of mechanical engineers journal of biomechanical engineering* 115 (1993), pp. 481–481.

[11] Huichin Yuan, Stefanida Kononov, Francisco SA Cavalcante, et al. "Effects of collagenase and elastase on the mechanical properties of lung tissue strips". In: *Journal of applied physiology* 89.1 (2000), pp. 3–14.

[12] Lynne E Bilston, Zizhen Liu, and Nhan Phan-Thien. “Large strain behaviour of brain tissue in shear: some experimental data and differential constitutive model”. In: *Biorheology* 38.4 (2001), pp. 335–345.

[13] Pablo Fernández, Lutz Heymann, Albrecht Ott, et al. “Shear rheology of a cell monolayer”. In: *New Journal of Physics* 9.11 (2007), p. 419.

[14] Kristy Tan, Shaokoon Cheng, Lauriane Jugé, et al. “Characterising soft tissues under large amplitude oscillatory shear and combined loading”. In: *Journal of biomechanics* 46.6 (2013), pp. 1060–1066.

[15] Gaynor M Kavanagh and Simon B Ross-Murphy. “Rheological characterisation of polymer gels”. In: *Progress in Polymer Science* 23.3 (1998), pp. 533–562.

[16] Eric A Appel, Jesus del Barrio, Xian Jun Loh, et al. “Supramolecular polymeric hydrogels”. In: *Chemical Society Reviews* 41.18 (2012), pp. 6195–6214.

[17] T Inoue and K Osaki. “Rheological properties of poly (vinyl alcohol)/sodium borate aqueous solutions”. In: *Rheologica acta* 32.6 (1993), pp. 550–555.

[18] AP Balgude, X Yu, A Szymanski, et al. “Agarose gel stiffness determines rate of DRG neurite extension in 3D cultures”. In: *Biomaterials* 22.10 (2001), pp. 1077–1084.

[19] Lisa M Barrangou, Christopher R Daubert, and E Allen Foegeding. “Textural properties of agarose gels. I. Rheological and fracture properties”. In: *Food Hydrocolloids* 20.2 (2006), pp. 184–195.

[20] Theo Z Pavan, Ernest L Madsen, Gary R Frank, et al. “Nonlinear elastic behavior of phantom materials for elastography”. In: *Physics in medicine and biology* 55.9 (2010), p. 2679.

[21] CP Salisbury and DS Cronin. “Mechanical properties of ballistic gelatin at high deformation rates”. In: *Experimental mechanics* 49.6 (2009), pp. 829–840.

[22] Junhua Zhang, Christopher R Daubert, and E Allen Foegeding. “Characterization of polyacrylamide gels as an elastic model for food gels”. In: *Rheologica Acta* 44.6 (2005), pp. 622–630.

[23] Lisa M Barrangou, MaryAnne Drake, Christopher R Daubert, et al. “Textural properties of agarose gels. II. Relationships between rheological properties and sensory texture”. In: *Food Hydrocolloids* 20.2 (2006), pp. 196–203.

[24] Randy H Ewoldt, N Ashwin Bharadwaj, et al. “Low-dimensional intrinsic material functions for nonlinear viscoelasticity”. In: *Rheol. Acta* 52.3 (2013), pp. 201–219.

[25] JM Maerker and SW Sinton. “Rheology resulting from shear-induced structure in associating polymer solutions”. In: *Journal of Rheology* 30.1 (1986), pp. 77–99.

[26] TA Witten Jr and MH Cohen. “Crosslinking in shear-thickening ionomers”. In: *Macromolecules* 18.10 (1985), pp. 1915–1918.

[27] JG Savins. “Shear thickening phenomena in poly (vinyl) alcohol-borate complexes”. In: *Rheologica Acta* 7.1 (1968), pp. 87–93.

[28] G Marrucci, S Bhargava, and SL Cooper. “Models of shear-thickening behavior in physically crosslinked networks”. In: *Macromolecules* 26.24 (1993), pp. 6483–6488.

[29] Y Serero, V Jacobsen, J-F Berret, et al. “Evidence of nonlinear chain stretching in the rheology of transient networks”. In: *Macromolecules* 33.5 (2000), pp. 1841–1847.

[30] A Vaccaro and G Marrucci. “A model for the nonlinear rheology of associating polymers”. In: *Journal of non-newtonian fluid mechanics* 92.2 (2000), pp. 261–273.

[31] Piyush K Singh, Johannes M Soulages, and Randy H Ewoldt. “Frequency-sweep MAOS: An accelerated and material economical medium amplitude oscillatory shear method”. *in prep*.

[32] Kyu Hyun, En Su Baik, Kyung Hyun Ahn, et al. “Fourier-transform rheology under medium amplitude oscillatory shear for linear and branched polymer melts”. In: *Journal of Rheology* 51.6 (2007), pp. 1319–1342.

[33] Kyu Hyun and Manfred Wilhelm. “Establishing a new mechanical nonlinear coefficient Q from FT-rheology: First investigation of entangled linear and comb polymer model systems”. In: *Macromolecules* 42.1 (2008), pp. 411–422.

[34] Manfred H Wagner, Víctor Hugo Rolón-Garrido, Kyu Hyun, et al. “Analysis of medium amplitude oscillatory shear data of entangled linear and model comb polymers”. In: *Journal of Rheology* 55.3 (2011), pp. 495–516.

[35] N Ashwin Bharadwaj and Randy H Ewoldt. “Constitutive model fingerprints in medium-amplitude oscillatory shear”. In: *Journal of Rheology* 59.2 (2015), pp. 557–592.

[36] Allen C Pipkin. *Lectures on viscoelasticity theory*. Vol. 7. Springer Science & Business Media, 2012.

[37] Manfred Wilhelm. “Fourier-transform rheology”. In: *Macromolecular materials and engineering* 287.2 (2002), pp. 83–105.

[38] Randy H Ewoldt. “Defining nonlinear rheological material functions for oscillatory shear”. In: *Journal of Rheology* 57.1 (2013), pp. 177–195.

[39] Christopher W Macosko. *Rheology: principles, measurements, and applications*. Wiley-vch, 1994.

[40] Shi-Qing Wang, S Ravindranath, and PE Boukany. “Homogeneous shear, wall slip, and shear banding of entangled polymeric liquids in simple-shear rheometry: A roadmap of nonlinear rheology”. In: *Macromolecules* 44.2 (2011), pp. 183–190.

[41] Randy H Ewoldt, Michael T Johnston, and Lucas M Caretta. “Experimental challenges of shear rheology: how to avoid bad data”. In: *Complex Fluids in Biological Systems*. Springer, 2015, pp. 207–241.

[42] A Kate Gurnon and Norman J Wagner. “Large amplitude oscillatory shear (LAOS) measurements to obtain constitutive equation model parameters: Giesekus model of banding and nonbanding wormlike micelles”. In: *Journal of Rheology* 56.2 (2012), pp. 333–351.

[43] Ewoldt, R H and Winter, P B, and McKinley G H. *MITlaos*. Software - MATLAB-based data analysis software for characterizing nonlinear viscoelastic responses to oscillatory shear strain.

[44] Chung Yuan Chen and Tzyy-Lung Yu. “Dynamic light scattering of poly (vinyl alcohol)-borax aqueous solution near overlap concentration”. In: *Polymer* 38.9 (1997), pp. 2019–2025.

[45] G Keita, A Ricard, R Audebert, et al. “The poly (vinyl alcohol)-borate system: influence of polyelectrolyte effects on phase diagrams”. In: *Polymer* 36.1 (1995), pp. 49–54.

[46] Hidenobu Kurokawa, Mitsuhiro Shibayama, Takeshi Ishimaru, et al. “Phase behaviour and sol-gel transition of poly (vinyl alcohol)-borate complex in aqueous solution”. In: *Polymer* 33.10 (1992), pp. 2182–2188.

[47] Hsiu-Li Lin, Yuan-Feng Liu, T Leon Yu, et al. “Light scattering and viscoelasticity study of poly (vinyl alcohol)–borax aqueous solutions and gels”. In: *Polymer* 46.15 (2005), pp. 5541–5549.

[48] Norio Nemoto, Akihiro Koike, and Kunihiro Osaki. “Dynamic light scattering and dynamic viscoelasticity of poly (vinyl alcohol) in aqueous borax solutions. 2. Polymer concentration and molecular weight effects”. In: *Macromolecules* 29.5 (1996), pp. 1445–1451.

[49] Akihiro Koike, Norio Nemoto, Tadashi Inoue, et al. “Dynamic light scattering and dynamic viscoelasticity of poly (vinyl alcohol) in aqueous borax solutions. 1. Concentration effect”. In: *Macromolecules* 28.7 (1995), pp. 2339–2344.

[50] Gang Huang, Huanhuan Zhang, Yulin Liu, et al. “Strain Hardening Behavior of Poly (vinyl alcohol)/Borate Hydrogels”. In: *Macromolecules* 50.5 (2017), pp. 2124–2135.

[51] Rheosense. *m-VROC-APP-25 (2-13)*. Procedure - to determine the molecular size of proteins, polymers, or macromolecules by measuring intrinsic viscosity.

[52] John D Ferry. *Viscoelastic properties of polymers*. John Wiley & Sons, 1980.

[53] John M Dealy. "Official nomenclature for material functions describing the response of a viscoelastic fluid to various shearing and extensional deformations". In: *Journal of Rheology* 39.1 (1995), pp. 253–265.

[54] Qicong Ying and Benjamin Chu. "Overlap concentration of macromolecules in solution". In: *Macromolecules* 20.2 (1987), pp. 362–366.

[55] Rongshi Cheng. "On the concentration regimes of a flexible-chain polymer solution". In: *Macromolecular Symposia*. Vol. 124. 1. Wiley Online Library. 1997, pp. 27–34.

[56] M Daoud, JP Cotton, B Farnoux, et al. "Solutions of flexible polymers. Neutron experiments and interpretation". In: *Macromolecules* 8.6 (1975), pp. 804–818.

[57] Pierre-Gilles De Gennes. *Scaling concepts in polymer physics*. Cornell university press, 1979.

[58] Michael Rubinstein and Ralph H Colby. *Polymer physics*. Vol. 23. Oxford University Press New York, 2003.

[59] Robert Byron Bird, Robert Calvin Armstrong, Ole Hassager, et al. *Dynamics of polymeric liquids*. Vol. 1. Wiley New York, 1977.

[60] N Ashwin Bharadwaj, Randy H Ewoldt, et al. "Single-point parallel disk correction for asymptotically nonlinear oscillatory shear". In: *Rheologica Acta* 54.3 (2015), pp. 223–233.

[61] Nicholas W Tschoegl. *The phenomenological theory of linear viscoelastic behavior: an introduction*. Springer Science & Business Media, 2012.

[62] Harold R Warner Jr. "Kinetic theory and rheology of dilute suspensions of finitely extendible dumbbells". In: *Industrial & Engineering Chemistry Fundamentals* 11.3 (1972), pp. 379–387.

[63] Akihiko Takada, Miki Nishimura, Akihiro Koike, et al. "Dynamic light scattering and dynamic viscoelasticity of poly (vinyl alcohol) in aqueous borax solutions. 4. Further investigation on polymer concentration and molecular weight dependencies". In: *Macromolecules* 31.2 (1998), pp. 436–443.

[64] Dimitri Merger and Manfred Wilhelm. "Intrinsic nonlinearity from LAOStrain—experiments on various strain-and stress-controlled rheometers: a quantitative comparison". In: *Rheologica Acta* 53.8 (2014), pp. 621–634.

[65] Randy H Ewoldt, AE Hosoi, and Gareth H McKinley. "New measures for characterizing nonlinear viscoelasticity in large amplitude oscillatory shear". In: *Journal of Rheology* 52.6 (2008), pp. 1427–1458.

[66] Raymond W Ogden. *Non-linear elastic deformations*. Courier Corporation, 1997.

[67] Michael F Ashby and Kara Johnson. *Materials and design: the art and science of material selection in product design*. Butterworth-Heinemann, 2013.

[68] Ilya Levental, Penelope C Georges, and Paul A Janmey. "Soft biological materials and their impact on cell function". In: *Soft Matter* 3.3 (2007), pp. 299–306.

[69] Bharadwaj, A N. *Ph.D. Thesis*. 2016.

[70] Katia Figueiredo, Tito LM Alves, and Cristiano P Borges. "Poly (vinyl alcohol) films crosslinked by glutaraldehyde under mild conditions". In: *Journal of Applied Polymer Science* 111.6 (2009), pp. 3074–3080.